Advanced Experimental Characterization of Ionic Liquid Electrospray Sources for Space Propulsion

by

David Villegas Prados

A dissertation submitted in partial fulfillment of the requirements for the degree of Doctor of Philosophy in

Aerospace Engineering

Universidad Carlos III de Madrid

Advisor(s):

Pablo Fajardo Peña
Sara Correyero Plaza

Tutor:

Pablo Fajardo Peña

November 2024

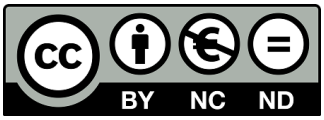

A mi familia—Jose María, Esther, Ángela, Paula y Rocío:
Cada paso que doy lleva vuestra huella. Gracias por caminar siempre a mi lado.

Acknowledgements

The completion of this PhD thesis marks the end of a journey filled with both intellectual challenges and personal growth. Over the course of these years, I have been fortunate to receive the support, encouragement, and friendship of many individuals, without whom this work would not have been possible. I would like to take this opportunity to express my deepest gratitude to those who have shaped both my research and personal development throughout this time.

First and foremost, I would like to sincerely thank my supervisor, Pablo. Your consistent support and approachable nature ensured that I never faced unnecessary obstacles along the way. Whenever I needed guidance, you were there, and for that, I am truly grateful. I would also like to extend my heartfelt thanks to Jaume, whose insightful feedback has significantly elevated the quality of my work. Although you were not directly involved in this thesis, your generous spirit and thorough reviews have played a pivotal role in shaping the research presented here. I am deeply thankful for your willingness to help.

A special thanks goes to Sara, Mick, Dani, and Javi, who welcomed me into such an exceptional team. Your camaraderie, collaboration, and expertise have made this PhD journey not only manageable but enjoyable. From technical discussions to moments of humor, you've made even the toughest challenges feel lighter and the successes more rewarding. Your support at every turn has helped me navigate this process with far greater ease, and I am truly grateful for the privilege of working alongside such a dedicated and inspiring group.

I would also like to extend my gratitude to my colleagues at IENAI SPACE. This research would not have been possible without the unique contributions each of you brought to this challenging project. A special thanks to Patxi—without your skill and dedication, the high-voltage pulse generator would never have come to life. And while we both know there's still room to sharpen those ping-pong skills, your expertise and selflessness have been truly indispensable to me.

To my friends, no matter how far away I am from home, you make anywhere feel like one. Though I may be miles away or in different corners of the world, thank you for your uniqueness, unconditional support, and always being there for me. And dear hardstyle, my love for you will never die.

A mi familia, más allá de cualquier logro o desafío, sois el alma y la brújula de mi vida. A mis padres, gracias por enseñarme que la vida se construye con paciencia, humdildad y, sobre todo, con amor y sencillez. Gracias por permitirme soñar, por cada sacrificio silencioso, y por el cariño con el que habéis formado esta familia.

A mis hermanas—mi mayor felicidad. A Ángela, por contagiar alegría y enseñarme a disfrutar de las pequeñas cosas cotidianas de la vida con tu espíritu vibrante. Y a Paula, por tu ternura y pasión; a pesar de ser la más pequeña, aprendo más de ti de lo que imaginas; de tu determinación y de tu valentía para enfrentar cada reto. Sois la inspiración de esta familia.

Y, a mi compañera de vida, Rocío—through the light and through the dark, you're the fire in my heart. Eres mi refugio, mi impulso, mi norte, mi paz.

David

Published and submitted content

Papers published and submitted in peer-reviewed journals as first author, in ascending chronological order:

- **D. Villegas-Prados**, J. Cruz, M. Wijnen, S. Correyero, P. Fajardo, J. Navarro-Cavallé, "Impact of propellant temperature on the emission regime of an externally wetted electrospray system using time-of-flight mass spectrometry", Acta Astronautica, vol. 213, pp. 145–155, 2023, doi: https://doi.org/10.1016/j.actaastro.2023.08.045. (**Paper I**, fully included in **Chapter 3**).

- **D. Villegas-Prados**, J. Cruz, M. Wijnen, P. Fajardo, J. Navarro-Cavallé, "Emission and performance characterization of ionic liquids for an externally wetted electrospray thruster", Acta Astronautica, vol. 219, pp. 97-107, 2024, doi: https://doi.org/10.1016/j.actaastro.2024.03.013. (**Paper II**, fully included in **Chapter 4**).

- **D. Villegas-Prados**, F.J. Blázquez-Plaza, "High-voltage pulse generator for time-of-flight mass spectrometry in electrospray thrusters", Review of Scientific Instruments - American Institute of Physics, vol. 95 (8), 2024, doi: https://doi.org/10.1063/5.0213974. (**Paper III**, fully included in **Chapter 2**).

Conference papers, in ascending chronological order:

- **D. Villegas-Prados**, S. Correyero, M. Wijnen, P. Fajardo, "Indirect characterization of ATHENA performance, a novel externally wetted Electrospray Propulsion System", in 9th edition of Space Propulsion Conference, Estoril, Portugal, May 2022.

- **D. Villegas-Prados**, M. Wijnen, S. Correyero, G. Arboleya, P. Fajardo, "Impact of the propellant temperature on the performance of externally wetted electrospray thrusters", in Proceedings of 37th International Electric Propulsion Conference, Boston, United States, June 2022.

- **D. Villegas-Prados**, J. Cruz, M. Wijnen, P. Fajardo, J. Navarro-Cavallé, "Ionic liquids performance for externally wetted electrospray propulsion system", in Aerospace Europe Conference - 10th EUCASS - 9th CEAS, Lausanne, Switzerland, July 2023, doi: 10.13009/EUCASS2023-985.

- **D. Villegas-Prados**, J. Kazadi, M. Wijnen, P. Fajardo, "Emission characterization of externally wetted electrospray thrusters using computed tomography", in Proceedings of 38th International Electric Propulsion Conference, Toulouse, France, June 2024. (**Paper IV**, fully included in **Chapter 5**).

Workshops in which the author has participated as a presenter:

- **D. Villegas-Prados**, "Performance characterization of ATHENA with time-of-flight spectroscopy and faraday probe measurements for different ionic liquids", in EPIC Workshop on SRC H2020 "Space Electric Propulsion", Naples, Italy, May 2023.

Whenever material from this source is included in this thesis, it is singled out with typographic means and an explicit reference.

Other research merits

Papers published and submitted in peer-reviewed journals to which the author of this dissertation provided minor contribution:

- F.J. Blázquez-Plaza, A. Barrado, M. Wijnen, **D. Villegas-Prados**. "Electrical model and electrical temperature-dependent model for electrospray thrusters", IEEE Transactions on Power Electronics, vol. 38, no. 10, pp. 12988-12998, Oct. 2023, doi: 10.1109/TPEL.2023.3292421.

- B. de Saavedra, **D. Villegas-Prados**, M. Wijnen, J. Cruz, "Comparison between direct and indirect measurements for externally wetted electrospray thruster with adapted analytical balance", article under review in Acta Astronautica.

- R. Ramos-Tomás, **D. Villegas-Prados**, J. Cruz, B. Sepúlpveda, "Impact of tip angle on the divergence and efficiency of electrospray thrusters", article under review in ACS Applied Electronic Materials.

Conference papers to which the author of this dissertation provided minor contribution:

- G. Di Pasquale, **D. Villegas-Prados**, M. Sanjurjo-Rivo, D. Pérez Grande, "Variable-performance electrospray maneuvers optimization", in Aerospace Europe Conference - 10th EUCASS - 9th CEAS, Lausanne, Switzerland, July 2023, doi: 10.13009/EUCASS2023-988.

- B. de Saavedra, **D. Villegas-Prados**, M. Wijnen, "Comparison of direct and indirect performance measurements of an externally wetted, passively fed electrospray thruster", in Proceedings of 38th International Electric Propulsion Conference, Toulouse, France, June 2024.

Bachelor and master thesis supervised:

- S. Diez Aza, "Modelling of electrospray plume effects on the Genesis Pocketsat mission", Bachelor thesis, Universidad Carlos III de Madrid (2022).

- J. Kazadi, "Reconstruction of electrospray emitted current using computed tomography", Master thesis, University of Liège (2024).

Abstract

This thesis aims to investigate the design, optimization, and performance analysis of electrospray thrusters, more specifically of externally wetted emitters, focusing on their operational modes, propellant behavior, and emission characteristics. Electrospray thrusters, which emit charged particles for propulsion, are of growing interest for small satellite applications due to their compactness and high efficiency. Chapter 2 introduces a novel converter-based bipolar high-voltage pulse generator designed to operate electrostatic gate shutter during time of flight mass spectrometry measurements. This generator allows for synchronized bipolar high-voltage pulses with adjustable voltage levels and frequencies. Experimental results demonstrate the effectiveness of this generator in providing sharp rise and fall times, alongside a voltage tuning range of 300–1000V, improving particle differentiation within the thruster plume. Chapter 3 explores the various operational regimes of electrospray thrusters, driven by the interaction between applied voltage and propellant temperature. Time-of-flight mass spectrometry is employed to analyze the plume composition under varying conditions, revealing that increased voltage favors ion emission, while higher temperatures promote droplet formation. In Chapter 4, the performance of different ionic liquids as propellants is evaluated for externally wetted electrospray thrusters. Seven ionic liquids, including EMI-BF_4, EMI-DCA, EMI-$EtOSO_3$, EMI-Im, EMI-OTf, EMI-SCN, and EMI-TFA are tested, providing insights into thrust, specific impulse, and thrust efficiency. Notably, four ionic liquids are reported for the first time in this context, with some operating purely in the ionic regime and others in mixed regimes. Chapter 5 presents a novel approach to mapping the current density of an electrospray thruster with asymmetric emission using computed tomography. The analysis highlights non-uniform emission patterns and identifies damaged emitter sites, offering valuable insights into the factors affecting emission uniformity and thruster reliability. These studies provide a comprehensive framework for understanding the overall thruster performance and emission characteristics of electrospray thrusters, contributing to their optimization for space missions.

Keywords: *electrospray propulsion, externally wetted emitter, indirect diagnostics*

Resumen

Esta tesis tiene como objetivo investigar el diseño, optimización y análisis de rendimiento de los propulsores de electrospray, específicamente de los emisores externamente humedecidos, centrándose en sus modos operativos, el comportamiento del propulsor y las características de emisión. Los propulsores de electrospray, que emiten partículas cargadas para la propulsión, están ganando interés para aplicaciones en satélites pequeños debido a su compactibilidad y alta eficiencia. El Capítulo 2 presenta un generador de pulsos de alta tensión bipolar basado en convertidor, diseñado para operar el obturador electrostático durante las mediciones de espectrometría de masas por tiempo de vuelo. Este generador permite pulsos bipolares de alta tensión sincronizados con niveles de voltaje y frecuencias ajustables. Los resultados experimentales demuestran la eficacia de este generador en proporcionar tiempos de subida y bajada agudos, junto con un rango de ajuste de voltaje de 300–1000 V, mejorando la diferenciación de partículas dentro del chorro del propulsor. El Capítulo 3 explora los diversos regímenes operativos de los propulsores de electrospray, impulsados por la interacción entre el voltaje aplicado y la temperatura del propulsor. Se emplea espectrometría de masas por tiempo de vuelo para analizar la composición del chorro bajo diferentes condiciones, revelando que el aumento del voltaje favorece la emisión de iones, mientras que las temperaturas más altas promueven la formación de gotas. En el Capítulo 4, se evalúa el rendimiento de diferentes líquidos iónicos como propulsores para propulsores de electrospray externamente humedecidos. Se prueban siete líquidos iónicos, incluyendo EMI-BF_4, EMI-DCA, EMI-$EtOSO_3$, EMI-Im, EMI-OTf, EMI-SCN y EMI-TFA, proporcionando información sobre el empuje, el impulso específico y la eficiencia del empuje. Notablemente, se reportan por primera vez cuatro líquidos iónicos en este contexto, con algunos operando puramente en el régimen iónico y otros en regímenes mixtos. El Capítulo 5 presenta un enfoque novedoso para mapear la densidad de corriente de un propulsor de electrospray con emisión asimétrica utilizando tomografía computarizada. El análisis destaca patrones de emisión no uniformes e identifica sitios de emisores dañados, ofreciendo valiosas perspectivas sobre los factores que afectan la uniformidad de la emisión y la fiabilidad del propulsor. Estos estudios proporcionan un marco integral para comprender el rendimiento general del propulsor y las características de emisión de los propulsores de electrospray, contribuyendo a su optimización para misiones espaciales.

Palabras clave: *propulsión por electrospray, emisor de mojado externo, diagnósticos indirectos*

Contents

List of Figures

List of Tables

Chapter 1

Introduction

Throughout the history of humanity, space has been a subject of worship and fascination for philosophers, scientists, and dreamers. Since the earliest civilizations, the night sky has inspired mythologies, philosophies, and scientific advancements. The vastness of the cosmos has been an enigma that has driven humanity to explore beyond the confines of our planet, seeking answers to the most fundamental questions about our existence and place in the universe.

This innate curiosity has evolved alongside our technological capabilities, leading to significant milestones such as the launch of Sputnik, the Apollo moon landings, and the construction of the International Space Station. These achievements were primarily driven by governmental space agencies with substantial budgets and resources. However, as technology advanced and the cost of access to space began to decrease, the door has been opened for private enterprises to join the quest. These developments set the stage for a new era in space exploration, where the boundaries of what is possible continue to expand rapidly.

In recent decades, we have witnessed the evolution of the space sector with the entry of private companies and startups aiming to democratize access to space. This phenomenon, known as the NewSpace era, has radically transformed the space industry. The goal is no longer just to explore but also to colonize, commercialize, and sustainably utilize space resources. The NewSpace movement has fostered a spirit of entrepreneurship and competition, driving rapid advancements and lowering entry barriers. This has opened up new opportunities for a diverse range of players, including academic institutions, smaller nations, and even individual entrepreneurs, to participate in space activities. Consequently, the landscape of space exploration and utilization is becoming more inclusive, collaborative, and dynamic, setting the stage for a new era of space achievements.

1.1 Propulsion systems in the NewSpace era

As illustrated by Figure 1.1, there has been an exponential increase in nanosatellites and CubeSats launched from the 2000s onward. From a modest beginning of just 2 launches in 1999, the cumulative total surged to over 2,600 by mid-2024. This remarkable increase is driven by advances in technology, reduced launch costs, and an expanding range of applications spanning communications, Earth observation, scientific research, and beyond. Despite this increasing trend, we observe that to date, less than 10% of the nanosatellites launched have propulsion modules on board, and this trend does not match the exponential increase in the total number of launched nanosatellites. This disparity is due to several key factors.

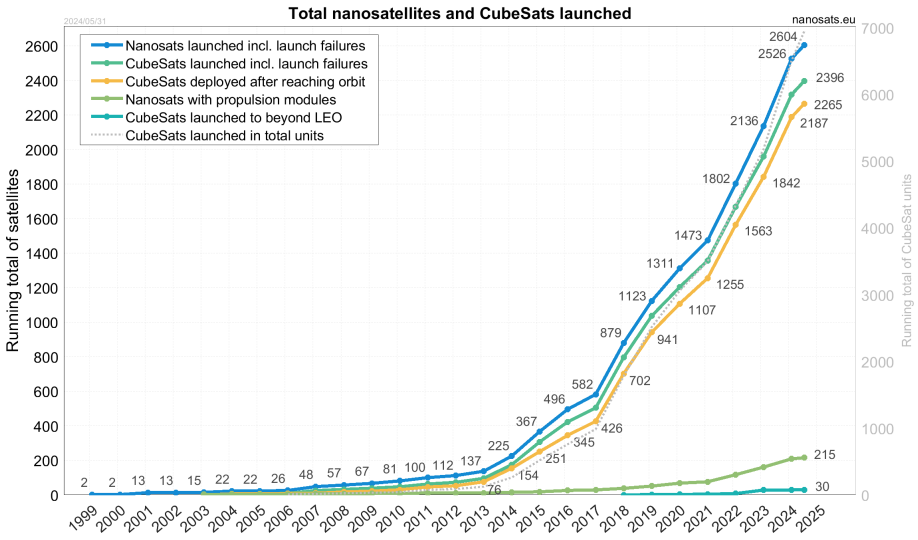

Figure 1.1: Total nanosatellites and CubeSats launched from 1999 to date [1]

Firstly, the integration of propulsion systems into nanosatellites presents significant engineering challenges. These small satellites have reduced size, weight, and power constraints, making it difficult to incorporate traditional propulsion technologies that are typically designed for larger spacecraft. For example, chemical propulsion systems require substantial amounts of propellant and its complex storage, which are not easily accommodated within the compact form factor of nanosatellites [2]. Similarly, traditional electric propulsion systems, such as Hall effect thrusters or ion engines, experience significant reductions in propulsive efficiency when scaled down to fit within the size constraints of nanosatellites [3].

Secondly, the development and testing of new propulsion technologies are time-consuming and costly. Many nanosatellites missions, particularly those from academic and research institutions, operate on limited budgets and tight timelines, making it less feasible to include experimental propulsion systems. As a result, a significant number of nanosatellites are launched without onboard propulsion, relying instead on passive stabilization and nat-

ural orbital decay.

The growing advances in propulsion technologies aim to bridge this gap by providing solutions tailored to the unique needs of nanosatellites. Innovations in the field of electric propulsion (EP) are particularly significant in this regard. Given the inherently limited volume and mass of these satellites, EP systems offer the highest payload mass efficiency as they are more fuel efficient [4]. However, the primary limitation of EP systems is the constrained power availability onboard the spacecraft. Consequently, EP is primarily employed for low-acceleration, constant-thrust maneuvers, such as station-keeping, end-of-life disposal, and attitude control.

Gridded ion thrusters and Hall effect thrusters represent the most mature technologies (TRL-9) within the electric propulsion ecosystem [5]. These systems utilize noble gases such as xenon, argon, or krypton as propellants, necessitating pressurized tanks and active propellant feeding systems. To miniaturize plasma devices while maintaining comparable ionization fractions, it is essential to increase plasma density [6]. This increase leads to more frequent particle collisions with internal surfaces, thereby accelerating erosion and degradation. Additionally, the magnetic components required for electron confinement must generate stronger fields when scaled down. These factors collectively contribute to reduced lifetime and efficiency of these propulsion systems [7], thereby driving the development of new micro-propulsion technologies that overcome these limitations.

1.2 Brief history on electrospray propulsion

The term electrospray is defined as an "ionization process by which analyte molecules or ions present originally in solution are transferred to the gas phase through either solvent or ion evaporation" [8]. Experimental research in this field dates back to the early 20th century, originating in the realms of analytical chemistry and mass spectrometry. In 1914, John Zeleny conducted pioneering experiments to investigate the behavior of liquid droplets in electric fields, specifically their stability, deformation, and eventual disintegration. He identified different operating regimes, such as the formation of steady jets and the onset of droplet emission [9], as well as the first images of liquid dynamics at the meniscus [10]. In the mid-20th century, Sir Geoffrey Ingram Taylor, described the formation of the Taylor cone [11], a cone-like shape in which the liquid deforms when subjected to an electric field. Further advancements were made with the development of electrospray ionization (ESI) by Malcolm Dole in the 1960s [12], who laid the groundwork for ionizing large biomolecules, significantly impacting the biochemistry field. John Fenn later refined this technology in the 1980s, for which he was awarded the Nobel Prize in Chemistry in 2002.

Electrospray propulsion involves the electrostatic acceleration of charged particles extracted from an electrified liquid surface to generate thrust. The concept was first explored in the 1960s by Krohn, who investigated the use of liquid metals and organic liquids, such

as glycerol, as propellants [13], [14]. These thrusters consist of an array of nozzles or capillaries made from conductive material that serves to apply a bias to the liquid propellant. At the tip of each capillary, when a sufficiently strong electric field is applied, a Taylor cone is formed. This initiates the electrospray process, where charged particles are extracted from the liquid and accelerated by the electric field. An extractor electrode positioned near the capillaries facilitates the efficient acceleration of these particles, generating thrust. The primary motivation for developing these thrusters was to achieve higher thrust densities, which could potentially make them viable as primary propulsion systems. This was largely due to the high molecular mass of the emitted particles, known as droplets, which could contribute to substantial momentum transfer. Two distinct research paths emerged based on the type of propellant used:

Field Emission Electric Propulsion (FEEP) with Liquid Metals: Thrusters utilizing liquid metals, such as indium or cesium, evolved into what is now known as Field Emission Electric Propulsion (FEEP). These thrusters demonstrated a stable and efficient ionization process[15], producing high-density ion beams suitable for generating precise thrust [16]. Liquid metals offered advantages like high electrical conductivity, hence higher local electric field [17], and low vapor pressure, making them ideal for maintaining the intense field required for efficient ion emission. However, their high melting points and corrosive nature presented significant operational challenges, particularly in maintaining the metal in a liquid state suitable for continuous ion emission.

Colloid Thrusters with Organic Solutions: Organic solutions, such as doped glycerol and formamide, presented a different set of advantages and challenges. These propellants were easier to handle due to their lower melting points and simpler storage requirements. However, they were prone to droplet formation, which limited the ionization efficiency. To achieve higher specific impulse, acceleration voltages in the range of 100 kV were required [18], leading to significant packaging and engineering challenges. Additionally, organic solvents like glycerol, with a vapor pressure of 0.013 Pa, posed risks of contamination and propellant loss in the vacuum of space.

Significant progress was made in the development of colloid thrusters, with notable advancements including a thruster that operated for 4,350 hours at an operational voltage of 12 kV, delivering 5 mN of thrust [19]. Similarly, Russian developments showcased a thruster that achieved 1 mN of thrust with a specific impulse of 1000 seconds at an operating voltage of 15 kV [20].

Despite these advancements, colloid thrusters did not see widespread adoption. They were designed for very specific applications that, at the time, were not of significant importance. Additionally, the difficulties associated with accommodating high voltages and the relatively low thrust and specific impulse compared to more established ion engines hindered their development. As a result, further research in this area remained dormant until recent years.

1.3 Current research on electrospray thrusters

In recent decades, significant advancements have revitalized interest in electrospray propulsion, positioning it as a competitive technology for modern space missions, particularly in the realm of small satellite propulsion. These developments have been driven by three key factors:

Firstly, the miniaturization of satellite platforms has generated a demand for highly efficient, low-power, and low-thrust propulsion systems that can be integrated into compact form factors. Electrospray thrusters, known for their ability to provide precise control over minuscule thrust levels, have emerged as an ideal solution for these applications [21].

Secondly, advancements in micro-fabrication technologies have enabled the production of highly precise and miniaturized electrospray thrusters. The capability to cluster multiple emitters together has significantly increased the current density, allowing electrospray systems to compete with traditional plasma thrusters. Micro-Electro-Mechanical Systems (MEMS) technology has been instrumental in fabricating miniaturized, compact, and nearly identical emitter arrays, thereby enhancing the scalability and reliability of these systems [22]–[27]. In recent years, additive manufacturing techniques such as 3D printing [28]–[30] and Computer Numerical Control (CNC) machining [31], [32] have been explored as cost-effective and accessible alternatives for the production of electrospray thrusters. These fabrication advancements, coupled with progress in electrospray science, have overcome the limitations of the charge-to-mass ratio of the droplets, reducing the operating voltages to the range of 1–5 kV [33].

Finally, the introduction of ionic liquids as propellants has been transformative for electrospray propulsion. Unlike traditional organic solvents, ionic liquids are composed entirely of ionic species. While their use does not inherently result in higher thrust levels, the efficient ionization provided by ionic liquids allows for better utilization of the propellant and improved thrust-to-power ratios. Ionic liquids offer several characteristics that make them ideal for electrospray propulsion:

- Low volatility: The negligible vapor pressure of ionic liquids prevents propellant evaporation and contamination in the vacuum of space, thereby reducing the need for highly pressurized tanks [34].

- High ionic conductivity: Ionic liquids exhibit high ionic conductivity, which allows for efficient charge transport, with values typically ranging from 0.1 mS/cm to 1.0 S/m [35], [36].

- Wide electrochemical window: Ionic liquids can operate over a broad range of potentials without undergoing decomposition, oxidation, or reduction, in contrast to organic electrolytes [37].

- Thermal stability: Ionic liquids remain stable as liquid media at temperatures up to

200°C, ensuring reliable performance in varying thermal environments [38].

- Dual polarity emission: A unique advantage of ionic liquids in electrospray propulsion is their ability to emit both positively and negatively charged particles, enabling charge compensation, thereby preventing spacecraft charging. This can be achieved by operating two thrusters in opposite polarity [39] or by alternating the emission polarity [40].

- Handling and safety: Many ionic liquids, known as Room Temperature Ionic Liquids (RTILs), are in a liquid state under standard laboratory conditions. Additionally, their low flammability enhances their safety for use in space applications.

- Accessibility: Ionic liquids are commercially available and relatively affordable, with prices typically in the range of a 100 to 1000 euros per kilogram of propellant.

- Tunable properties: The science of ionic liquids is a rapidly growing field, with over 1,000 different ILs reported in the literature [41], [42]. The vast array of possible cation-anion combinations allows for the customization of ionic liquids to optimize their performance for specific applications.

The adoption of ionic liquid propellants has transformed colloid thrusters into what are now recognized as Ionic Liquid Ion Sources (ILIS). These systems are generally categorized under the broader term "electrospray thrusters", distinguishing them from liquid-metal-based thrusters, categorized as FEEP thrusters. Developments of electrospray thrusters has focused on three main emitter configurations based on their morphology: capillary emitters, which evolved from traditional colloid thrusters; porous emitters; and externally wetted emitters (Figure 1.2).

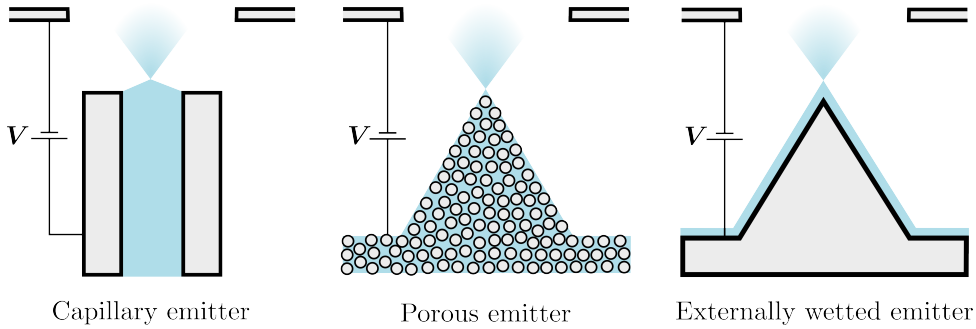

Figure 1.2: Schematic of the different types of emitter morphology: capillary emitter, porous emitter and externally wetted emitter.

Capillary emitters represent the most extensively studied and advanced technology in electrospray propulsion, owing to their origins in colloid thrusters. These emitters are characterized by small channels through which ionic liquids flows, with the flow rate actively controlled to maintain optimal performance [43]–[45]. The operational regime

of capillary emitters is predominantly reported in the cone-jet mode [46], where micro-droplets are emitted from the vertex of the Taylor cone formed at the capillary outlet [47]. In this regime, a portion of the emitted droplets also releases ions, contributing to the thrust generation [48]. The maturity of this technology is evident in its successful demonstration during the Disturbance Reduction System-Space Technology 7 (DRS-ST7) mission [49], a precursor to the Laser Interferometer Space Antenna (LISA) mission [50]. The thruster was the Colloid Micro Newton Thruster (CMNT) developed by BUSEK Co., Inc. The thruster emitted in the droplet regime using the propellant 1-Ethyl-3-methylimidazolium bis(trifluoromethylsulfonyl)imide (EMI-Im) delivering thrust from 5 to 30 μN and nominal specific impulse of 240 s. The maximum operating power of the two thruster clusters was 53 W.

On the opposite end of the spectrum, porous [51]–[54] and externally wetted [55]–[57] thrusters have emerged as innovative solutions for achieving passive propellant flow in electrospray propulsion systems. Porous emitters utilize materials with intrinsic porosity, where capillary forces naturally drive the liquid propellant to the emitter tips. The inherent porosity of these materials also determines the system's hydraulic impedance. Similarly, externally wetted emitters rely on the propellant flowing over the emitter surface. To facilitate this, the emitter surface is textured to wick the liquid to the emitter tips and regulate hydraulic impedance. In both cases, the flow rate is not actively controlled, necessitating a design that is carefully tailored to the specific propellant and desired performance.

These systems were developed because they simplify achieving a pure ionic regime, which is associated with higher specific impulse and greater propulsive efficiency [58]. However, these emitters face significant challenges, particularly related to the manufacturing process. Ensuring uniform propellant distribution and consistent flow rates across the emission surface requires precise control over the emitter's structural uniformity. An example of an externally wetted emitter is the BET-300-P thruster developed by Busek Co., Inc. formed of arrays of wedges, delivering thrust levels ranging from 5 to 150 μN and achieving specific impulses between 840 and 1050 s [59]. The practical implementation of these technologies remains dependent on overcoming the challenges associated with their manufacturing and performance consistency.

1.3.1 Performance in electrospray thruster

To comprehend the benefits that electrospray propulsion can offer to CubeSat propulsion, one can consider the well-known Tsiolkovsky rocket equation, which describes the change in velocity, Δv, of a spacecraft as imparted by its propulsion system:

$$\frac{m_p}{m_{\text{sc}}} = \exp\left(\frac{\Delta v}{I_{\text{sp}} g_0}\right) - 1 \tag{1.1}$$

In this equation, m_{sc} represents the dry mass of the spacecraft, m_p is the propellant mass, I_{sp} is the specific impulse, and g_0 is the standard gravitational acceleration. From this relationship, it becomes clear that a propulsion system with a higher specific impulse can achieve the same total velocity change (Δv) while using less propellant. In the case of high specific impulse systems, a Taylor expansion assuming that $I_{sp}g_0 >> \Delta v$, simplifies the expression to $m_p/m_{sc} \sim \Delta v/(I_{sp}g_0)$, showing linear reduction of the needed propellant mass with increasing specific impulse. This efficiency is one of the key advantages of electric propulsion for CubeSats, where both mass and volume are highly constrained.

To understand how electrospray thrusters generate thrust, we can perform an energy conservation analysis between the electrostatic potential energy and the kinetic energy imparted to a charged particle. This relationship is given by:

$$\frac{1}{2}m_i v_e^2 = q_i \Delta V \tag{1.2}$$

where v_e is the exhaust velocity, ΔV is the potential drop across the emitter and the extractor, and m_i and q_i are the mass and charge of the accelerated particle, respectively. The specific impulse for an electrospray thruster can be simplified to:

$$I_{sp} = \frac{v_e}{g_0} = \frac{1}{g_0}\sqrt{2\Delta V\langle q/m\rangle} \tag{1.3}$$

This equation tells us that, for a fixed voltage differential a propellant with a higher charge-to-mass ratio, q/m, will result in a higher specific impulse. This is where the importance of achieving a pure ionic regime becomes evident. A plume composed entirely of ions has a higher charge-to-mass ratio, leading to propulsion systems with significantly higher specific impulse. Conversely, the presence of droplets—particles composed of multiple propellant molecules with a lower charge-to-mass ratio—can substantially decrease the overall specific impulse. Therefore, from a propulsive efficiency standpoint, minimizing or eliminating these droplets is crucial for maximizing the specific impulse of the system.

Another crucial parameter is the thrust delivered by the propulsion system. In electrospray systems, the thrust, T, can be expressed as:

$$T = v_e \dot{m}_p = I\sqrt{2\Delta V\langle m/q\rangle} \tag{1.4}$$

where $\dot{m}_p$ is the propellant mass flow rate, and it is related to the total emitted current, $I = \dot{m}_p\langle q/m\rangle$. From the thrust equation, we find an inverse relationship with the charge-to-mass ratio, where a plume consisting of more droplets (and hence a higher mass-to-charge ratio) produces higher thrust than a plume composed solely of ions. The thrust required from the system ultimately depends on mission requirements, but the levels generated from a single emission site are typically on the order of 0.1 μN [39]. This limitation

drives the ongoing efforts to manufacture arrays with hundreds of emission sites to achieve higher thrust levels without compromising specific impulse [60]–[62].

The previous expressions for thrust and specific impulse provide a general framework for understanding how the main characteristics of the plume affect performance. However, they do not account for efficiency losses within the propulsion system. One of the major constraints for propulsion systems on small satellites is the limited power available on board, which is typically only a few watts [63]. As a result, power efficiency becomes critically important in scenarios where the available power is limited. The overall power efficiency is determined by the propulsive efficiency of the electrospray thruster and other losses associated with the electrical circuitry that drives the thruster.

From a propulsive standpoint, the thruster efficiency, η_T, represents the system's ability to convert input electrical power, P_{in}, into the kinetic power of the jet, P_{jet}. In the case of electrospray systems, the total efficiency can be decomposed into a series of partial efficiencies [64]:

$$\eta_T = \frac{P_{\text{jet}}}{P_{\text{in}}} = \eta_i \eta_E \eta_\theta \eta_p \eta_x^2 \tag{1.5}$$

These partial efficiencies each account for different processes that contribute to thrust losses:

- The ionization efficiency, η_i, relates to the loss of propellant due to the evaporation of neutral particles from the propellant.
- The energy efficiency, η_E, considers the loss of kinetic energy of a particle relative to the initial potential drop applied.
- The angular efficiency, η_θ, accounts for the lateral acceleration of particles that does not contribute to thrust.
- The polydispersive efficiency, η_p, addresses the acceleration of particles with varying charge-to-mass ratios.
- The transmission efficiency, η_x, considers the loss of current that impacts the electrospray extractor and does not expand to generate thrust.

Characterizing these efficiencies is key to understanding the mechanisms that contribute to performance losses in electrospray systems. Electrospray thrusters can theoretically achieve high efficiencies, as their ionization, energy, and transmission efficiencies are typically close to unity [64], [65]. The primary contributor to efficiency loss in these systems is often the polydispersive efficiency. Therefore, minimizing the presence of particles with distinct charge-to-mass ratios is a desirable objective of these thrusters.

The partial efficiencies can be individually measured using indirect diagnostic techniques. An angular Faraday probe scan is used to estimate the angular efficiency, a retarding potential analyzer is employed to determine the energy efficiency, and time-of-flight mass spectrometry is used to estimate the polydispersive efficiency.

1.4 Motivation

IENAI SPACE is a Madrid-based startup founded in March 2019, with the goal of developing a new propulsion system for small satellites. The technology being developed by IENAI SPACE is based on externally wetted electrospray technology, which presents a very attractive alternative to current electric propulsion systems that rely on the electrostatic/electromagnetic acceleration of a plasma jet. Specifically, electrospray thrusters are of particular interest for platforms where onboard electric power is limited to tens or a few hundred watts, and where expected orbital maneuvers do not have critical time constraints. In return, they offer great simplicity, fewer components in the system (no need for neutralizers, active propellant feed systems), and much higher efficiencies than other electric propulsion technologies for low-power ranges. This technology is of special interest given the increase in the number of small satellite platform launches, categorized as micro- (weighing less than 100 kg) and nano-satellites (weighing less than 10 kg), coupled with their greater application to professionalized services and products.

This increase drives a growing need for precise control over the orbital trajectories of these platforms to maximize their functionality, reduce satellite deployment costs (or those of the constellations to which they belong), enhance the resolution of onboard instruments or revisit time, and enable the necessary maneuvers to prevent potential collisions in orbit. This is made possible through the integration of onboard propulsion systems that allow for orbital control of the platform. Despite the numerous advantages offered by this type of propulsion, no company has yet established itself as the leader in this technology. Consequently, the market for this type of thruster remains open and ripe for innovation.

The development of these electric thrusters requires extensive ground testing and characterization capabilities to certify and evaluate their performance and operational characteristics, such as thrust, efficiency, lifespan, and degradation over time. Certification of electric propulsion thrusters is one of the most critical and challenging aspects of their development. In this context, the creation of diagnostic tools for characterizing electric thrusters has historically evolved in tandem with the development of the thrusters themselves. These tools are essential for generating a comprehensive testing environment that can accurately validate the design hypotheses of these thrusters under conditions representative of the space environment.

The central motivation of this thesis is to advance the knowledge and development of diagnostics available for the characterization of electrospray thrusters, as well as the

understanding of the performance behavior of these thrusters under different operating conditions.

1.5 Gaps and Research Questions

The motivation outlined in Section 1.4 highlights several challenges surrounding the development of electrospray thrusters, not only from a research perspective but also from industrial and commercial viewpoints. Despite the promising potential of electrospray thrusters, especially externally wetted emitters, they remain significantly underreported in the literature, leading to a substantial gap in understanding the performance and current emission characteristics of these thrusters. Interest in this morphology peaked in the early 2000s with pioneering work from the Massachusetts Institute of Technology, but has largely remained dormant until recent years. Recently, a few research groups in Asia have begun exploring these thrusters again[66], [67]. Despite this, there are still many areas of externally wetted electrosprays that have not been covered or are not sufficiently well reported. Several overarching gaps in the field have been identified:

G.1 *Insufficient reporting on externally wetted electrospray thrusters*: There is a significant lack of comprehensive reporting on externally wetted electrospray thrusters. While foundational research was conducted in the early 2000s, more recent studies are sparse. The existing literature does not sufficiently cover various aspects of thruster design, including emission characteristics, operational regimes, and performance metrics. This gap necessitates a detailed examination of the design considerations and operational parameters of externally wetted electrospray thrusters to provide a clearer understanding of their functionality and limitations.

G.2 *Insufficient development of diagnostic tools for electrospray thrusters*: There is a notable lack of detailed research on the development of diagnostic tools specifically tailored for electrospray thrusters. Much of the existing diagnostic electronics are purchased off-the-shelf rather than being developed in-house, leading to a potential mismatch between commercial diagnostics and the specific needs of electrospray thruster testing. Addressing this gap involves creating and refining diagnostic instruments that cater specifically to the unique requirements of electrospray thrusters.

G.3 *Limited information on performance variables and temperature dependence*: There is a deficiency in knowledge regarding the variables that affect the performance and emission characteristics of electrospray thrusters. In particular, the influence of temperature on the operating regime and performance is not well-documented. Understanding how temperature variations impact the thruster's efficiency, thrust, and specific impulse is crucial for optimizing performance.

G.4 *Underexplored ionic liquids for propellants*: Although various ionic liquids have potential as propellants, there is limited exploration of their performance with electrospray thrusters. Many ionic liquids remain untested. This gap in research means that optimal propellants for specific thruster designs have not been fully identified or characterized. Further investigation into the performance of different ionic liquids is necessary to benchmark and select the most effective propellants for various applications.

G.5 *Lack of information on geometric and manufacturing impacts*: There is insufficient knowledge regarding how the geometry of electrospray emitters and small manufacturing imperfections affect emission characteristics. The impact of emitter geometry, the importance of uniformity in emitter manufacturing, and issues such as short-circuiting caused by grid impingement are not well-understood. Understanding these factors is critical for ensuring consistent performance and reliability of electrospray thrusters.

1.6 Objectives

Recognizing the current gaps in the characterization of externally wetted electrospray thrusters, as outlined in Section 1.5, this dissertation aims to make significant scientific contributions to this research area. The primary research objective is to is the development of a holistic testing platform that allows the complete characterization of electrospray thrusters, with respect to their performance: thrust, specific impulse, efficiency, and operating regime. This work will lay the groundwork for the future development of scaling laws to correlate the different design aspects of the thruster emitter. By tracing these mechanisms back to the emitter design, the goal is to develop tailored solutions that optimize thruster performance. To achieve this, a comprehensive suite of diagnostic tools must be developed and implemented, enabling rigorous testing of the thrusters within the appropriate vacuum environment.

Before delving into the specific research objectives, it is essential to highlight the industrial context of this thesis. Conducted within the framework of IENAI SPACE, an industrial company, and supported by a grant from the Spanish government, this thesis is inherently shaped by its industrial nature. This context not only influences the research approach and direction but also defines the scope and objectives of the study. The corporate environment imposes specific implications, particularly concerning the commercial application of these thrusters. Consequently, this research prioritizes a practical approach, with a strong focus on testing and characterization.

Moreover, the industrial setting introduces additional constraints and considerations that are integrated into the research objectives. These constraints may arise from practical limitations, such as available resources, market demands, or operational requirements, all of which play a crucial role in shaping the direction and outcomes of this research.

The necessity to balance scientific exploration with commercial viability ensures that the findings of this dissertation are not only academically rigorous but also directly applicable to the development of market-ready propulsion systems for small satellite platforms. The main objectives along with sub-objectives are described below.

O.1 *Design and development of indirect measurement techniques*: This objective focuses on creating the necessary instruments and methodologies for comprehensive characterization of an electrospray thruster. The diagnostic tools to be developed include:

- **O.1.1** Development of a Retarding Potential Analyzer (RPA) to accurately estimate the energy efficiency of the thruster by measuring the kinetic energy distribution of the emitted particles.
- **O.1.2** Development of a Faraday Probe (FP) with angular resolution to assess the angular distribution and efficiency of the thruster's emitted particles, providing insights into beam divergence and alignment.
- **O.1.3** Development of a Time-of-Flight Mass Spectrometry (TOF-MS) system to determine the polydispersive of the emitted species, characterize the operating regime, and enable indirect estimation of thrust and specific impulse by integrating data from **O.1.1** and **O.1.2**.
- **O.1.4** Development of a computed tomography (CT) scan system for the detailed characterization of individual emission sites, allowing for spatially resolved analysis of the thruster's emission profile.
- **O.1.5** Development of an insulated heater to increase the ionic liquid's temperature during operation.

O.2 *Characterization of an externally wetted electrospray thruster*: Utilizing the tools and methodologies developed in **O.1**, this objective aims to evaluate the performance of the thruster, including partial efficiencies, thrust, and specific impulse, under various operational conditions. The specific tasks include:

- **O.2.1** Investigate the impact of operating voltage on the thruster's performance.
- **O.2.2** Analyze the effect of propellant temperature on the thruster's performance.
- **O.2.3** Explore the influence of different ionic liquids on the thruster's performance, identifying optimal propellants.

O.3 *Development and commissioning of a medium-sized vacuum chamber and testing of diagnostic probes*: This objective involves designing, constructing, and setting up a medium-sized vacuum chamber to simulate space-like conditions for comprehensive testing. It includes developing software for controlling the thruster, managing the associated instrumentation, and acquiring data. Additionally, this objective covers the integration, calibration, and validation of the diagnostic probes developed

under **O.1**, ensuring their precise functionality and effectiveness in a controlled environment.

O.4 *Dissemination and communication of the research results*: This objective covers the systematic dissemination of research findings through academic publications, conference presentations, and other relevant platforms.

1.7 Contribution of this Research

Given the background, the identified gaps discussed in Section 1.5, and the objectives outlined in Section 1.6, this section highlights the original contributions of this dissertation. Each contribution is linked to a specific publication that addresses one or more research objectives. Among these publications, three are peer-reviewed journal articles (**Paper I**, **Paper II**, and **Paper III**), which have been published in internationally indexed scientific journals. Additionally, one publication (**Paper IV**) is presented as a conference paper, with efforts underway to convert it into a journal article. The detailed contributions are as follows:

C.1 *Development of a high-voltage pulse generator for time-of-flight mass spectrometry in electrospray thrusters*: This contribution details the design of an electronic board for high-voltage switching, specifically tailored for use with electrostatic shutter gates in TOF-MS. It includes variable voltage and duty cycle capabilities, employing off-the-shelf components to achieve low noise, and minimal rise and fall times (**Paper III**).

C.2 *Characterization of an externally wetted electrospray thruster under varying voltage and temperature conditions*: This contribution represents the first report on propellant temperature analysis for this type of emitter. It demonstrates how variations in temperature and voltage influence the operating regime and overall thrust performance of the thruster (**Paper I**).

C.3 *Study of various ionic liquid propellants using an externally wetted electrospray thruster*: Although many ionic liquids exist, the majority have not been extensively tested. This work highlights the performance of seven ionic liquids, including some well-documented in the literature and others newly investigated. It provides a benchmark comparison with other thrusters using similar propellants (**Paper II**).

C.4 *Development of a simple and reliable computed tomography scan for high-resolution reconstruction of emission site profiles*: This contribution addresses the importance of uniform emitter manufacturing and the challenges associated with it. It presents a computed tomography system that enables high-resolution imaging of emission sites, improving understanding of emitter performance and manufacturing quality (**Paper IV**).

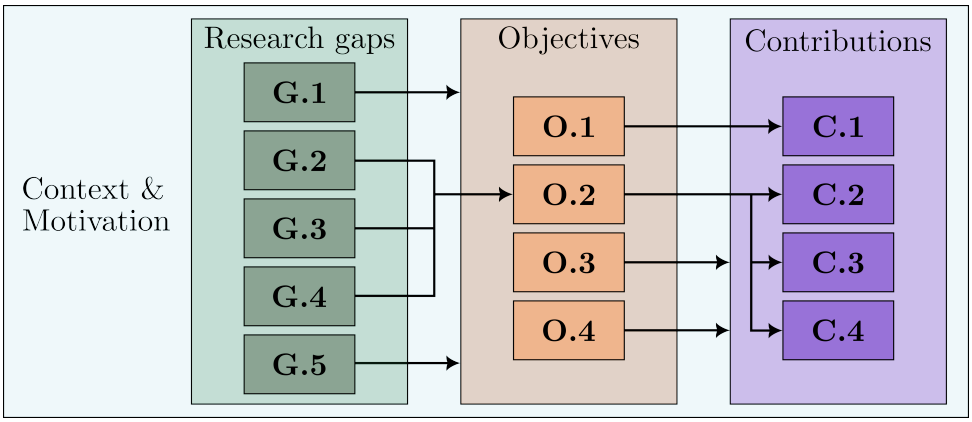

Figure 1.3: Schematic of the research gaps, objectives and contributions and their links.

To clarify the relationship between the research gaps, objectives, and contributions, Figure 1.3 provides a schematic overview. In this diagram, each research gap is addressed by the corresponding objectives, as indicated by the connecting arrows. Similarly, the thesis objectives are linked to the relevant contributions, illustrating how each objective has been achieved. When an arrow spans the entire framework, it signifies a connection to all the objectives or contributions, indicating a comprehensive relationship.

1.8 Thesis structure

This dissertation is organized as a collection of journal articles, with each chapter dedicated to one of the published research works. These chapters are structured to directly address the research questions outlined in Section 1.5 and to achieve the objectives detailed in Section 1.6. Each article is included in its full form, with minor editorial modifications, such as resizing figures and tables, to enhance readability. While the nomenclature is largely consistent across the articles, some differences exist, so a specific nomenclature section has been added to each article to improve clarity.

The thesis is organized as follows: Chapter 2 presents the content of **Paper IV**, which details the development of a key diagnostic tool—the time-of-flight measurement—that enabled the characterization work presented in this dissertation. Chapter 3 covers the content of **Paper I**, which focuses on the characterization of externally wetted electrospray thrusters under varying operating voltages and propellant temperatures. Chapter 4 contains **Paper II**, which explores the characterization of seven different propellants, highlighting the versatility of the thrusters and the performance variations that arise from using different ionic liquids. Chapter 5 includes **Paper III**, which introduces a diagnostic tool that, while not used for direct performance estimation, provides crucial insights into the uniformity of current emission across the thruster, akin to a computed tomography scan. Finally, Chapter 6 draws together the conclusions of this research, discussing the capabilities and limitations encountered, and proposing potential directions for future

research.

Chapter 2

Development of indirect diagnostics

The content of the current chapter coincides with the following journal paper:

- **D. Villegas-Prados**, F.J. Blázquez-Plaza, "High-voltage pulse generator for time-of-flight mass spectrometry in electrospray thrusters", Review of Scientific Instruments - American Institute of Physics, vol. 95 (8), 2024, doi: https://doi.org/10.1063/5.0213974 (**Paper III**).

Paper content and author contribution

This research focuses on the development of a high-voltage pulse generator specifically designed for time-of-flight mass spectrometry in electrospray thrusters, addressing thesis objective **O.1**. The design and development of this generator align with objective **O.1.3**, providing valuable insights into the creation of instruments for the characterization of electrospray thrusters (**G.1**).

In this paper, we present a simple and cost-effective solution using off-the-shelf components to construct a pulse generator that competes with market-leading devices in terms of rise and fall times. The generator is capable of producing high-voltage pulses with differential voltages up to 1000 V, achieving maximum rise and fall times of 30 ns, while offering selectable pulse width and frequency (up to 100 Hz). As part of the time-of-flight setup, this diagnostic tool has been tested in a controlled vacuum environment, successfully fulfilling objective **O.3**.

The candidate contributed significantly to this work, including circuit simulation, PCB design, soldering, testing, debugging, and the characterization of the pulse generator with electrospray thrusters. This research has been published in the Review of Scientific Instruments by the American Institute of Physics (**O.4**).

* * *

Abstract

Electrospray thrusters exhibit diverse operational modes based on the nature of ejected particles. Time-of-flight mass spectrometry is frequently employed to analyze the composition of the plume. This study introduces a novel converter-based bipolar high-voltage pulse generator aimed at producing synchronized bipolar high-voltage pulses with controllable voltage levels and frequencies, specifically tailored for the study of electrospray thrusters. The proposed topology generates bipolar high-voltage rails from a low-voltage power source through the Forward-Flyback with Cockcroft-Walton voltage multiplier topology. Subsequently, fast high-voltage MOSFETs are employed to generate the high-voltage pulses. The paper outlines the operational principles and design methodologies of the pulse generator. Experimental verification corroborate its operational principles and functionalities, revealing that the pulse rise and fall times consistently remain below 30ns while the voltage can be tuned within the range of 300-1000V. An electrospray thruster was employed to conduct a thorough and practical validation of the high-voltage pulse generator. This included generating time-of-flight curves and mass spectra of the plume, resulting in precise differentiation of all particles present.

Nomenclature

C	system capacitance	n	transformer's turn ratio
C_e	electrodes capacitance	q/m	charge-to-mass ratio
C_g	gate capacitance	r_c	collector radius
C_{coax}	coaxial cable capacitance	s_g	gate spacing
C_d	diode junction capacitance	s_p	ground-gate spacing
C_o	output capacitance	t_g	gate thickness
C_{st}	stray capacitance	v_i	ion velocity
C_w	winding parasitic capacitance	V_a	thruster applied potential
D_1	switch-on fraction diode	V_g	electrostatic gate voltage
Δe	energy resolution	$V_{\text{DS,max}}$	maximum switching voltage
Δt	time resolution	V_{in}	input voltage
h_g	gate height	V_o	DCDC output voltage
$L_{e,g}$	extractor-gate length	V_r	repeller voltage
L_{lk}	leakage inductance	$V_{\text{o,p}}$	positive high voltage output voltage
L_m	magnetizing inductance	$V_{\text{o,p}}^{\sqcap}$	positive high voltage pulse voltage
L_{ToF}	flight length	$V_{\text{o,n}}$	negative high voltage output voltage
m	number of voltage multiplier stages	$V_{\text{o,n}}^{\sqcup}$	negative high voltage pulse voltage

Acronyms/Abbreviations

CDVM	Capacitor-Diode Voltage Multipliers
DC	Direct Current
EMI-BF_4	1-Ethyl-3-methylimidazolium tetrafluoroborate
ESG	Electrostatic Shutter Gate
FF-CW	Forward-Flyback Cockcroft-Walton
HB	Halg Bridge
HV	High Voltage
HVPG	High-Voltage Pulse Generator
MBL	Multi-stage Blumlein Lines
MMC	Modular Multilevel Converter
MOSFET	Metal-Oxide-Semiconductor Field-Effect Transistor
MPC	Magnetic Pulse Compressor
MS	Mass Spectrometer
PCB	Printed Circuit Board
PFN	Pulse Forming Network
PG	Pulse Generator
PWM	Pulse Width Modulation
SEE	Secondary Electron Emission

SPDT	Single Pole Double Throw
TIA	Transimpedance Amplifier
ToF	Time of Flight
TTL	Transistor-Transistor Logic
ZVS	Zero Voltage Switching

2.1 Introduction

A high-voltage pulse generator (HVPG) was custom-designed and constructed to facilitate precise time-of-flight (ToF) measurements of ion beams extracted from an ionic liquid electrospray thruster. In the domain of electric propulsion, an electrospray thruster functions by extracting and accelerating ions from an electrified ionic liquid propellant. Ionic liquids are electrically conductive salts in liquid state at room temperature composed of negatively and positively charged molecules. They are characterized by its low vapor pressure and stability making them ideal for space propulsion applications. The ionic liquid employed is the commonly used 1-ethyl-3-methylimidazolium tetrafluoroborate (EMI–BF_4) [64], where EMI^+ represents the cation and BF_4 the anion. Moreover, the ability to eject both positive and negative particles allows to achieve a neutral plume avoiding charge accumulation [68].

Consisting of two passive components, namely the emitter and the extractor, the electrospray thruster relies on the emitter's specialized geometric attributes, which facilitates, upon the application of high voltage to the ionic liquid, the attainment of a sufficiently electric field for the ionic liquid to deform into what is commonly referred to as Taylor cones [69]. Subsequently, particles are extracted from these cones and accelerated using the same electric field. The polarity bias between the ionic liquid and the extractor dictates whether positive or negative particles are extracted. An schematic of a single emitter electrospray thruster is shown in Fig.2.1.

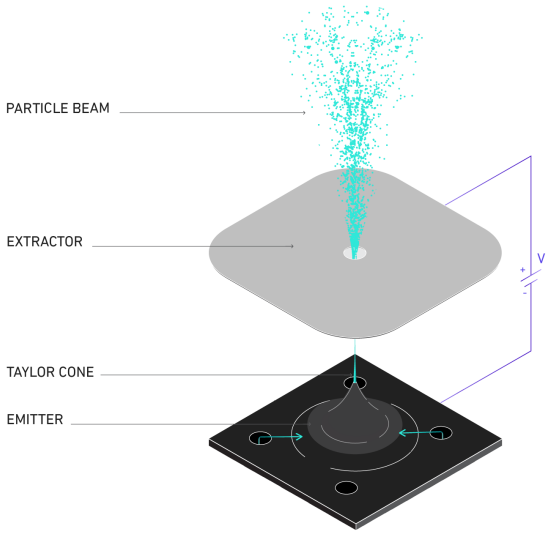

Figure 2.1: Schematic of an externally wetted electrospray source, where the ionic liquid propellant flows over the emitter surface and the emitter present cone-like protrusion to enhance ion evaporation.

The complexity of the electrospray thruster plume, characterized by its diverse species and varied energy distributions, poses a significant challenge to achieving optimal propulsive performance. Hence, comprehending the composition of the ion beam is key for the

development and improvement of these systems. The utilization of a time-of-flight mass spectrometer (ToF-MS) stands out as the primary diagnostic tool to achieve said task and has been widely employed to characterize these devices [70]–[72]. By understanding the plume composition, performance parameters such as thrust, specific impulse or propulsive efficiency can be indirectly measured.

A critical component of ToF-MS for electrospray is the generation of a high voltage pulse. This study introduces a converter-based bipolar HVPG capable of producing synchronized bipolar HV pulses with adjustable voltage levels and frequencies. While HVPG have found applications in various fields such as electron-impact ionization [73], ion trap [74] or single reflection [75], there has not been a pulse generator specifically tailored for electrospray thruster applications. Section 2.2 presents the theory in ToF-MS for electrospray and requirements imposed to the HVPG. Section 2.3 explains the design of the converter-based bipolar HVPG, comprising the HV DC/DC converter, the bipolar kilovolt pulser for modulating the HV-DC outputs, and the pulse logic to achieve synchronized pulse generation. Experimental results validating the HVPG operation are provided in Section 2.4. Finally, Section 2.5 summarizes the conclusions of the study.

2.2 Time-of-flight mass spectrometry in electrospray

In electrospray, ToF-MS allows the identification of the different emitted particles and their contribution to the total emitted current. This is achieved by obtaining the specific charge or charge-to-mass ratio, q/m, of the particles. Because the particles emitted by the thruster have some charge q_i, they are accelerated by the potential drop V_a between the emitter and extractor. Energy conservation yields an expression for the velocity, v_i, of a particle leaving the thruster:

$$v_i = \sqrt{2\,(q/m)_i\,V_a} \tag{2.1}$$

which is dependent on the aforementioned charge-to-mass ratio, $(q/m)_i$. The beam of the thruster will consists of particles with different charges and masses. An electrospray thruster can emit two types of particles: ions, which distribution of specific charge is discrete, and droplet whose range of specific charges is a continuum. In the case of ions, these particles sometimes are emitted associated to neutral particles, forming oligomers with different degrees of solvation, n, depending on the amount of neutral attached to the ion. Typically, oligomers with $n = 0, 1, 2$ show notable current fractions, while those with higher n are often undetectable. This equation represents a simplified model that assumes the electrospray operates in a pure ionic regime without fragmentation. Despite its simplicity, it provides a useful quick estimation for calculating ion velocity and performing an initial sizing of the ToF gate.

The ToF-MS provides the mass distribution of the ion beam by measuring the ion beam current as a function of time. The particles are emitted through a section of known

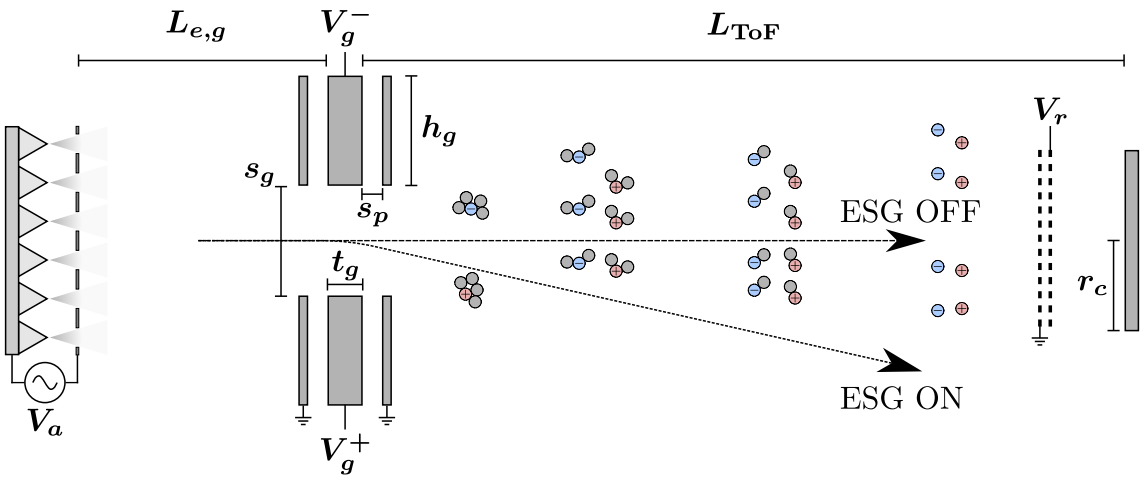

Figure 2.2: Schematic of time-of-flight setup with a deflection gate as electrostatic gate shutter. When the ESG is in OFF state particles are able to reach the collector, while when the state is ON, particles are deflected, hence not collected.

flight-length, L_{ToF}, resulting in a travel time, $t_i = L_{\mathrm{ToF}}/v_i$. Particles with higher q/m will arrive earlier to the collector, while those with lower q/m will arrive later in time.

A typical ToF setup for electrospray thruster characterization contains two components: an electrostatic shutter gate (ESG) and a collector, as illustrated in Fig.2.2. The ESG is driven by the square pulse of the developed HVPG. When the ESG is turned off, all incoming particles are able to pass. By activating the ESG on for a short time τ_{ON} ($\sim$ 500 μs) all particles arriving the gate are blocked. However, particles downstream of the ESG will still arrive at the collector. Since the particles have different velocities (due to different specific charges) they will hit the collector at different times, arriving first the ones with higher velocities. The collector is connected to ground through a high bandwidth and amplitude trans-impedance amplifier at the end of the flight region. Through this method, the current composition time-wave can be obtained, which later can be translated into a mass spectrum.

Moreover, a secondary electron repeller is positioned in front of the collector. The repeller consists of a grounded grid and a grid biased negatively by a few tenths of a volt. The use of the repeller allows to collect the secondary electrons generated by the impact of high-speed ions on the collector.

2.2.1 Time-of-fight electrostatic shutter gate potential

The gate design can take a variety of forms including: stopping gate, deflection gate, or Bradbury-Nielsen gate. Stopping gates consists of semi-transparent grids spaced by a few millimeters. By biasing the middle grid to a voltage larger than the source potential all the ions are stopped. The main drawback is erosion of the thruster surface since particles are reflected back when the gate is active. The deflection gate approach is a simpler and more

reliable alternative. It consists of a perpendicular electric field (to the ion beam) created by means of two biased plates, eliminating the needs of grid which reduce the current and avoiding the generation of SEE. Bradbury-Nielsen gates are formed of interleaved wires, increasing the transparency and reducing erosion and back-streamed particles, but present challenges due to its complex manufacturing [76].

In this work, the ESG developed is a deflection gate, due to its easy manufacturing, implementation and reduced erosion. By applying a bias to the gate, particles are deflected, preventing them from reaching the collector. The deflection angle, θ_d, experienced by an ion passing through the activated electric field is governed by

$$\theta_d = \arctan\left(\frac{t_g}{4s_g}\frac{V_g}{V_a}\right) \tag{2.2}$$

where t_g is the thickness of the gate plates, s_g the spacing of the plates, and V_g the differential voltage between gate electrodes. For proper design of the ESG, θ_d must exceed the collection angle, θ_c, which is the maximum angle deviation a particle can have to reach the collector while the gate is deactivated. This relationship is encapsulated by the trigonometric expression

$$\theta_c = \arctan\left(r_c/L_{\text{ToF}}\right) \tag{2.3}$$

where r_c denotes the radius of the collector. Solving the inequality $\theta_d > \theta_c$ yields a constraint on the differential voltage supplied to the pulse generator, expressed as:

$$V_g > \frac{4s_g r_c}{t_g L_{\text{ToF}}} V_a \tag{2.4}$$

While numerous combinations may satisfy this condition, the primary constraint often lies in the flight length, dictated by the capabilities of the vacuum facility. Given that the gate geometry (s_g, t_g) closely matches the thruster dimensions (~10 mm), and considering a maximum operating voltage of the electrospray thruster used in for this analysis, $V_a = 2$ kV, the minimum operating voltage of the high-voltage pulse generator is determined by the vacuum facility. Reducing the flight length is advantageous as more current can be collected reducing noise levels. However, as discussed in Section 2.2.2, higher resolution times are needed. The developed pulse generator is capable of supplying up to +1 kV and -1 kV to the plates resulting in a gate voltage, $V_g = 2$ kV. A preliminary numerical analysis using Eq.2.4, and considering $t_g = 5$ mm, $s_g = 12$ mm, $r_c = 45$ mm, shows that with that selected V_g, L_{ToF} can be reduced to 432 mm.

This analysis serves as a basis for selecting the operating voltage of the gate, depending on the characteristics or requirements of the facility. Longer flight lengths necessitate a lower gate voltage. However, we selected a desired deflection angle that is at least 1.5 times greater than the collection angle to incorporate a safety factor. This precaution accounts for the fact that our analysis does not consider potential fragmentation or ion evaporation from droplets, which would increase the m/q ratio and result in lower deflec-

tion angles [77]. Accounting for this safety margin upholds the reliability and efficacy of the electrostatic shutter gate. The vacuum facility for this study allows for setting a flight length of 700 mm which results in $\theta_c = 3.68°$ and $\theta_d = 5.95°$, guiding the ESG configuration to balance current collection and resolution needs.

Another critical design consideration for the deflection plates is optimizing their size relative to the spacing between them. Reducing the plate size has significant advantages, including a decrease in the system's total capacitance. This reduction enhances the dynamic response of the deflection gate by shortening the time required to charge and discharge the electrodes, thereby improving switching speed. However, large apertures relative to the plate size can introduce potential "leakage," resulting in a non-uniform electric field. This non-uniformity can cause inconsistencies in particle deflection, as ions experience varying forces depending on their trajectories.

The capacitance of each leg of the deflection gate includes the stray capacitance between the electrode and the ground plates, C_s, plus half the capacitance between the electrodes, C_e. This results from the electrodes being biased to the same voltage but with opposite polarities, creating a virtual ground between them:

$$C_g = C_s + \frac{1}{2}C_e = \frac{2\epsilon_0 h_g w_g}{s_p} + \frac{\epsilon_0 t_g w_g}{2s_g} \tag{2.5}$$

where ϵ_0 is the absolute permittivity, h_g is the height of the plates, w_g is the width of the plates, and s_p is the spacing between ground and electrode plates. In addition, the total capacitance seen by each polarity of the HVPG must include the capacitance of the coaxial cable, leading to a total capacitance $C = C_g + C_{\text{coax}}$. Commonly, coaxial cables have a capacitance of 100 pF/m. Using Eq.2.5, and taking into account a total of 1.5 meters of coaxial cable (air-side + vacuum), the setup employed had a total capacitance for each leg of approximately 300 pF. Note the importance of considering the cable capacitance, as in our case it corresponds to half of the total capacitance.

The last geometric consideration is that the aperture diameter should be such that the gate angle (angle between thruster emitter and gate aperture) matches that of the collector calculated before, $s_g = 4r_c L_{\text{e,g}}/L_{\text{ToF}}$, where $L_{\text{e,g}}$ is the extractor-gate axial distance.

2.2.2 Time-of-flight resolution

A critical parameter in the design of the HVPG electronics is to achieve the desired time resolution for the ToF data. The required time resolution, Δt, in mass spectromentry for electrospray thrusters is calculated according to [78]

$$\Delta t = \frac{\Delta e}{2}t = \frac{\Delta e L_{\text{ToF}}}{2v_i} \tag{2.6}$$

where Δe is the required energy resolution expressed in percentage and t the flight time of an ion. Previous study has suggested that the required energy resolution to resolve all

present species in an electrospray plume should be at least 5% [70]. The equation highlights the role of L_{ToF} in improving time resolution. A longer ToF chamber increases the ion flight time, effectively amplifying the time difference between ions with slightly different energy levels or masses. Considering the most restrictive scenario with the minimum calculated L_{ToF} and the maximum velocity of EMI^+ ions (112 Dalton) at the highest applied voltage, the ion flight time is approximately 7.4 μs. Consequently, using Eq.2.6 the minimum time resolution is estimated to be 180 ns. This time resolution is assumed to be the upper limit constraint of the required rise/fall times of the designed HVPG.

It is important to take into account the minimum current that the ToF setup is able to detect. Apart from the geometric constraint, the transimpedance amplifier (TIA) used plays a big role. In this work, the commercial TIA DHCPA-100 is used, which features tunable high amplification and high bandwidth. The amplitude was set to 10^6 and the bandwidth to 1.8 MHz, and they remain constant throughout the whole energy spectrum. The bandwidth, B, is directly related to the to the maximum rise time that the collector system can detect through $t_{\mathrm{r,max}} = B/0.35$, and it has to be higher than the actual rise/fall times of the HVPG. With this characteristic our setup is able to detect collected currents down to 10 nA. While working with an array of electrospray these currents are easily obtained, but while working with single emitters, which emit currents in the order of 100-200 nA [55], [57], [68], the collected currents can be lower, and other devices such as einzel lens to focus the beam or channeltrons can be used to enhance the collected current output [79].

2.3 Architecture of the high-voltage pulse generator

The high-voltage pulse generators are classified in literature into two primary categories: classical generators and solid-state generators [80].

The HV pulses in classical generators are achieved by charging a group of capacitors in parallel and subsequently discharging them in series [81], and can be subdivided into the Magnetic Pulse Compressor (MPC), the Pulse Forming Network (PFN), the Multistage Blumlein Lines (MBL), and the Marx generator [82].

Actual power electronics switches can tolerate HV and deliver rapid on/off switching performance for narrow HV pulse generation, introducing several solid-state HVPGs. Some power electronics-based PGs emulate classical PGs, as the Marx generator. Furthermore, solid-state HVPGs exhibit a modular design, offering advantages as redundancy, scalability, and robust operation as well as being a long-lasting, and cost-effective alternative for pulse generation [82]. The use of solid-state switches into pulsed power supplies results in a smaller and more efficient system, leveraging power electronics control techniques [82] by the ease of gate control, snubberless operation, and reduced power losses. Power electronics-based PGs are based on DC-DC converters and can be categorized into three main groups based on their structure: Modular Multilevel Converter (MMC) based,

non-MMC-based, and hybrid topologies [83].

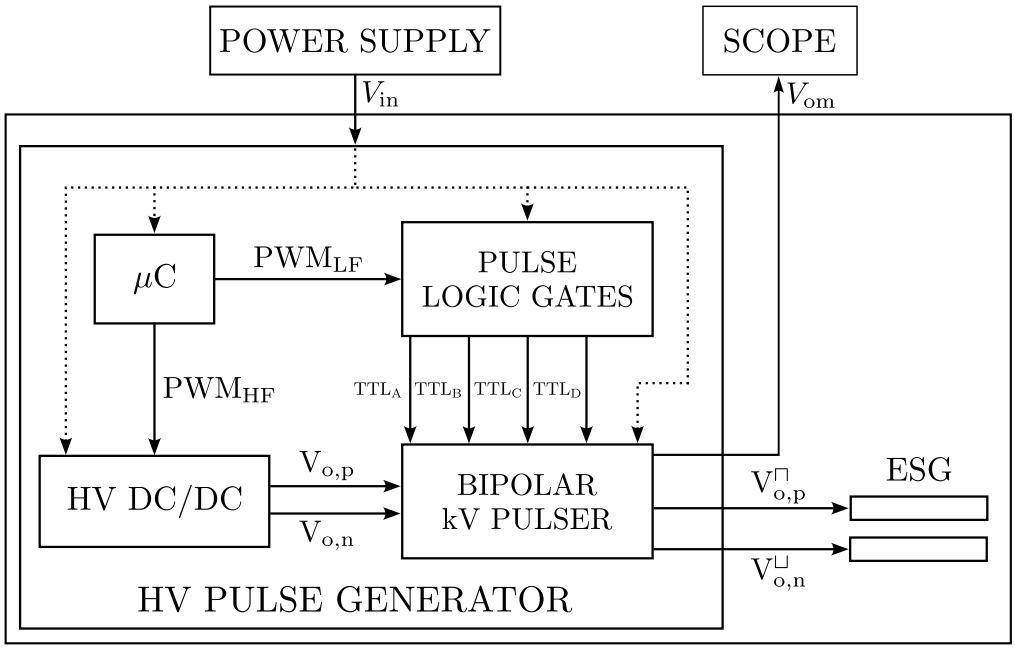

Figure 2.3: HVPG: block diagram.

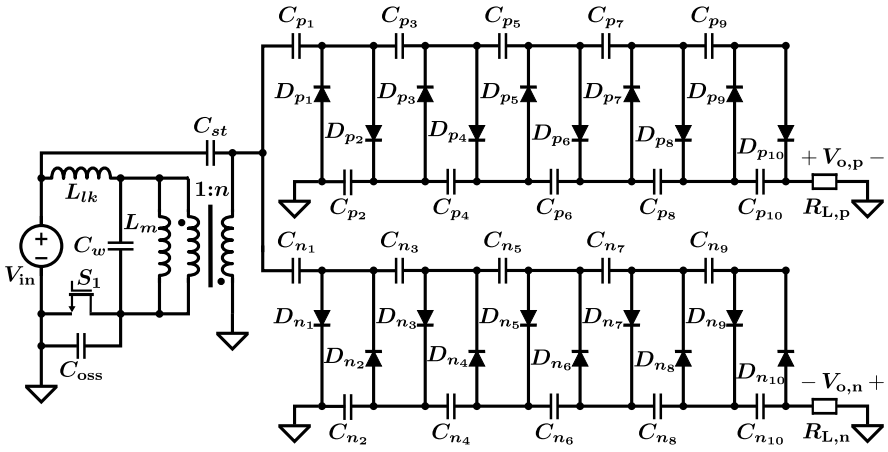

Figure 2.4: Forward-Flyback converter with two fifth-order CW-VMR considering the transformer non-idealities.

The PG proposed is based on a bipolar non-MMC-based converter, where Capacitor-Diode Voltage Multipliers (CDVMs) are used to achieve a high output-input voltage gain from a 5V DC supply, V_{in}, within a converter's duty cycle ranging from 0 to 50 %, with switching frequency below 200 kHz, making it suitable for in-house applications, and providing configurable regulated output voltages. However, the proposed PG requires for HV controlled switches at the output stage to modulate the generated HV DC voltage [81].

The architecture of the HV pulse generator is illustrated in Fig.2.3. It comprises three distinct subcircuits. Firstly, the HV-DC/DC converter generates bipolar HV rails from

the 5V power bus while minimizing power conversion losses (therefore, heat dissipation). Subsequently, the bipolar kilovolt pulser circuit is connected in series with the ESG to modulate the generated HV DC. This subcircuit is driven by the fast pulsing low voltage logic, guaranteeing a swift rectangular pulse shape and simultaneous firing of both polarities to preserve the synchronized reflection times of the ESG.

The HVPG presented in this study consumes a total power of 0.6 W in the most demanding scenario of supplying ±1 kV. The electrical power required to operate each electrostatic gate, as calculated with Eq.2.7, is approximately 7.5 mW. This relatively low power consumption is attributed to the low pulse frequency, f_{PWM}, of around 25 Hz.

$$P_g = V^2 f_{\mathrm{PWM}} \frac{C}{2} \tag{2.7}$$

2.3.1 HV DC/DC converter

The chosen topology for generating the bipolar HV outputs is the Forward-Flyback with two fifth-order Cockcroft-Walton Voltage Multiplier converter (FF-CW) in Discontinuous Conduction Mode (DCM) depicted in Fig.2.4 [84]. The low-voltage NMOS MOSFET (n-Channel Metal Oxide Semiconductor Field Effect Transistor) switch, S_1, is controlled by a high-frequency Pulse Width Modulated (PWM) signal. Parasitic capacitance influence the circuit operation, particularly at high voltages and low power conditions, allowing quasi-ZVS (Zero Voltage Switching) to reduce energy losses [85].

This topology includes along the MOSFET output capacitance. C_{oss}, and diode junction capacitance, C_d, the transformer parasitic components. Eq.2.4 includes leakage inductance, L_{lk}, total winding parasitic capacitance, C_w, equivalent stray capacitance, C_{st}, and magnetizing inductance, L_m. To achieve quasi-ZVS is necessary to turn ON the MOSFET when the voltage across all parasitic capacitance has reached the minimum voltage levels in the resonance. This allows the resonant energy to flow through the parasitic capacitance and magnetizing inductance and to be conserved.

Besides, the voltage drop in the CW-VMRs affects voltage gain since current passes through the CW-VMR capacitors before supplying energy to the load to charge them. Consecutive capacitors (even ones) partially discharge when delivering energy to the load and charging the opposite capacitor branch (odd ones), leading to an undesired output voltage drop. The total voltage gain considering the voltage drop effects can be expressed as shown in Eq.2.8, which depend on the number of voltage multiplier stages, m, transformer's turn ratio, n, switch-on fraction of the period, D_1, magnetizing inductance, switching frequency, f_{sw}, output capacitance, $C_{p_i} = C_{n_i} = C_o$), and equivalent output resistance, $R_L = R_{\mathrm{L,p}} || R_{\mathrm{L,n}}$. It is also assumed that $V_o \approx V_{\mathrm{o,p}} \approx |V_{\mathrm{o,n}}|$.

$$\frac{V_o}{V_{\mathrm{in}}} = \frac{\frac{nm}{2}\left[1 + \sqrt{1 + \frac{2R_L}{L_m f_{sw}}\left(\frac{D_1}{nm}\right)^2}\right]}{1 + \frac{2m^3+3m^2+m}{12R_L f_{sw} C_o}} \tag{2.8}$$

From Eq.2.8, D_1 can be calculated according to Eq.2.9. Therefore, for a fix f_{sw}, tuning D_1 allows to vary the voltage applied to the ToF gate. The quasi-ZVS operation point can be achieved if f_{sw} is also tuned together with D_1.

$$D_1 = \frac{nm}{2}\sqrt{\frac{2L_m f_{sw}}{R_L}\left(\left[\frac{2V_o}{nmV_{\text{in}}}\left(1+\frac{2m^3+3m^2+m}{12R_L f_{sw} C_o}\right)-1\right]^2-1\right)} \tag{2.9}$$

2.3.2 Bipolar kilovolt pulser

The HV DC signals are modulated into two rectangular waveforms, positive $V_{\text{o,p}}^{\sqcap}$ and negative $V_{\text{o,n}}^{\sqcup}$ with an oscillating frequency in the tens of hertz range, using the circuit depicted in Fig.2.5 [86]. A pair of n-channel MOSFET switches in half-bridge configuration (HB), Single Pole Double Throw (SPDT) switches, are employed to alternate the connection of the output between ground and the HV DC source in each polarity to generate the pulses. Due to the high impedance nature of the time-of-flight gate and the presence of numerous capacitors in the CDVMs, the application of pulses does not induce a drop in the output voltage.

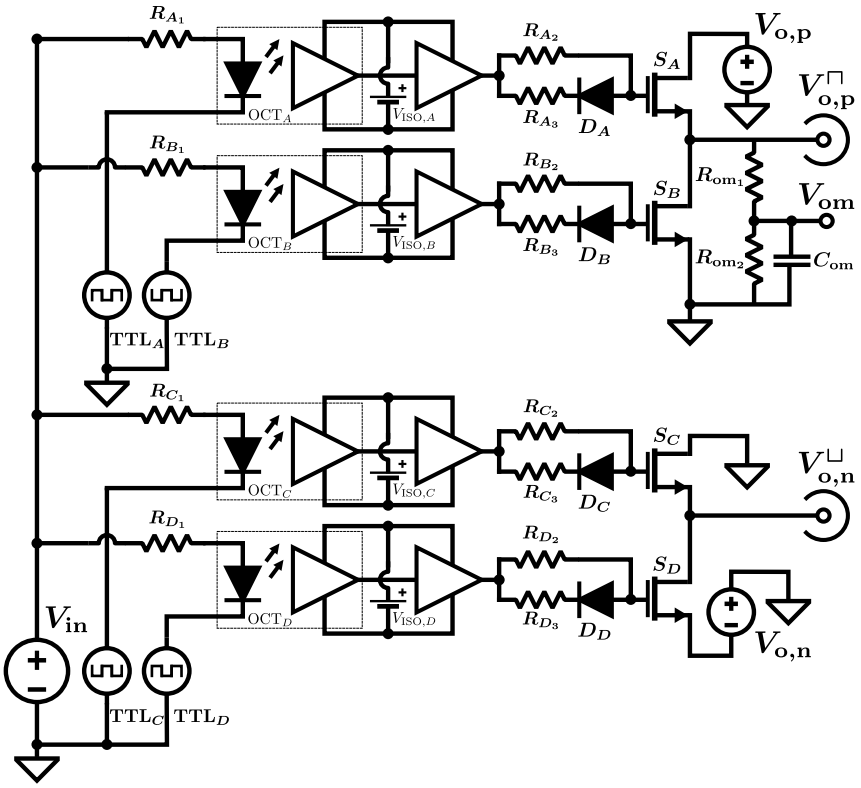

Figure 2.5: Bipolar kilovolt pulser: schematic.

The MOSFETs (S_A-S_B for the positive leg, S_C-S_D for the negative) are high side driven, creating floating gate-source voltages V_{GS} by using auxiliary isolated low-voltage supplies, V_{ISO}. These signals are generated from fast TTL logic-level inputs, described in Section 2.3.3, using an isolated high-speed octocoupler and a high-speed driver. Despite

the logic provides transitions within tens of nanoseconds of rising and falling times, the primary delay of the PG arises from primarily the MOSFET and driver combination, imposing delay times of hundreds of nanoseconds.

To enhance turn-off speed, the output switches incorporate small series gate resistors, $R_{A-D_{2,3}}$, in parallel with Schottky diodes, D_{A-D}. The gate-source resistors prevents switch conduction if high voltage is applied before the isolated driving DC supplies are activated. The complete isolation of both drivers and their respective floating supplies allows a straightforward reversal of polarity. This reversal is achieved by simply switching the terminal of the high-voltage supply connected to ground. However, one of the limiting factors of HV MOSFETS pulse is the maximum switching voltage ($V_{\mathrm{DS,max}}$) which is half of the absolute rating provided by the manufacturer in the half-bridge configuration, $|V_{\mathrm{o,max}}| < |V_{\mathrm{DS,max}}/2|$.

An output monitor has been incorporated at the output of the positive HB. This monitor consists of a resistor divider, comprising a precision high-voltage resistor, $R_{\mathrm{om_2}}$, and a compensation capacitor in parallel, C_{om}. This configuration is designed to compensate for the stray shunt capacitance of the upper resistor, $R_{\mathrm{om_1}}$, ensuring the preservation of fidelity in the rapid timescales of the pulse waveform of resulting scoped low-voltage waveform, V_{om}.

2.3.3 Pulse forming logic

The TTL signals preceding the high-speed optocouplers are generated by means of the low-frequency pulse width modulation, $\mathrm{PWM_{LF}}$. A pair of XOR gates, $X_{1,2}$, generate the true and inverter input signals, $\mathrm{TTL_{ON}}$ and $\mathrm{TTL_{OFF}}$, and are integrated in the same chip, allowing to match the delay of the signals and to create a non-overlap interval to avoid output short-circuit condition. Subsequently, the signals are duplicated by means of logic buffers, B_{1-4}, to provide the ON and the OFF signal to each half bridge.

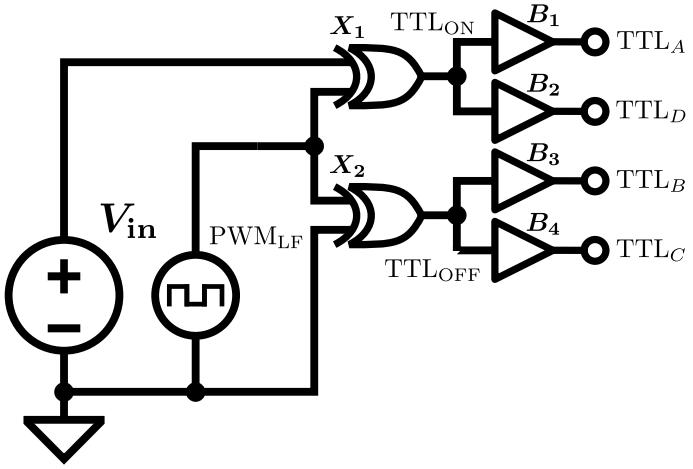

Figure 2.6: Pulse forming logic: schematic.

2.3.4 Operation Intervals

There are eight operation intervals considering the signals propagation delays, as shown in Fig.2.7:

- **Interval 1.** (t_0 **to** t_1): At time t_1, the PWM_{LF} transitions to the ON state, introducing a propagation delay between the rising edge of PWM_{LF} and the falling edge of TTL_{OFF}.
- **Interval 2.** (t_1 **to** t_2): The safety delay is implemented between the falling edge of TTL_{OFF} and the rising edge of TTL_{ON} to prevent any overlapping conditions.
- **Interval 3.** (t_2 **to** t_3): The HBs are switched, producing a delay in the rising time of the HV pulse until it reaches HV DC levels, at which point the HV pulse becomes active.
- **Interval 5.** (t_3 **to** t_4): The HV pulse attains HV DC levels while in the ON state until t_6, influenced by the propagation delays.
- **Interval 6.** (t_4 **to** t_5): At time t_4, the PWM_{LF} transitions to the ON state, introducing a propagation delay between the falling edge of PWM_{LF} and the falling edge of TTL_{ON}.
- **Interval 7.** (t_5 **to** t_6): The safety delay is implemented between the falling edge of TTL_{ON} and the rising edge of TTL_{OFF} to prevent any overlapping conditions.
- **Interval 8.** (t_6 **to** t_7): There is a falling time delay in the HV pulse until it reaches ground levels, at which point the HV pulse transitions to the OFF state.

2.4 Experimental verification

The experimental setup of the HVPG is depicted in Fig.2.8. The main components of the HV-DC/DC are summarized in Tab. 2.2, where for the EI18 transformer, the E core part reference is given. For the HV pulser, IXYS IXTT1N200P3HV MOSFETs and high speed TC4422 drivers were employed, along with 6N137 optocouplers. The input pulse PWM_{LF} is originated from the ATMEGA328 microcontroller embedded in the Arduino. Both the duty cycle and the frequency of the high-voltage pulse can be specified. For the verification, a 1.25% duty cycle and 25 Hz frequency are selected.

To test the HVPG PCB, the high-voltage outputs were connected to the gate electrodes via a coaxial SHV (Safe high voltage) connector. This connection ensures that the casing of the coaxial SHV grounds the HVPG to the vacuum chamber when connected through the feed-through. Fig. 2.9 illustrates the experimental PWM_{LF} input signal and

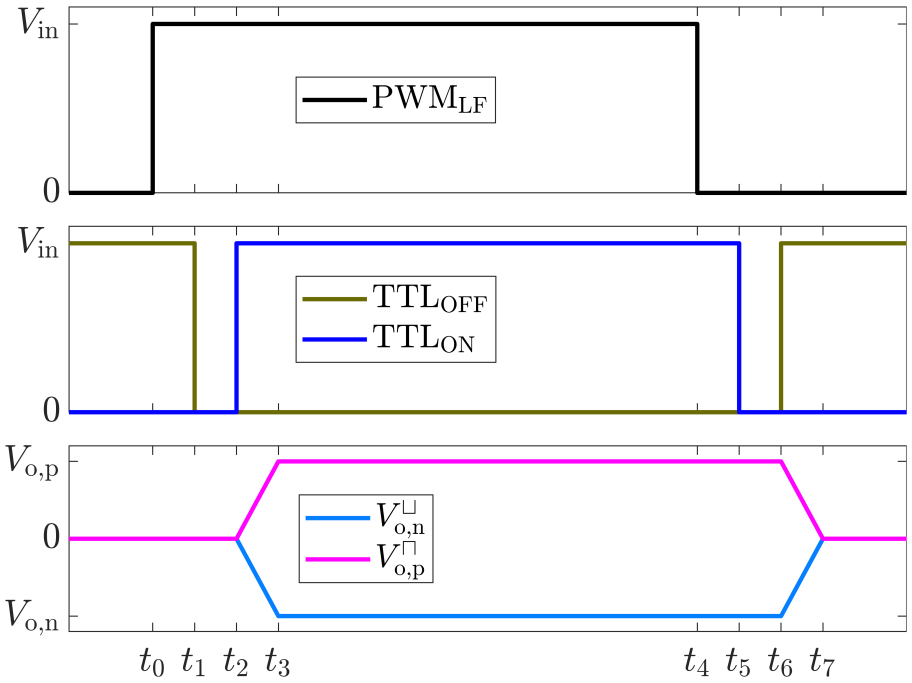

Figure 2.7: Theoretical pulses waveforms showing PWM_{LF} in first plot, TTL_{OFF} and TTL_{ON} in second plot, and $V^{\sqcap}_{\text{o,p}}$ and $V^{\sqcup}_{\text{o,n}}$ in the third plot.

Table 2.2: High-voltage DC/DC components reference

Component	**Identifier**	**Reference**
MOSFET	S_1	IRFR7446TRPBF
Diodes	$D_{p_1} - D_{p_{10}}$ $D_{n_1} - D_{n_{10}}$	BYG23M
Capacitors	$C_{p_1} - C_{p_{10}}$ $C_{n_1} - C_{n_{10}}$	GCJ43DR7LV224KW01K
EI18 Transformer	-	B66283G0000X197

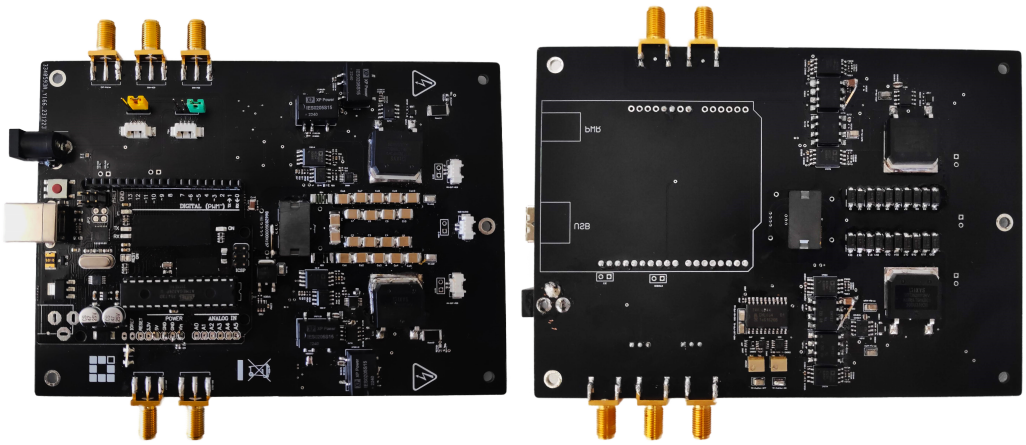

Figure 2.8: Top and bottom view of the HVPG PCB.

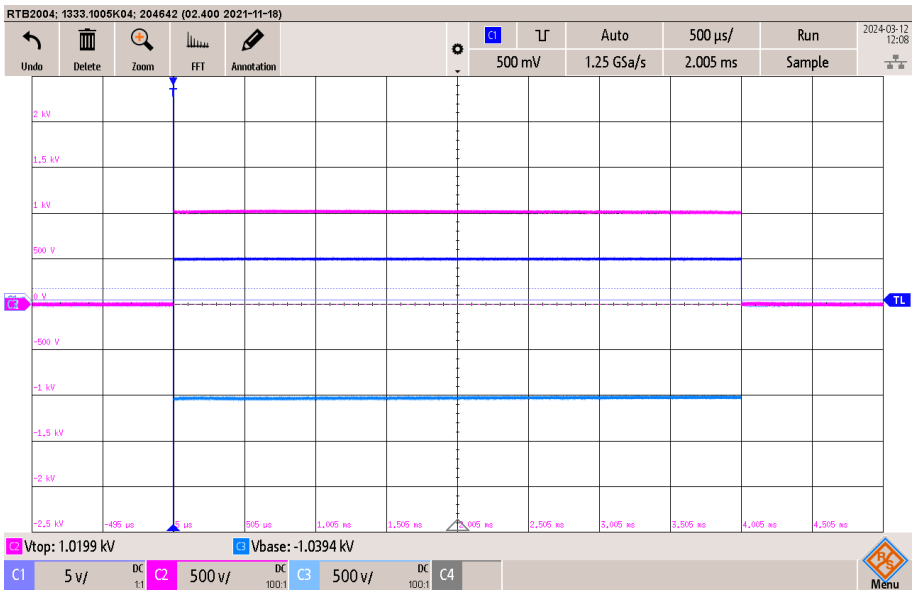

Figure 2.9: Experimental pulse waveforms $\mathrm{PWM_{LF}}$, $V_{\mathrm{o,p}}^{\sqcap}$, and $V_{\mathrm{o,n}}^{\sqcup}$

the high voltage pulse signals $V_{\mathrm{o,p}}^{\sqcap}$ and $V_{\mathrm{o,n}}^{\sqcup}$, as directly obtained from the oscilloscope. Fig.2.10 and Fig.2.11 provide a detailed view of the rising and falling edges, constructed using exported data. Additionally, the experimental high-voltage DC/DC outputs, $V_{\mathrm{o,p}}$ and $V_{\mathrm{o,n}}$, are presented. The high voltage pulse signals exhibit clean rising and falling edges, with ringing and ripple in the range of 10-20 V, which is negligible as it corresponds to approximately 1% of the operating voltage. The oscilloscope used in this work is the Rohde&Schwarz RTB2004 (100MHz - 2.5GSa/s).

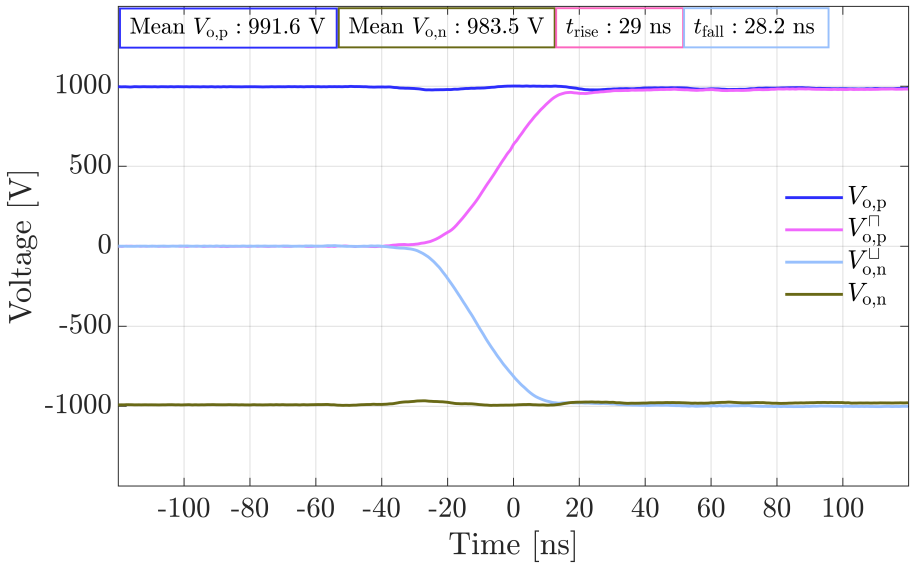

Figure 2.10: Close-up image of rising edge.

The results of the HVPG comply with the estimated requirements, reaching the output voltage without voltage drop and with rise/fall in the vicinity of 30 ns, times much smaller than the requirement of 180 ns. With the selected $L_{\mathrm{ToF}} = 700$ mm, according to Eq.2.6 the

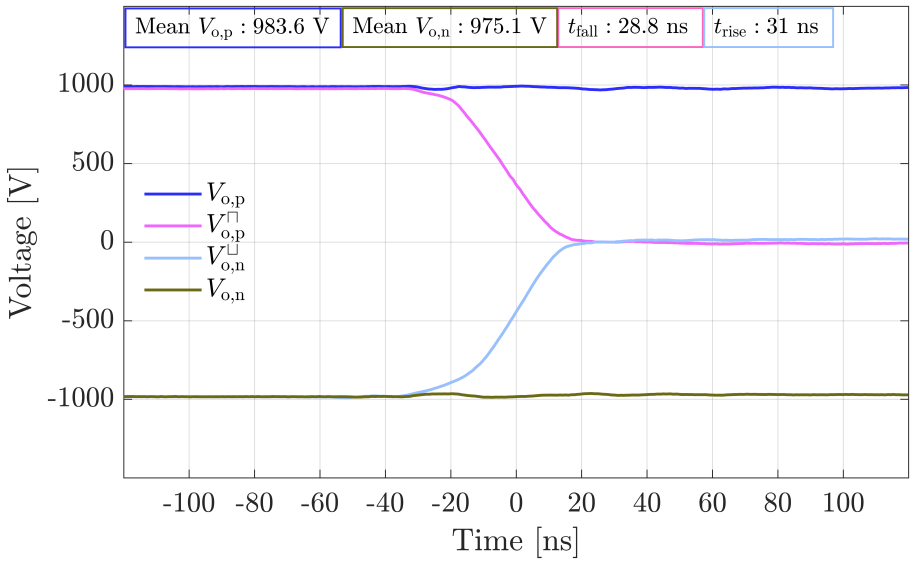

Figure 2.11: Close-up image of falling edge.

energy resolution of the setup is 0.5%. ten times smaller than the one suggested by the literature [70]. Furthermore, the pulse generator underwent testing across various voltage settings, demonstrating consistent small rise and fall times for pulses ranging from 300 V to 1000 V. Fig.2.12 shows how the averaged rise/fall times linearly increase with voltage, but remain below 30 ns for the nominal working voltage of 1 kV.

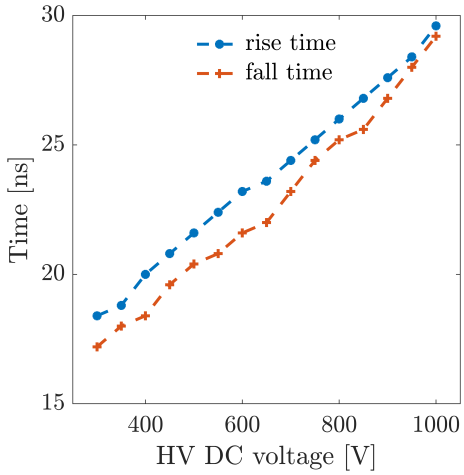

Figure 2.12: Averaged rise and fall times of the pulse generator for different voltages.

2.4.1 Time-of-flight measurements with an electrospray thruster

To completely verify the design, the pulse generator was tested in a real application with an electrospray thruster. An schematic of the geometrical parameters of the device employed is shown in Fig.2.13. It consists of an externally wetted electrospray thruster featuring 101 cones distributed in an hexagonal packaging with 900 μm spacing, 180 μm

height and 30° half-angle, compacting them to an active area of 1 cm^2, a 110 μm tip-to-extractor distance, and a 450 μm extractor holes diameter. The propellant employed is the aforementioned EMI-BF_4, and the operating voltage is set to ±1600 V.

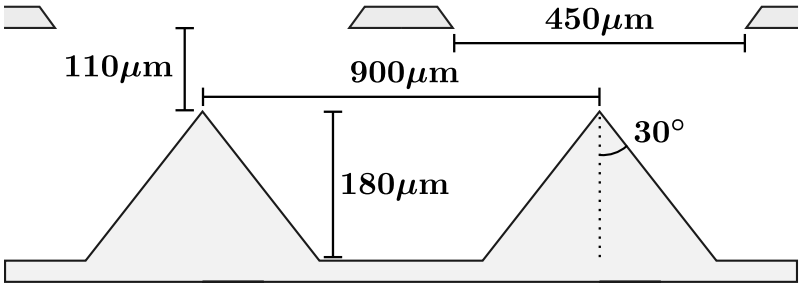

Figure 2.13: Externally wetted electrospray schematic with the geometrical parameters of the thruster prototype.

To validate the ToF setup for characterizing thruster performance, several limitations must be considered. One significant limitation is the divergence of electrospray arrays due to dispersion forces [87], [88], which can reach angles of 40-50° [62], [65], [89]. This divergence implies that the linear ToF configuration can only assess the central performance of the thruster. Additionally, for externally wetted electrosprays, the passive flow control prevents the mass flow rate obtained from ToF measurements from being directly correlated with the actual mass flow rate, unlike in systems with capillary emitters. Nevertheless, the functionality of the HVPG is confirmed, as it effectively drives the electrostatic gate to deflect incoming particles, achieving the primary objective of this study .

The thruster operates using a square pulse that alternates polarities every second, facilitating emission of both positive and negative particles. Synchronization of gate pulses with the flat part of the applied voltage to the thruster is achieved through the HVPG, which offers two methods: utilizing dedicated software to control pulsing via microcontroller PWMs or employing an external pulse generator. In our study, we opt for the microcontroller-driven approach facilitated by our software, which synchronizes both the HVPG and the thruster's HV amplifier. This synchronization is pivotal during polarity switching to maintain standard operation and ensure accurate experimental measurements.

Given the pulse frequency of 25 Hz, approximately 20 measurements are obtained during each polarity cycle. This slightly reduced number ensures data collection occurs within the stable operation phase of the thruster. The emission characteristics of the thruster reveal consistent operation, with emission currents measured at 178 μA during the positive polarity and 115 μA during the negative polarity. For a more comprehensive understanding of the thruster's operational specifics in this experiment, detailed information can be found in [90].

ToF data is presented separately for positive and negative emission cases, as the com-

position of particles in each plume differs. In Fig.2.14, normalized time-of-flight current data is depicted. To mitigate random noise, the displayed traces result from averaging 200 ToF measurements. Analysis of the data reveals two distinct steps, corresponding to the flight times of single ion particles and molecules with one degree of solvation. For a clearer estimation of the particles, charge-to-mass spectra are constructed in Fig.2.15. Known oligomers with discrete values of charge and mass manifest as peaks in the spec-

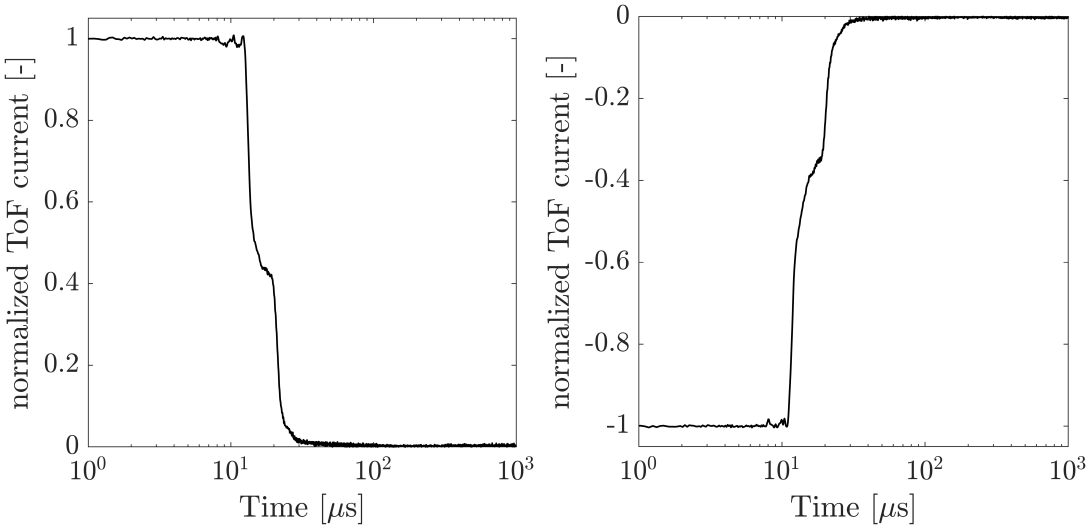

Figure 2.14: Time-of-flight normalized collected current for negative emission versus time.

tra, with a predominance of EMI^+ and BF_4^- species in the plume. This is followed by oligomers with one degree of solvation, such as $EMI^+(EMI\text{-}BF_4)$ and $BF_4^-(EMI\text{-}BF_4)$, and a smaller fraction of more highly solvated molecules. Droplets, if present, would appear as a distribution in the spectra; however, they are not observed in this plume. This condition is referred to as the pure ionic regime [91], characterized by the presence of distinct ion molecules. From a propulsion perspective, this regime enhances propulsive performance efficiency.

The low rise/fall times of the HVPG allow for the observation of molecules resulting from fragmentation [78], occurring between the known particles. Such molecules form when accelerated molecules break down into their constituent particles.

2.5 Conclusions

The paper introduces a novel bipolar high-voltage pulse generator tailored for application in electrospray thrusters time-of-flight mass spectrometry. This proposed generator relies on a bipolar high-gain converter, specifically the Forward-Flyback with Cockcroft-Walton voltage multiplier, which operates from a 5V DC supply. The generator modulates HV rails into pulses through a bipolar kilovolt pulser composed of high voltage MOSFETs and

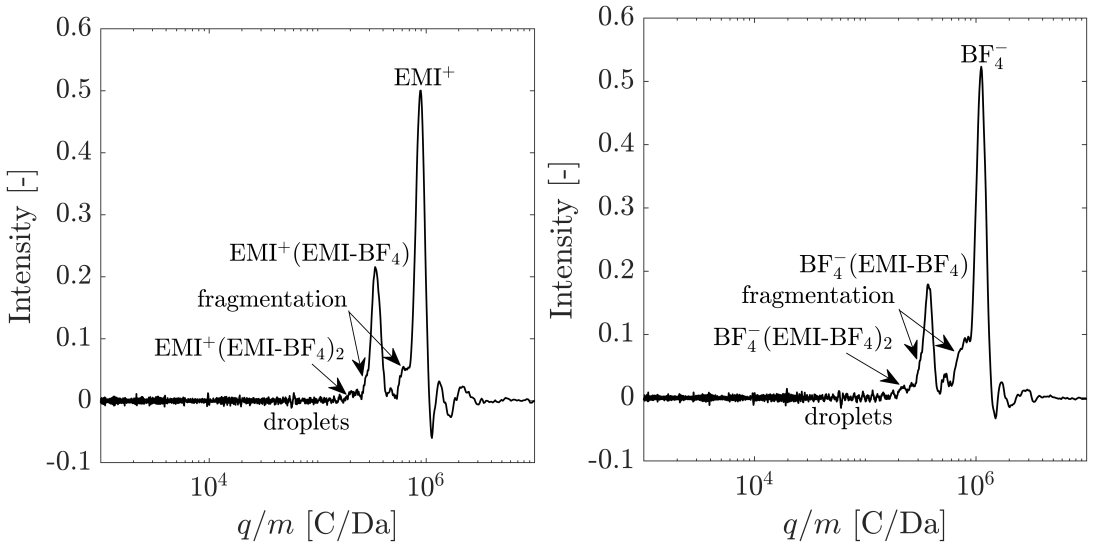

Figure 2.15: Time-of-flight charge-to-mass spectra for positive and negative emission.

high-speed driving circuitry. This modulation is accomplished without inducing voltage drop in the high voltage rails.

The bipolar pulses are synchronized, with a non-overlap interval strategically integrated to avert short-circuit conditions in the pulse forming logic. Experimental validation of the pulse generator corroborates theoretical descriptions, showcasing configurable pulse amplitudes and fast rising and falling pulse times of 30 ns at 1 kV. which constitute the worst case scenario.

Primarily designed to drive the electrostatic shutter gate of a time-of-flight mass spectrometer, this generator proves well-suited for investigating the plume composition of electrospray sources. An experimental characterization of an electrospray thruster has shown the ability of clearly distinguish all the particles present in the plume, including particles formed by fragmentation.

* * *

Chapter 3

Voltage and temperature performance dependence

The content of the current chapter coincides with the following journal paper:

- **D. Villegas-Prados**, J. Cruz, M. Wijnen, S. Correyero, P. Fajardo, J. Navarro-Cavallé, "Impact of propellant temperature on the emission regime of an externally wetted electrospray system using time-of-flight mass spectrometry", Acta Astronautica, vol. 213, pp. 145–155, 2023, doi: https://doi.org/10.1016/j.actaastro.2023.08.045 (**Paper I**).

Paper content and author contribution

This study investigates the characterization of an externally wetted electrospray thruster under varying conditions of applied voltage and propellant temperature. To achieve comprehensive performance characterization, diagnostic tools were developed in alignment with objectives **O.1.1**, **O.1.2**, and **O.1.3**, and subsequently integrated into the vacuum chamber setup (**O.3**). Additionally, to facilitate the controlled heating of the ionic liquid, an assembly incorporating a heater and a feedback-controlled loop was designed (**O.1.5**).

The thruster's emission behavior and propulsive performance were analyzed across a range of operating voltages (**O.2.1**) and propellant temperatures (**O.2.2**), addressing the research gap identified as **G.3**. Furthermore, this study correlates the findings to the minimum flow rate required to achieve the desired pure ionic regime, drawing conclusions on the impact of ionic liquid properties and operating conditions on this regime. Notably, this research represents the first reported temperature-dependent characterization of externally wetted electrosprays using time-of-flight diagnostics (**G.1**).

The candidate contributed to the development of the vacuum setup, including all diagnostic tools and the thruster assembly, the execution of experiments, and the post-processing and extraction of meaningful insights from the results. This research has been published in Acta Astronautica (**O.4**).

* * *

3.1 Abstract

Electrospray thrusters operate in different regimes depending on the ejected particles: pure ionic regime, characterized by the presence of only solvated ions; droplet regime; and mixed regime, where both ion and droplets are emitted. The electrospray emission regime is driven by the physical properties of the liquid, the flow rate to the emission site, and the electric field applied. Because of the temperature dependence of the ionic liquid, the emission regime and hence the propulsive performance are sensitive to the liquid temperature. Additionally, in externally wetted electrospray emitters, where the flow rate is passively controlled by viscous forces, temperature plays a crucial role as it drives the hydraulic impedance of the emitter due to the variation of the liquid's viscosity, and therefore the emitter flow rate. The research described in this work is focused on the effect of the propellant temperature on the emission regime of externally wetted emitters. By means of a time-of-flight mass spectrometer the plume composition has been analyzed under different conditions of applied voltage and operating temperature, finding that voltage increases the relative amount of ion species and temperature increases the relative amount of droplets.

Nomenclature

a	distribution step height
c	distribution median
e	elementary charge
E_n	normal electric field
$E_{\max}$	maximum electric field
E^*	critical electric field
f^I	current fraction
f^M	mass fraction
F_{ToF}	time-of-flight thrust
h	Planck's constant
h_c	cone height
I_{ToF}	time-of-flight collected current
I_e	emitted current
I_{sp}	specific impulse
K	liquid conductivity
K_{ps}	permeability of surface layer
L_{ToF}	time-of-flight length
ΔG_S	activation energy
Δp	pressure drop
j_e	current density
k_B	Boltzmann constant
N_e	number of emitters
Q	flow rate
Q^*	critical flow rate
ρ	liquid density
R_c	emission region radius
σ	local surface charge density
s	distribution standard deviation
t	time of flight
θ	cone semi-angle
T	liquid temperature
v_i	particle's velocity
ε	liquid dielectric constant
ε_0	vacuum permittivity
η_p	polydispersive efficiency
μ	liquid viscosity
x	mass vector
$\dot{m}$	mass flow
γ	liquid surface tension

Acronyms/Abbreviations

EMI-BF_4	1-Ethyl-3-methylimidazolium tetrafluoroborate
EMI-Im	1-Ethyl-3-methylimidazolium bis(trifluoromethylsulfonyl)imide
EP	Electric Propulsion
ESG	Electrostatic Shutter Gate
IL	Ionic Liquid
PIR	Pure Ionic Regime
SER	Secondary Electron Repeller
TIA	Transimpedance Amplifier
ToF	Time-of-Flight

3.2 Introduction

Electric rocket propulsion (EP) is a type of propulsion system that uses electric power to accelerate a spacecraft or vehicle. Unlike traditional chemical propulsion systems, which burn fuel to create a hot gas that thermally expands out of a nozzle to create thrust, electric propulsion uses charged propellants and electric or magnetic fields to accelerate the particles and generate thrust [92].

One of the key advantages of electric propulsion is the high specific impulse which results in high fuel efficiency. From the Tsiolkovsky rocket equation, $\Delta v = I_{sp} g_0 \ln(m_0/m_f)$, either the spacecraft can achieve the target Δv with less propellant mass leading to a reduced launch mass or the spacecraft can achieve more demanding missions in terms of Δv. These benefits have made electric propulsion increasingly important for both commercial and scientific space missions. Among the electric propulsion systems, electrospray propulsion systems have gradually attracted the attention of the EP community due to their small size, high efficiency and high thrust-to-power, becoming more suitable for micro and nano satellites since they can retain higher efficiencies ($> 50\%$) even in the low power range (< 100 W), contrary to ion or hall thrusters [3], [93]–[95]. The first successful in-space demonstration of electrospray propulsion was achieved in 2015 by Busek and NASA Jet Propulsion Laboratory on board the of the European Space Agency Laser Interferometer Space Antenna Pathfinder mission [50].

Electrospray propulsion systems are based on the extraction and acceleration of charge particles from a conductive liquid [79]. The propellant wets a substrate, called emitter, located closely to an extractor grid. An electric potential difference is established between the liquid and extractor grid. At sufficiently high values of the resulting electric field, ions may be extracted from the emission site by the field-emission or Taylor cone phenomenon; the electric field accelerates said ions to a high speed jet, producing thrust [96]. Fig. 3.1 shows the schematic of an an electrospray source. Depending on the emitter morphology, they can be grouped into: capillary [97], externally wetted [59] or porous [52].

This type of propulsion often uses ionic liquids (ILs) as propellant, which are molten salts composed of chemically stable mixtures of positive and negative molecular ions. One of the key advantages of ILs is their negligible vapor pressure which makes them suitable for space applications. Additionally, the emission of both positive and negative ions allows for net neutral emission without the need of a neutralizer [68], which is an advantage with respect to field-emission electric propulsion. From the propulsive point of view, the propellant choice becomes extremely relevant for the overall performance of the thruster.

Three different emission regimes or operation modes have been reported in the literature for electrospray thrusters: pure ionic regime (PIR), where only ions are sprayed; droplet regime, where clusters of ions are emitted; and mixed regime, containing both ions and droplets in the plume. Generally, droplets are heavier, hence their presence tends

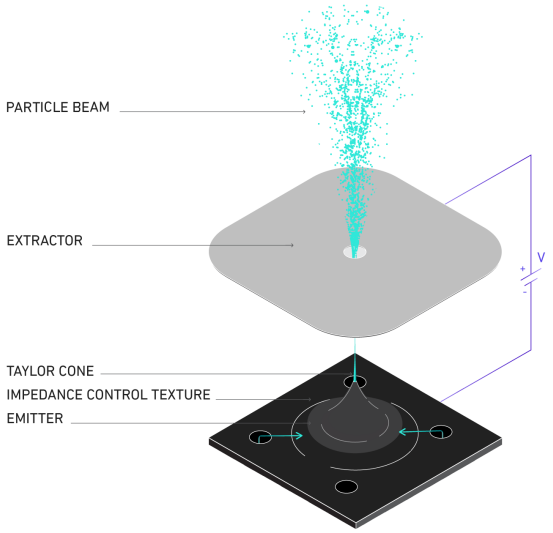

Figure 3.1: Schematic of a single emission site externally wetted electrospray source.

to increase the thrust but penalize the specific impulse of the thruster. On the other hand, PIR is characterized by a lower thrust but high specific impulse. In the mixed regime there is a penalty for emitting particles with very different specific charges, leading to a lower thrust efficiency. Both the pure droplet and pure ionic regime however have very high thrust efficiencies [32], [64].

The purpose of the present study is to improve the understanding of the emission regime of externally wetted electrosprays. The thruster analyzed in this work is an IENAI SPACE prototype (ATHENA). In particular, the performance of the thruster for different operating voltages and operating temperatures has been assessed by varying the propellant reservoir temperature with a controlled heater. The beam composition has been analyzed by the time-of-flight mass spectrometer (ToF) technique, a diagnostic specifically adapted to the characteristics of the thruster. The rest of the article is organized as follows: Section 3.3 assesses the theoretical framework on emission regimes, Section 3.4 presents the experimental set-up, Section 3.5 and Section 3.6 discusses the obtained results and Section 3.7 summarizes the conclusions extracted.

3.3 Theory on ionic emission

The emission mode in which an electrospray operates depends on the physical properties of the liquid, the propellant flow rate to the emission site and the electric field generated at the tip.

In order to achieve ionic emission, ions must overcome an energy barrier to escape the liquid. If the electric field is not strong enough to trigger ion emission, the electrospray may still operate as a cone-jet, where the total or a majority of the jet is composed by droplets [98], [99]. The ion evaporation effect was first described by [100],

$$j_e = \sigma \frac{k_B T}{h} \exp\left[-\frac{\Delta G_S - G(\mathrm{E}_n)}{k_B T}\right] \quad \text{with} \quad G(\mathrm{E}_n) = \left(e^3 \mathrm{E}_n / 4\pi\varepsilon_0\right)^{1/2} \tag{3.1}$$

where j_e is the current emitted per unit surface area, σ is the local density of surface charge, k_B is Boltzmann's constant, T is the liquid temperature, h is the Planck's constant, e is the elementary charge, ε_0 is the permittivity of vacuum, ΔG_S is the activation energy barrier for solvated species and takes values of 1-2 eV [101], E_n is the normal component of the electric field on the surface and $G(\mathrm{E}_n)$ is the Schottky hump. For temperatures of interest, $\Delta G / k_B T$ is large and ion evaporation begins when $\Delta G_S - G(\mathrm{E}_n) = O(k_B T)$ [102]. The critical electric field, E^*, arises from the condition $G_S - G(\mathrm{E}_n) < 0$,

$$\mathrm{E} > \frac{4\pi\varepsilon_0 \Delta G_S^2}{e^3} = \mathrm{E}^* \tag{3.2}$$

which results in $E^* \sim 1$ V/nm. Reaching the critical electric field strongly depends on the liquid properties. [103] showed that pure ionic regime is favored by ILs of high electrical conductivity, and high surface tension. For capillary emitters, PIR operation was restricted to ILs at or near room temperature having surface tension in the range of 40 mN/cm, and electrical conductivity in the order of 1 S/m [104], with EMI-BF_4 (1-ethyl3-methylimidazolium) as one of the most commonly used liquids. [70], and later confirmed by [105], noted that externally wetted emitters have the advantage over capillary emitters of being able to achieve ionic emission with ILs with relatively modest surface tensions and electrical conductivities. The scaling law as derived by [48], for the structure of cone-jets indicate that the maximum electric field on the surface of the meniscus for a particular liquid is given by,

$$\mathrm{E}_{\max} = \varphi(\varepsilon) \gamma^{1/2} \varepsilon_0^{-2/3} (K/Q)^{1/6} \tag{3.3}$$

where γ is the surface tension of the liquid, K is the electrical conductivity of the liquid, Q is the flow rate of liquid to the emission site and $\varphi(\varepsilon)$ is a coefficient dependent on the dielectric constant ε. The smallest value that Q can take to ensure stability of the Taylor cone scales as $1/K$ [69], and the maximum electric field generated is proportional to, $\mathrm{E}_{\max} \sim \gamma^{1/2} K^{1/3}$, confirming the role of high γ and K to attain high electric fields [103], and therefore to produce ionic emission.

Another important characteristic to reach the pure ionic regime is to restrict the flow rate below a critical value, $Q < Q^*$ [91]. [106] derived two expressions for the critical flow rate depending on whether polarization forces ($\varepsilon\delta_\mu > 1$) or viscous forces ($\varepsilon\delta_\mu < 1$) dominate the cone-jet transition,

$$\begin{aligned} Q^* &= \frac{\gamma \varepsilon_0 \varepsilon}{\rho K} && \text{if } \varepsilon\delta_\mu > 1 \\ Q^* &= \frac{\mu \gamma^{1/3} \varepsilon_0^{2/3}}{\rho^{4/3} K^{2/3}} && \text{if } \varepsilon\delta_\mu < 1 \end{aligned} \tag{3.4}$$

where $\delta_\mu = \left[\gamma^2 \rho \varepsilon_o / \left(\mu^3 K\right)\right]^{1/3}$, ε is the dielectric constant of the liquid, μ the viscosity of the liquid and ρ the density of the liquid. For the case of EMI-Im (the IL used throughout this work), the parameter $\varepsilon\delta_\mu \sim 10^{-2}$ [107], so that the critical flow rate scales as described in Eq. 3.4 when $\varepsilon\delta_\mu < 1$. This relation shows that high values of γ will favor ionic regime as Q^* increases. 0n the other hand, for high value of K, Q^* decreases. From the critical electric field and flow rate conditions, the emission mode of an electrospray can be summarized as follows: pure ionic regime will be achieved if E > E* and $Q < Q^*$, while droplet mode is characterized by E < E* and $Q > Q^*$. If both the electric field and flow rate are above the critical values, the mixed regime is encountered, and if they are below the critical values no emission from the electrospray is obtained.

In capillary emitters the flow rate, and therefore the emission regime, can be actively controlled. However, in externally wetted emitters there is no direct control of the liquid flow rate. It is controlled passively through geometric parameters, the most important being the surface roughness [108]. The latter controls the wettability and hydraulic impedance for the fluid moving towards the emission site, hence controlling indirectly the flow rate. The relationship between the pressure drop, Δp, and the flow rate for an externally wetted emitter was derived by [26], and can be related to the hydraulic resistance, R_H, by the Hagen-Poiseulle law,

$$\Delta p = \frac{\mu}{2\pi K_{\text{ps}} \sin\theta} \ln\left(\frac{h_c}{R_c}\right) Q = R_H Q \tag{3.5}$$

where θ is the cone semiangle, R_c is the base of emission region and it is typically of the order of $10^0 - 10^{-1}$ μm [102], and h_c the height of the emitter. and K_{ps} is the permeability of the surface layer [m^3]. This last parameter affects the thickness of the liquid layer and has dependence on μ [109]. From this equation, it is clear that for a fixed emitter geometry (K_{ps}, θ, R_c, and h_c) and pressure drop, the flow rate is driven by the viscosity of the liquid. If the viscosity decreases, the hydraulic impedance decreases, hence increasing the flow rate promoting droplet formation.

3.3.1 Temperature dependence

During operation in LEO, a satellite can reach temperatures from -20°C up to 60°C [110]. This can affect the operation of electrospray thruster as the physical properties of ionic liquids are temperature dependent. For instance, conductivity increases, while surface tension decreases when the liquid temperature is increased [111]. Also, it is reported that some ionic liquids freeze at temperatures above 0 °C, for example EMI-BF_4 has a freezing point of approximately 12.0-12.5 °C (although it often tends to supercool [112]), presenting an operational constraint. These changes in temperature can lead to inadvertent changes in emission regime or even prevent any emission. For that reason, for electrospray thrusters to become reliable systems, it is crucial to understand the effects of temperature on their operation.

The first temperature studies on externally wetted emitters were carried out by [58] using EMI-BF_4, finding that for the same voltage, current increases roughly linearly with temperature. Emitted current increased by a factor of two when the temperature changed from 25 to 50 °C. The EMI-BF_4 viscosity is roughly halved for this temperature range. Lozano suggested that emission is limited by viscous transport, which is inversely proportional to the liquid viscosity, as suggested also by the derivation in Eq. 3.5. [70] also noted that wettability of EMI-Im was improved by heating the emitter to temperatures around 80 °C.

The ion current emitted from a surface has a strong dependency on the temperature as shown in Eq. 3.1, suggesting that increasing temperature favors the emission of ion current. In the field of capillary emitters, [71] showed with time-of-flight spectra that the mass-to-charge ratio increases with beam current at constant emitter temperature, and decreases with increasing temperature. The potential of increasing the temperature to improve propulsive parameters was also studied by [77], finding that relatively modest changes in temperature ($\Delta T \sim 20°C$) result in significant reductions of the jet diameter and the droplet mass-to-charge distributions under comparable spray currents, leading to substantial increase in specific impulse. Although this statement holds true for capillary emitters, where the flow rate is actively controlled, it is unclear how the temperature affects the average mass-to-charge ratio and the conditions to achieve pure ionic regime in externally wetted emitters, where the flow rate is passively established. Ionic emission should be favored by the temperature increase as the electric field intensifies. However a decrease of the liquid viscosity, decreases the hydraulic impedance increasing the flow rate, resulting in droplet emission, leading to a mixed or pure droplet regime.

3.4 Experimental set-up

3.4.1 Thruster assembly

The thruster assembly of the electrospray propulsion system used in this study consists of an extractor grid and an externally wetted emitter array; both micro-fabricated in silicon. The emitter features an array of $N_e = 101$ micro cones with a nano-texturization, which wicks the fluid to the emitters tips and controls the hydraulic impedance. The emitter contains numerous feeding holes, such that the ionic liquid can passively flow from the reservoir to the emitter. A filter-paper cloth is added between the emitter and the reservoir to ensure a continuous liquid connection. The reservoir consists of a 3D printed porous aluminum piece that can hold 45 μL of liquid. A polyimide heater with cross-section equal to the reservoir and 0.2 mm thickness is placed right below and in contact with it. A PT100 temperature sensor is placed on one of the sides of the reservoir. With this set-up, the liquid is heated indirectly by the reservoir. A control loop is used to maintain the reservoir at the desired temperature. The extractor grid is biased to ground and the

voltage is applied to the metallic reservoir. A schematic of the thruster assembly is shown in Fig. 3.2a and a photo of the assembly in Fig. 3.2b.

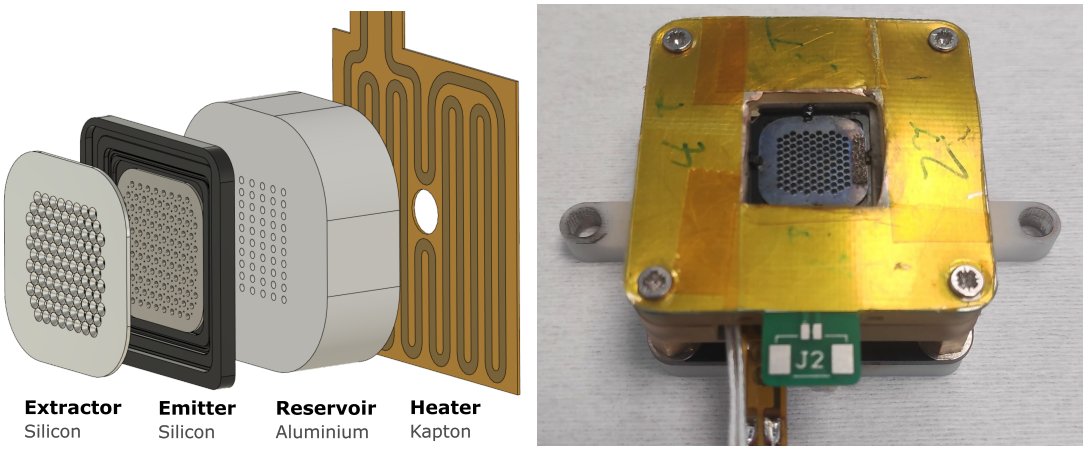

(a) Schematic of thruster assembly.

(b) Thruster after assembly

Figure 3.2: Thruster head schematic (a) and assembly image (b).

3.4.2 Propellant selection

The ionic liquid used in this work is 1-Ethyl-3-methyl-imidazolium bis-trifluoromethylsulfonyl-imide, also known as EMI-Im or EMI-NTf_2 in the literature. Ionic liquids are room temperature molten salts composed of positively charged cations and negatively charged anions. The ions emitted can be single molecules, degree of solvation $n = 0$, as well as ions with a higher degree of solvation, mainly $n = 1$ (dimers) or $n = 2$ (trimers); higher degrees of solvation are possible but rare. Throughout this work, particles with a mass larger than that of trimers' are considered droplets. Tab. 3.1 lists the molecular masses of the ions and oligomers.

Table 3.1: Molecular masses of 1-Ethyl-3-methyl-imidazolium bis-trifluoromethylsulfonyl-imide

Cation	mass$^+$ [Da]	**Anion**	mass$^-$ [Da]
EMI^+	112	Im^-	280
$[EMI\text{-}Im]EMI^+$	504	$[EMI\text{-}Im]Im^-$	672
$[EMI\text{-}Im]_2EMI^+$	896	$[EMI\text{-}Im]_2Im^-$	1064

The high conductivity, high surface tension and negligible vapor pressure make EMI-Im a promising propellant. Also it is much less hygroscopic than for example EMI-BF_4 and therefore absorbs less water which can cause problems in vacuum [113]. It is a common IL in electrospray propulsion with flight heritage [50] and has been used with externally wetted emitters [55], [70]. For capillary emitters, EMI-Im has been found to operate in the mixed regime [71] and for externally wetted emitters, tests at room

temperature have been operated in pure ionic regime [70]. A summary of the relevant liquid properties with temperature is shown in Tab. 3.2

The sample used of EMI-Im has a purity > 99% and it has been kept inside an hermetic box in a clean-room environment (ISO 7) prior to tests to ensure minimum water absorption. In addition, the liquid was outgassed for a day at 10^{-6} mbar prior to filling the thruster to avoid explosions of water vapour bubbles during the thruster operation.

Table 3.2: Properties of 1-Ethyl-3-methyl-imidazolium bis-trifluoromethylsulfonyl-imide at different temperatures. Temperature (T), density (ρ), conductivity (K), viscosity (μ), surface tension (γ) are shown. Values are obtained from [114]–[116]. The critical flow rate per emitter as calculated with Eq. 3.5 is also given.

T [°C]	ρ [g·cm^{-3}]	K [S·m^{-1}]	μ [mPa·s]	γ [mN·m^{-1}]	Q^* [pL·s^{-1}]
20	1.524	0.774	36.5	33.79	3.41
30	1.513	1.063	25.7	32.86	1.95
40	1.503	1.398	19.05	31.99	1.20
50	1.493	1.775	14.65	31.16	0.79
60	1.484	2.187	11.39	30.34	0.53

3.4.3 Vacuum facility and diagnostics

The vacuum facility consist of a 290 mm sided cube, with a 775 mm long and 97 mm inner diameter extension tube located along the central axis of one cube face. An Edwards 85 L/s turbo-molecular pump maintains a chamber pressure < 10^{-5} mbar. The results from a time-of-flight mass spectrometer test campaign are presented in this work. Fig. 3.3 shows an schematic of the set-up.

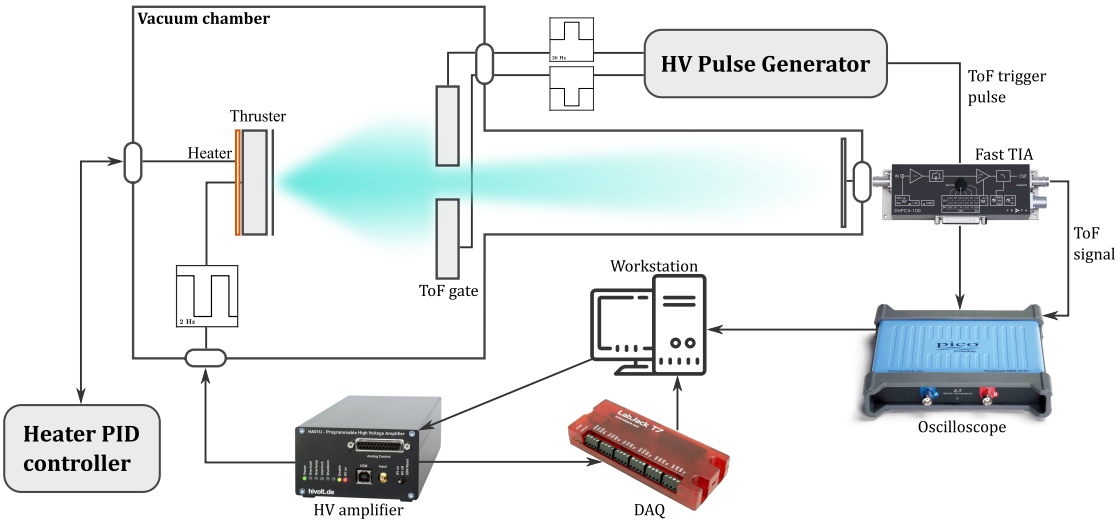

Figure 3.3: Experimental set-up including vacuum chamber and electrospray source with heater.

Time-of-Flight mass spectrometry

The ToF is used to characterize the composition of the thruster ion beam. In electrospray propulsion, it is one of the most important diagnostics as it allows for identifying the different emitted particles and their contribution to the total emitted current. From this, the average specific charge, q/m, as well as an indirect estimation of the thrust and specific impulse can be obtained.

ToF mass spectrometers provide the mass distribution of the ion beam by measuring a time wave of the charged particle beam current modulated by an electrostatic gate. The ions travel through a section of known length, L_{ToF}, called the flight region. The time taken by each particle, i, is then,

$$t_i = \frac{L_{\mathrm{ToF}}}{v_i} = \frac{L_{\mathrm{ToF}}}{\sqrt{2(q/m)_i V_a}} \tag{3.6}$$

where V_a is the applied voltage. The mass spectrometer built in this work is similar to other ToF set-ups in the literature [70]. It consists of a deflection gate driven by a high-voltage pulse generator and a collector plate placed at the end of the flight region. The collected current is then measured with a high-speed trans-impedance amplifier (TIA). A secondary electron repeller (SER) is added in front of the collector. A schematic of the ToF is shown in Fig. 3.4.

The ToF gate acts as an electrostatic shutter, and it is placed close to the thruster exit plane. When the electrostatic gate (ESG) is polarized, it deflects all upstream particles; only the particles already downstream will be collected. Since particles have different velocities (due to different specific charges) they will reach the collector at different times, those with the highest velocities arriving first (Fig. 3.5). The deflection gate operates by applying an electric field perpendicular to the particle beam, created by means of two biased plates. The collection angle of a 90 mm diameter detector and a flight length of 796 mm is 3.2°. When the deflection angle of the ESG exceeds the collection angle, none of the upstream particles will reach the collector and the gate is effectively ‘closed’.

The collector consists of a 1 mm thick aluminum disk connected to a single sided BNC feed-through. At 5 mm upstream from the collector, a SER is placed consisting of two meshes with 70 % transparency, spaced 5 mm. The first mesh is grounded directly to the vacuum chamber by means of conductive tape. The second mesh is biased to -10V using an external power supply.

A fast TIA is connected directly to the feed-through, minimizing the input capacitance and corresponding current noise. The TIA used in this work is a DHCPA-100, a variable gain high bandwidth amplifier. The TIA was operated with a gain of 1 MOhm in low-noise mode, resulting in a bandwidth of 1.8 MHz. This corresponds to a minimum rise time of 194 ns. The HV pulse generator driving the ESG was developed in-house and its architecture is based on a design from [86]. The circuit consists of two half bridges

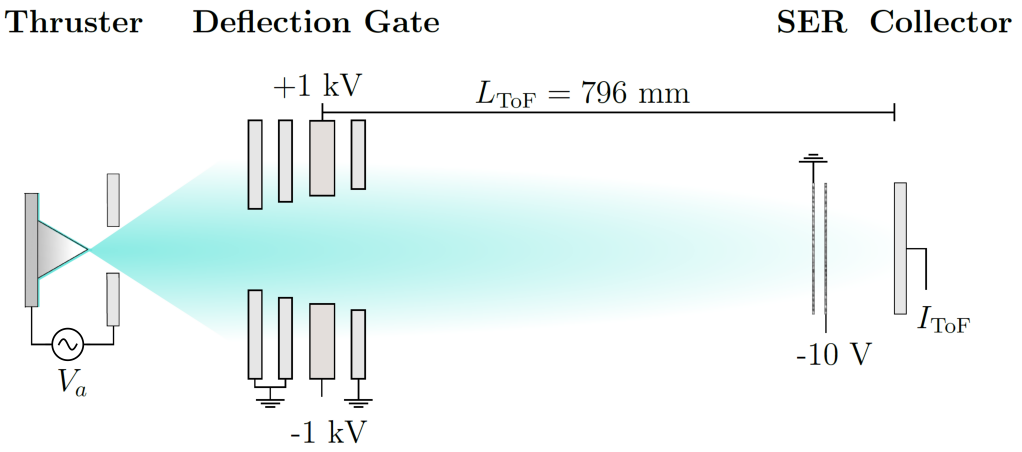

Figure 3.4: Schematic of time-of-flight electrostatic gate set-up.

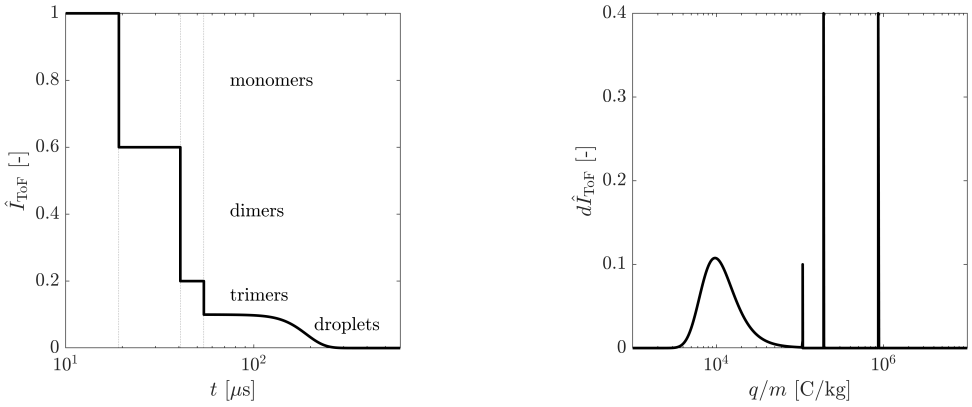

(a) (b)

Figure 3.5: a) Theoretical ToF timewave for a monoenergetic 1000 V EMI-Im ion beam operating in mixed regime with composition: 40% monomers, 40 % dimers, 10 % trimers and 10 % droplets with an arbitrary m/q distribution, and b) theoretical derivative of the ToF timewave as a function of the specific mass.

that switch the output between a high voltage output and ground. It can bias the gate electrodes to ± 1 kV respectively (resulting in a 2 kV differential voltage) with a 180 ns rise time.

3.4.4 Thruster operation

When the magnitude of the applied voltage is the same for both negative an positive polarity, the magnitude of the current of the positive emission tends to be higher than that of the negative. To avoid charge accumulation with time, the thruster was driven with a square wave in the positive polarity for a fixed time $t^+ = t_1$ and variable duration $t^- = t_2 - t_1$ in the negative polarity until the time integral of the positive and negative emitted currents matches (i.e. $\int_0^{t_1} I_e^+ dt = \int_{t_2}^{t_1} I_e^- dt$). Voltage polarity was changed at a rate of 2 Hz to avoid electrochemical reactions [117], so that $t^+ = 0.5$ s and $t^- = t^+ (I_e^+ / I_e^-)$.

An schematic of the square wave used is shown in Fig. 3.6. The time t_2, is updated in real time during each cycle to fulfill the relation.

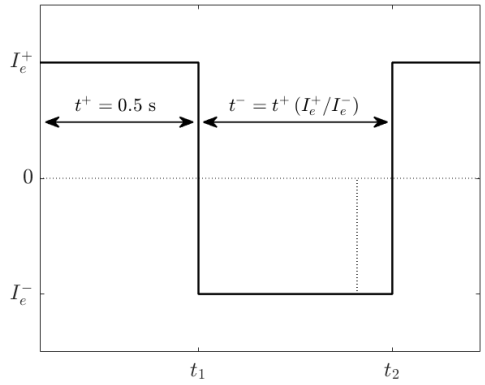

Figure 3.6: Current compensation methodology to avoid electrochemical reactions. Positive polarity has a fixed time. Negative polarity has variable time depending on current emission levels.

The measurements were performed at three different temperatures: T = 30, 40 and 50 °C. At each temperature point, a 20 min delay was introduced before measuring to ensure stabilization of the liquid temperature. This stabilization time was previously corroborated with emission tests, by checking the time needed to stabilize the emitted current for a given temperature. Once stable, the emitter was operated at 11 different operating voltages, from 1000 V to 1500 V every 50 V.

3.5 Results and discussion

3.5.1 Emission characteristics

For every temperature, an I-V curve was measured by sweeping the voltage with a triangular waveform from -1500 V to 1500 V with a 5 s rise time. The curves in Fig. 3.7 are obtained by averaging four I-V curve measurements. For both positive and negative applied voltage, the current increases first exponentially and then linearly. This is the expected behavior of an externally wetted emitter with sufficiently high hydraulic impedance, as reported by [62]. At the different temperatures, the averaged maximum emitted currents at 1500 V are 323, 511, and 673 μA, respectively. At -1500 V, these are 242, 378 and 494 μA, respectively, showing the asymmetry of the emitted current for positive and negative emission. Moreover, increasing the temperature from 30 to 50 °C results in a current increase of a factor of two, approximately, for both polarities.

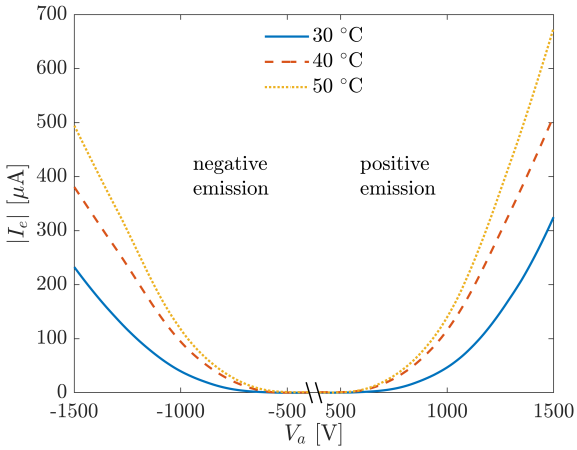

Figure 3.7: Absolute emitted current, $|I_e|$, vs applied voltage, V_a, at the three operating temperatures.

3.5.2 Time-of-flight mass spectrometry

During the ToF measurements, the thruster was operated using the square waveform explained in Section 3.4.4. For all the experiments carried out in this work, the spray of EMI-Im was always composed of a combination of ions and charged droplets. The flight times in the measurements are transformed into ion masses with Eq. 3.6, assuming that all particles have charge e. This is performed for convenience in the plots, as ion masses are known, but is technically not true for droplets which distribution of m/q is formed by droplets of varying masses and varying charge. Each trace is the result from averaging 200 ToF measurements. The curves have been fitted using a combination of log-normal cumulative distribution functions [97], [118], as presented in Eq. 3.7. Although this approach has been primarily used for capillary emitters, the droplets encountered during our experiments show similar spread and mean q/m, validating the use of this fit.

$$\hat{I}_{\mathrm{ToF}}(\mathrm{Da}) = \sum_{i=1}^{N} \frac{a_i}{2}\left[1 + \mathrm{erf}\left(\frac{\log x - c_i}{s_i\sqrt{2}}\right)\right] \tag{3.7}$$

where x is the mass vector, a_i is the step height or the current contribution of each specie, s_i is the standard deviation of the distribution, and c_i is the median value of the distribution. The measurements show four different populations ($N = 4$). Three steps coinciding with the ion species present in the plume: monomers, dimers and trimers, and a fourth distribution corresponding to droplet population ($i = 4 =$ drop). In the case of solvated ions, their mass is known and the median value is then $c_i = \log m_{\mathrm{ion}}$, but for the droplets c_{drop} is unknown.

Fig. 3.8 shows the ToF spectra normalized at fixed applied voltage for positive and negative emission for the three temperatures considered. Fig. 3.9 shows the ToF curves normalized at fixed operating temperature for positive and negative emission and three fixed voltages. The dashed black lines coincide with the curve steps and correspond to the theoretical masses of the solvated ions ($n = 0, 1, 2$) as given by Tab. 3.1.

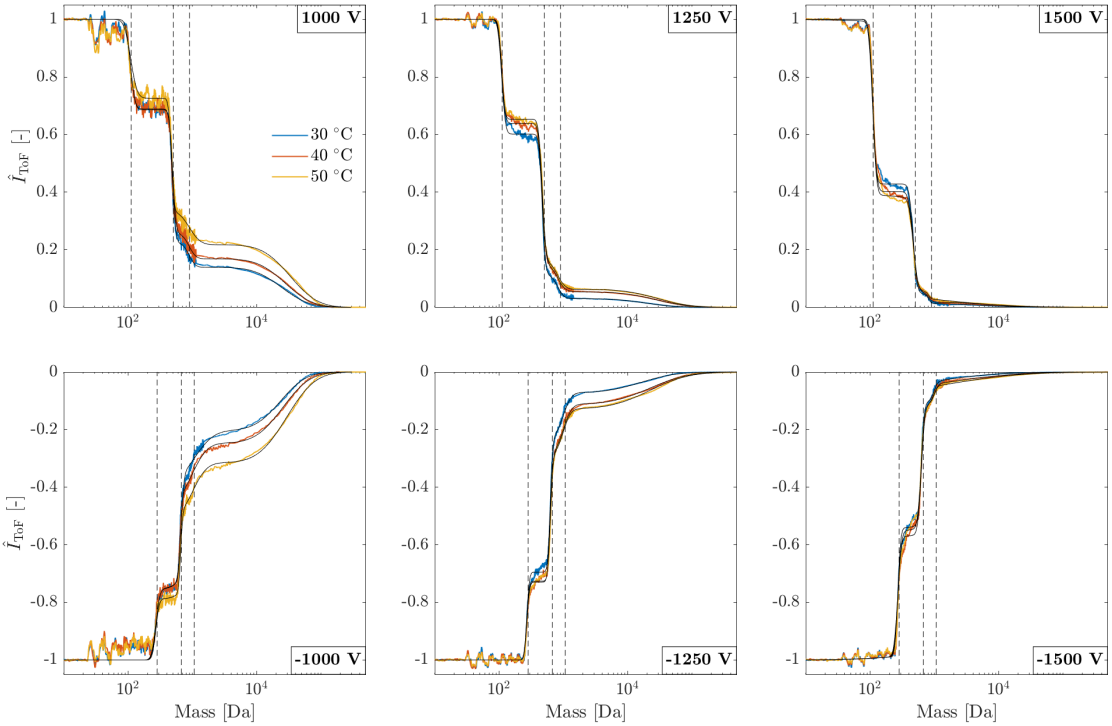

Figure 3.8: Experimental time of flight spectra at 30, 40 and 50 °C and constant applied voltage (1000, 1250 and 1500 V are shown). Positive polarity corresponds to positive applied voltages and negative polarity to negative applied voltages. Fitted curve for each data set is plotted as the black trace. Dashed black lines indicate the theoretical masses of the different oligomers (monomers, dimers and trimers).

Fig. 3.10 gathers the current fraction, f_i^I, and mass fraction, f_i^M, of monomers and droplets present in the spectra for positive and negative emission. These magnitudes are computed using the fitted curves. The current fraction of each particle corresponds to the fitting parameter a_i. The mass fraction contribution of each specie is estimated as, $f_i^M = a_i m_i / \sum_{i=1}^{N} a_i m_i$, where the mean mass of the droplets is calculated according to $\langle m_{\mathrm{drop}} \rangle = \exp(c_{\mathrm{drop}} + s_{\mathrm{drop}}^2/2)$.

At fixed temperature, the results clearly show a mixed regime at lower voltages tending to predominantly ionic emission when the voltage is increased. In terms of current, at 30 °C monomers account for 32 and 25 % at 1000 V, for positive and negative polarities respectively, compared to the 61 and 45 % at 1500 V. Increasing the voltage not only allows for achieving higher emitted currents, but increases the evaporation of ions from the cone tip as the electric field increases. At 1000 V, although the droplet current fraction is ~14 %, droplets account for 93 % of the mass of the beam. The presence of these heavy and slower, particles penalizes strongly the thruster performance, as will be discussed in Section 3.6. Even at 1500 V, the 2 % of current carried by droplets corresponds to 31 % of the total mass. Comparing both polarities, the Im^- molecule consistently exhibits a greater amount of droplets compared to EMI^+ for the same voltage and temperature.

When keeping the voltage constant, the results show that an increase of the liquid

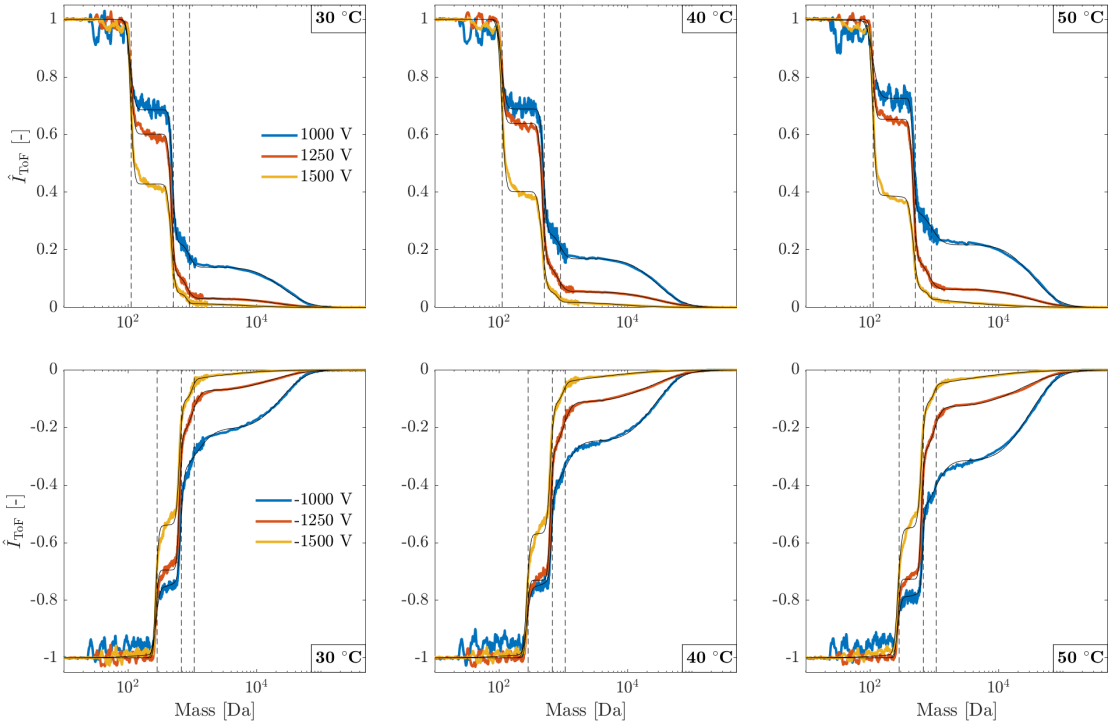

Figure 3.9: Experimental time of flight spectra at 1000, 1250 and 1500 V and constant operating temperature (30, 40 and 50 °C). Positive polarity corresponds to positive applied voltages and negative polarity to negative applied voltages. Fitted curve for each data set is plotted as the black trace.

temperature results in an increase in droplet current. At 1000 V, the droplet current increases from 15 and 20 % at 30 °C to 22 and 32 % at 50 °C. At 1500 V, the droplet current increased from 2 and 6 % to 4 and 8 %. This trend shows that at higher voltages, the droplet population is less sensitive to temperatures changes, while at lower voltages temperature has a greater effect on the droplet contribution. Another finding is that while monomers current percentage increase with higher electric field, increasing the temperature decreases this population in favor of the droplets.

ToF measurements by [117] indicated that at larger values of Q a considerable current fraction was carried by droplets, and as Q reduces, droplet current contribution decreases accordingly. This statement coincides with our hypothesis of higher flow rates with increasing temperature due to the decrease of the hydraulic impedance (lower viscosity). Although ionic emission increases with temperature, flow rate also increases. If the critical flow rate is exceeded, droplet emission occurs, shifting the device to the mixed regime.

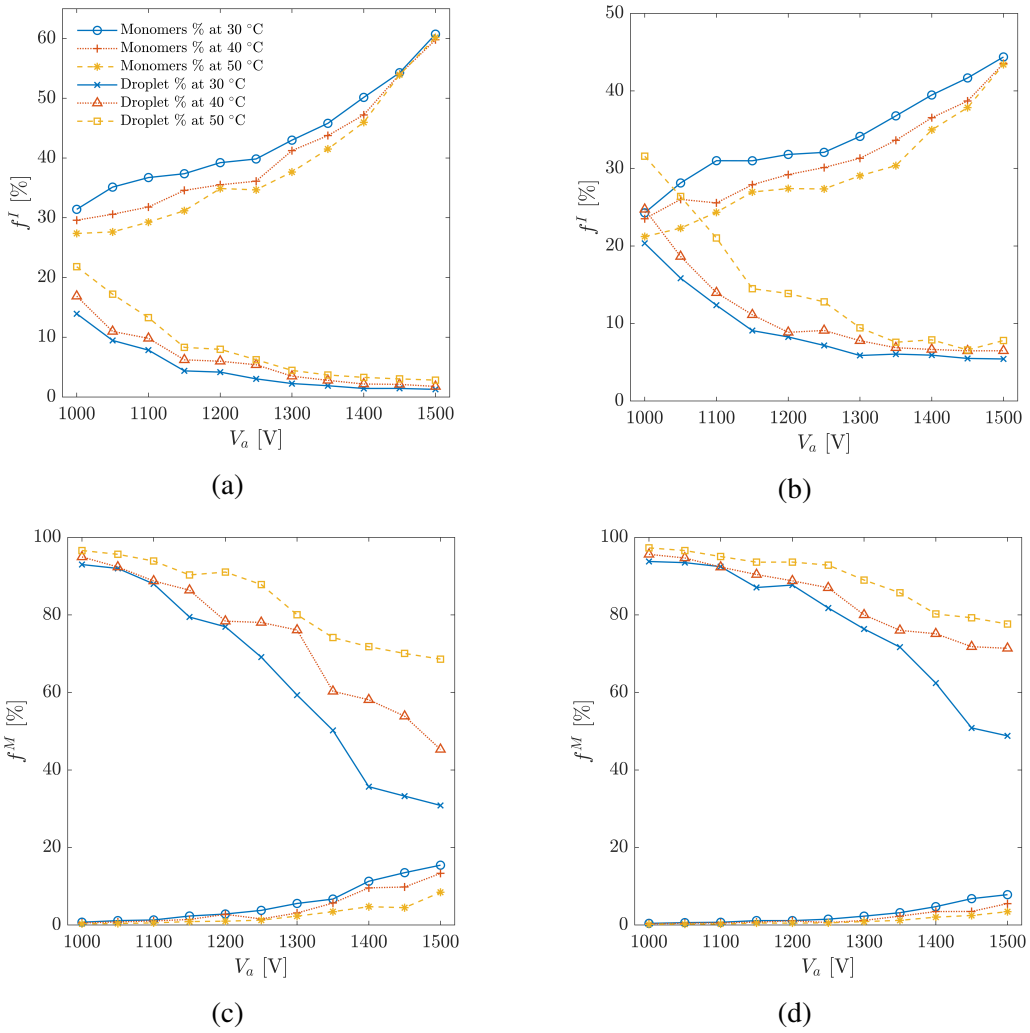

Figure 3.10: a), b) Current fraction of monomers and droplets for positive and negative emission, respectively, and c) , d) mass fraction of monomers and droplets for positive and negative emission, respectively.

3.6 Impact of applied voltage and operating temperature on propulsive performance

By integrating the time of flight curves the thrust and mass flow rate can be obtained. Eq. 3.8 shows the thrust, F_{ToF}, and Eq. 3.9 relates the mass flow, $\dot{m}$ to the flow rate per emitter [65].

$$F_{\text{ToF}} = \frac{2V_a I_e}{L_{\text{ToF}}} \int_0^\infty \hat{I}_{\text{ToF}}(t)dt \tag{3.8}$$

$$Q = \frac{\dot{m}}{\rho N_e} = \frac{4V_a I_e}{\rho N_e L_{\text{ToF}}^2} \int_0^\infty t\hat{I}_{\text{ToF}}(t)dt \tag{3.9}$$

The thrust obtained from the time-of-flight spectra is an overestimation as it is only sensitive to the polydispersive efficiency. To obtain actual thrust the energy efficiency,

the transparency efficiency, and the angular efficiency must be taken into account. The polydispersive efficiency is obtained as [78].

$$\eta_p = \frac{\left(\int_0^\infty \hat{I}_{\mathrm{ToF}}(t)dt\right)^2}{2\int_0^\infty t\hat{I}_{\mathrm{ToF}}(t)dt} = \frac{F_{\mathrm{ToF}}^2}{2\dot{m}I_e V_a} \tag{3.10}$$

The results shown in Fig. 3.11 are the weighted average between positive and negative emission. For the time-of-flight thrust in Fig. 3.11a, the mean is calculated from a time-weighted averaged from the polarity firing times t^+ and t^-. However, the mean specific impulse in Fig. 3.11b is obtained with a mass-weighted average taking into account the mass flows from each polarity. Fig. 3.11c shows the ratio of mean average specific mass to the specific mass of monomers, $\langle m/q\rangle/(m/q)_1$, and Fig. 3.11d the ratio of the mean flow rate per emission site to the critical flow rate, Q/Q^*, as calculated with Eq. 3.4. Note that Q^* varies with temperature as the liquid properties change.

Thrust increases with voltage ($T \propto Q\sqrt{V_a\langle q/m\rangle\eta}$). Even though, at higher voltages Q is reduced, $\langle q/m\rangle$ has increased such that the overall thrust increases. In addition, temperature is observed to have a considerable influence on the thrust. For the same applied voltage, increasing the temperature increases the thrust considerably. At 1500 V, the thrust is increased from 25 to 43 μN when temperature rises from 30 to 50 °C. This effect is explained due to the predominance of droplets when the temperature is increased, as observed by the higher average specific mass, which results in a plume with slower but heavier particles. Since $g_0 I_{\mathrm{sp}} = v \propto \sqrt{V_a}$, ($v$ being the particle velocity) for a monodisperse specific charge one would expect a square root behavior of I_{sp} as a function of the emitter voltage. However, as was derived of the ToF results, the fraction of droplets and ions varies greatly and so does the specific mass and polydispersive efficiency resulting in a very different trend. Due to the predominance of droplets at lower voltages (as well as the lower voltage itself) the specific impulse is about 250 s at 1000 V. As the voltage is increased, the droplet fraction is reduced, and an increase in specific impulse is observed up to 1600 s at 1500 V and 30 °C. As it is expected and contrary to the thrust behavior, increasing the propellant temperature has a negative effect on the specific impulse, due to the higher amount of droplets as well as the increased number of solvated ions in favor of monomers encountered at higher temperatures. Mitigation of these heavy particles in the mixed regime is critical for maximizing specific impulse. The mean flow rate is observed to be above the critical flow rate, explaining why all the cases correspond to the mixed regime. For a given pressure drop, the flow rate is driven by the liquid viscosity. In the case of EMI-Im, an increase in the temperature from 30 to 50 °C results in $\mu_{30°C} = 0.57\mu_{50°C}$, and should yield a flow rate, $Q_{50°C} = 1.75Q_{30°C}$. The differences observed in Fig. 3.11d are greater since as the temperature is increased, not only does the flow rate increase, but the critical flow rate to achieve ionic regime becomes smaller due to the change in the liquid properties, reducing its value 1.95 pL/s to 0.79 pL/s when rising the temperature from 30 to 50 °C.

The polydispersive efficiency is presented as a function of the applied voltage in Fig.

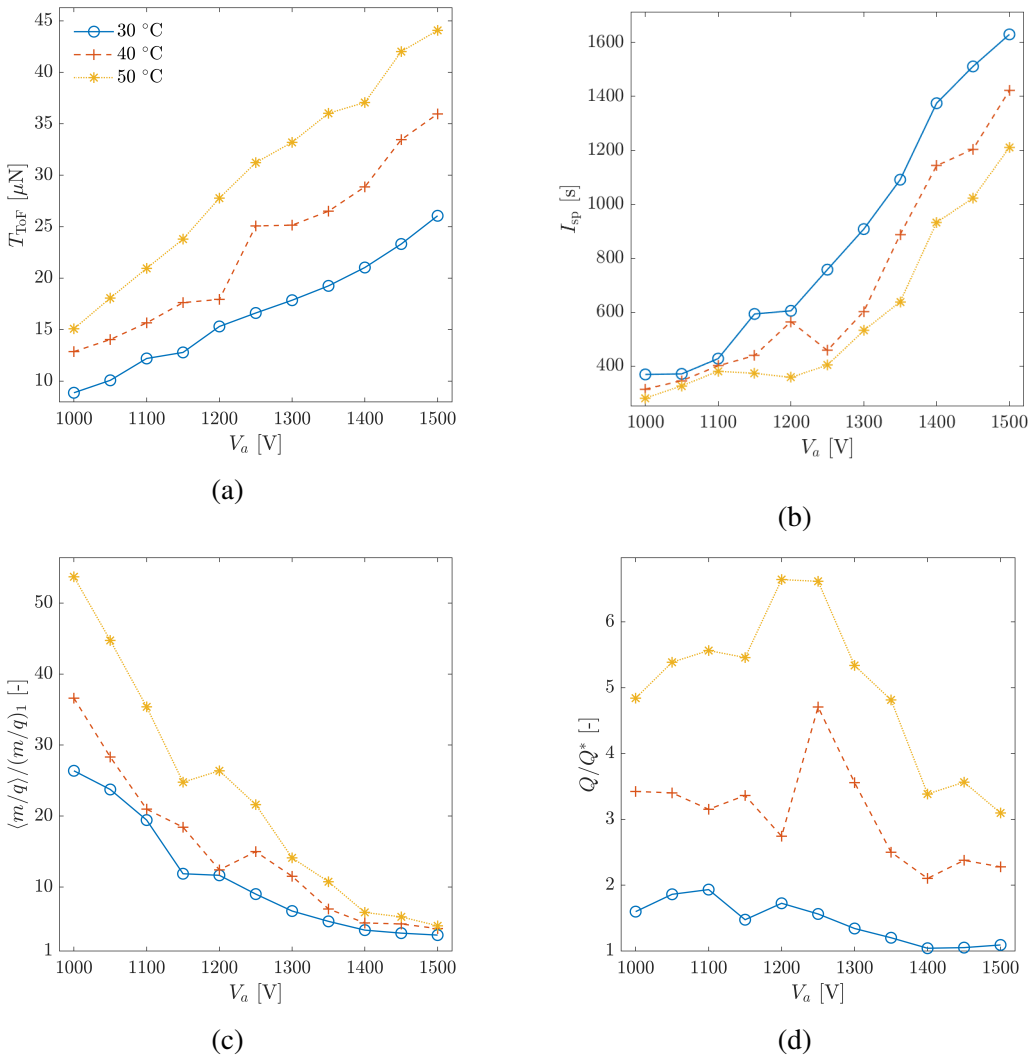

Figure 3.11: a) mean time-of-flight thrust, b) specific impulse, c) normalized mean specific mass with respect to the mean monomer specific mass $(m/q)_1$, and d) normalized mean flow rate with respect to the critical flow rate Q^*, as obtained from the time-of-flight data at different voltages and temperature.

3.12a and as a function of the ion current fraction, f^I_{ion} (including all species except droplets), in Fig. 3.12b. The latter is plotted against a modeled polydispersive efficiency of a plume composed of monomers and droplets. As provided by [118], the efficiency can be expressed as the specific mass weighted average of the polydispersive efficiency of the individual species,

$$\eta'_p = \frac{\left(\sum_{i=1}^{N} f_i^I \sqrt{\langle m/q \rangle_i \eta_{p_i}}\right)^2}{\sum_{i=1}^{N} f_i^I \langle m/q \rangle_i} \qquad \text{with} \quad \eta_{p_i} = \left(\frac{1}{1 + (s_i/c_i)^2}\right)^{1/4} \tag{3.11}$$

where $\langle m/q \rangle_i$ is the average specific mass of each of the species and η_{p_i} is the efficiency of a plume composed of a single specie and it is modeled by a lognormal distribution with

mean c_i and standard deviation s_i. In the case of ions, $\eta_{p_i} = 1$. Because of the dependence of f_{ion}^I with voltage, $\langle m/q \rangle_{\text{drop}}$ is approximated as the mean value for all voltages at 30 °C, s_{drop} and c_{drop} are approximated as the mean value of the fitting parameters from Eq. 3.7 at 30 °C.

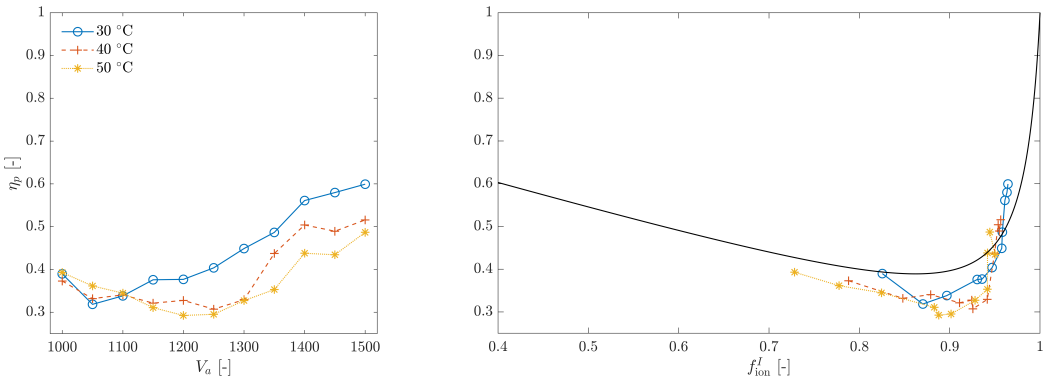

(a) (b)

Figure 3.12: a) Polydispersive efficiency versus applied voltage and b) polydispersive efficiency versus ion current fraction with modeled approximation for the case $T = 30$°C.

When operating in the mixed regime, the polydispersive efficiency is highly dependent on the ratio of ion species to droplets, with a local minimum around $f_{\text{ion}}^I \approx 0.9$. Mitigation of the last percentage of droplets is important to maximize the polydispersive efficiency, as even with ion current fraction of 95 %, the efficiency obtained is 0.6. Deviations of the modeled efficiency with test data are due to disregard of solvated species (dimers and trimers), whose appearance should lower the efficiency [79], as well as the mean values used for the approximation.

3.7 Conclusion

The effect of voltage and propellant temperature on the plume composition and thruster performance has been studied. The characterization was performed for both emission polarities, but for simplicity of results, the mean values are presented when assessing impact on the performance in terms of thrust, specific impulse and polydispersive efficiency. Different voltages were used from 1000 V to 1500 V in steps of 50 V and three temperatures (30, 40, 50 °C). To the best of our knowledge this is the first time that the emission regime of an externally wetted electrospray has been characterized under different propellant temperatures.

Time-of-flight data confirms a mixed regime for EMI-Im. Studies by [55] and [57] using an externally wetted tungsten ribbon have also shown ToF spectra corresponding to a mixed regime with EMI-Im as propellant. Our experimental findings indicate a relative decrease in the droplet population with increasing voltage, as the electric field increases ion evaporation. Negative emission exhibits a greater amount of droplets than the positive

for all cases studied. At higher voltages, droplets are reduced but the pure ionic regime is not completely achieved. The lowest droplet current fraction was achieved at 1500 V and 30 °C in the positive polarity with 5 %, although it accounts for 50 % of the total mass, resulting in a thrust of 26 μN, I_{sp} of 1600 s and polydispersive efficiency of 0.6.

The temperature affects the performance of an externally wetted electrospray, not only in terms of emitted current but also the emission regime. Ionic liquids are sensitive to temperature, and their physical properties can vary considerably. Especially conductivity and viscosity have a strong dependence. This dependence affect both the maximum electric field that can be attained by the liquid and the critical flow rate needed for ionic emission. Moreover, in externally wetted emitters, the viscosity plays a direct role in the flow rate, as it determines the hydraulic impedance.

Measurements at increased temperatures show that ionic emission is enhanced as predicted by the Iribarne-Thomson law. However, droplet emission is also increased. For all applied voltages tested, the droplet current fraction at 50 °C is highest, with a maximum increase of 8 % at 1000 V. Even at 1500 V, droplet current fraction is 1.5 larger at 50 °C than at 30 °. Droplet emission grows faster, leading to a higher relative amount of droplets in the plume. Ion evaporation increases with temperature and the increase of the conductivity with temperature allows for reaching higher electric fields on the meniscus surface. However, contrary to what has been observed in capillary emitter studies, the increase of the temperature shifts the emission regime towards the mixed regime, instead of the pure ionic. In the case of capillary emitters, the flow rate is actively controlled, and if it is below the critical flow rate to achieve ionic regime for the given liquid, the increase of temperature will favor ion evaporation. In externally wetted emitters, the flow rate is passively controlled by the hydraulic impedance of the emitter, a characteristic that depend on geometric parameters (fixed during fabrication) and the fluid viscosity. If the temperature is increased, viscosity decreases, lowering the impedance, resulting in higher flow rates. This effect shifts the emission regime towards the mixed regime for EMI-Im.

* * *

Chapter 4

Characterization of ionic liquids

The content of the current chapter coincides with the following journal paper:

- **D. Villegas-Prados**, J. Cruz, M. Wijnen, P. Fajardo, J. Navarro-Cavallé, "Emission and performance characterization of ionic liquids for an externally wetted electrospray thruster", Acta Astronautica, vol. 219, pp. 97-107, 2024, doi: https://doi.org/10.1016/j.actaastro.2024.03.013 (**Paper II**).

Paper content and author contribution

This study characterizes an externally wetted electrospray thruster using various ionic liquid propellants. Diagnostic tools developed in objectives **O.1.1**, **O.1.2**, and **O.1.3** were employed alongside the vacuum chamber setup (**O.3**) to conduct the research.

The thruster characterization was evaluated across seven ionic liquids (**O.2.3**). Among these, EMI-BF_4 and EMI-Im are well-known and extensively studied in the literature, while the remaining liquids (EMI-DCA, EMI-$EtOSO_3$, EMI-Otf, EMI-SCN, EMI-TFA) have been scarcely reported or never characterized in externally wetted thrusters, addressing the research gap identified as **G.4**. The varying properties of these liquids provide valuable insights into their influence on thruster emission and performance, enhancing the understanding of the mechanisms driving electrospray phenomena in externally wetted thrusters (**G.1**).

The candidate contributed to the development of the vacuum setup, including all diagnostic tools and the thruster assembly, conducted the experiments, and led the post-processing and analysis of the results. This research has been published in Acta Astronautica (**O.4**).

* * *

Abstract

Ionic liquids are the base for electrospray propulsion, yet few have been explored. The performance of an externally wetted electrospray thruster is characterized for seven different ionic liquids: 1-ethyl-3-methylimidazolium tetrafluoroborate (EMI-BF_4), dicyanamide (EMI-DCA), bistrifluoromethylsulfonylimide (EMI-Im), thiocyanate (EMI-SCN), ethylsulphate (EMI-$EtOSO_3$), triflate (EMI-OTf), and trifluoromethanesulfonate (EMI-TFA). This research marks the first time that the latter four liquids are reported for externally wetted emitters. A complete thruster assembly has been tested with each of the propellants. Using time-of-flight mass spectrometry and a Faraday cup for beam divergence, the performance of these ionic liquids has been characterized, assessing thrust, specific impulse and thrust efficiency. EMI-BF_4, EMI-DCA and EMI-SCN operated in pure ionic regime while EMI-Im, EMI-$EtOSO_3$, EMI-OTf and EMI-TFA operated in mixed regime at room temperature (25 °C).

Nomenclature

F	thrust	η_x	transmission efficiency
F_{ToF}	time-of-flight thrust	$\dot{m}_{\text{ToF}}$	time-of-flight mass flow rate
g_0	gravitational constant	K_{ps}	permeability of surface layer
H_c	cone height	P	power
K	liquid conductivity	q/m	charge-to-mass ratio
K_{ps}	permeability of surface layer	R_c	emission region radius
I_e	mean emitted current	R_H	hydraulic impedance
I_{fc}	Faraday cup current	ρ	liquid density
I_{sp}	specific impulse	θ	divergence angle
η_E	energy efficiency	Q	flow rate
η_p	polydispersive efficiency	μ	liquid viscosity
η_T	thrust efficiency	h_s	nano-structure height
η_θ	divergence efficiency	γ	liquid surface tension

Acronyms/Abbreviations

IL	Ionic Liquid
RTIL	Room Temperature Ionic Liquid
PIR	Pure Ionic Regime
EMI-BF_4	1-Ethyl-3-methylimidazolium tetrafluoroborate
EMI-DCA	1-Ethyl-3-methylimidazolium dicyanamide
EMI-$EtOSO_3$	1-Ethyl-3-methylimidazolium ethylsulfonate
EMI-SCN	1-Ethyl-3-methylimidazolium thiocyanate
EMI-TFA	1-Ethyl-3-methylimidazolium trifluoroacetate
EMI-Im	1-Ethyl-3-methylimidazolium bis(trifluoromethylsulfonyl)imide
EMI-OTf	1-Ethyl-3-methylimidazolium triflate
ToF	Time-of-Flight
FC	Faraday Cup

4.1 Introduction

Ionic liquids (ILs) are molten salts formed by stable mixtures of positive and negative molecular ions. Room temperature ionic liquids (RTIL) is the term that has been associated to ILs with a melting point below 100 °C [119]. The first report of low melting salt dates back to 1914 by [120], but it was not until the early 2000s that ILs started to be proposed for electrospray propulsion [121]. Not only does the low melting point aid the storability of these propellants, but they also posses suitable properties for in-space operation such as negligible vapor pressure, high electrical conductivity, K, high surface tension, γ, and low viscosity, μ, [122]. It is the use of these ILs which has allowed electrospray propulsion to emerge as a competitive technology within the field of electric propulsion. The emission of both positive and negative ions eliminates the need for a neutralizer [58]. Also, they are able to retain competitive performance in the low power range, where other electric propulsion technologies suffer from efficiency losses and become less appealing [94]. Along with their compact size and clustering capability, these systems are especially well suited for the micro and nano-satellite market [95].

Electrospray propulsion is based on the extraction and acceleration of charged particles from a conductive liquid, resulting a high velocity jet, thus producing thrust [96]. This is achieved by the application of a strong electric field between the liquid and an extractor grid. In externally wetted emitters, the intensification of the electric field takes place at the tip of cone-like protrusions, called hereafter emission site. The balance between the surface and and electric tension governs the extraction process from the emission site. These type of emitters were first tested with ILs by [68] and have shown emission stability. However they presented drawbacks such as low thrust per emission site (in the order of 0.1 μN [112]). The solution to this problem has been to create an array of emission sites [25], [26].

Another important challenge of externally wetted emitters is the passive control of the flow rate, Q. This is established by the balance of electrical and capillary forces, and a viscous dissipation that induces a pressure drop from the reservoir to the emission site [123]. In electrospraying, controlling Q is essential as only under certain conditions with sufficiently low Q, it is possible to obtain a beam composed of only ionic particles [91], known as the pure ionic regime (PIR). Reaching PIR is interesting for electrospray propulsion as it is characterized by a high specific impulse, high efficiency mode of operation. First studies by [104] supported the notion that PIR is favored by ILs with high electrical conductivity and high surface tension. However, recent work by [123] has shown that in passive sources, electrical conductivity does not affect neither the magnitude of the emitted current nor the flow rate during PIR, but rather they are governed by the viscosity. The fact that for a given IL the product μK is constant [124] has overshadowed the effect of the viscosity in the emitted current. In addition, in externally wetted emitters, for a given electric field, the flow rate is determined by the hydraulic resistance, R_H, which measures the pressure decrease per unit flow rate resulting from fluid friction as the propellant trav-

els from the reservoir to the emission site. The hydraulic resistance is dependent on the liquid viscosity, the geometry of the emitter and the surface roughness. This has been supported experimentally in the works of [108] and [125], and in simulations by [126]. Previous work [72] has also shown that by increasing the liquid temperature results in lower hydraulic resistance, and hence a higher flow rate, producing a higher percentage of droplets and deviating from the pure ionic regime.

It is clear that the properties of the ionic liquid play a significant role in influencing the emission regime and overall performance of an electrospray thruster. Therefore, carefully selecting or designing an ionic liquid propellant is key to obtaining the desired performance. The most commonly used IL is EMI-BF_4. The first test using EMI-BF_4 in externally wetted emitters was performed by [68] demonstrating pure ionic emission from a tungsten needle. Later, [25] characterized the current emission from a microfabricated array of needles. There are several reported results on EMI-BF_4 using externally wetted emitters with all of them performing in the pure ionic or near-pure ionic regime at room temperature [32], [68], [127]. Another common liquid in electrospray is EMI-Im. This liquid has a lower conductivity than EMI-BF_4, but it is much less hygroscopic which improves its use in vacuum [113]. EMI-Im has been extensively tested with capillary emitters showing a great amount of droplets [107]. With externally wetted emitters, [70] reported PIR, in contrast to other authors where mixed regime has been observed [55], [57]. Another liquid that has been successfully tested with externally wetted emitters is EMI-DCA [128], showing a mixed regime close to PIR. Along EMI-SCN, these ILs are of great interest, as they are hypergolic, and are being studied as propellants for chemical propulsion for a possible dual-mode propulsion thruster [129]–[133].

During this work a total of seven liquids are studied. Three of the seven ILs tested are the widely known throughout the literature and already mentioned EMI-BF_4, EMI-Im and EMI-DCA. These will serve as baseline comparison. The remaining four ILs, to the best of our knowledge, have never been characterized for externally wetted emitters: EMI-SCN [134] and EMI-OTf [135] have been tested in single capillary emitters. EMI-TFA, and EMI-$EtOSO_3$ have not been reported for any emitter topology. Tab. 4.1 summarizes the propellants used along with the emission regime in which they have been reported for an externally wetted configuration.

The purpose of this work is to successfully characterized the performance of externally wetted emitters with new ionic liquids that could be suitable for electrospray propulsion. The performance of the thruster will be assessed for different operating voltages at room temperature for each of the propellants proposed. A time-of-flight mass spectrometer technique, specifically adapted to the characteristics of the thruster, was used to derived the performance, and a Faraday cup was used to estimate the beam divergence. The rest of the article is organized as follows: Sec. 4.2 presents the thruster, the ionic liquids and the experimental set-up, Sec. 4.3 discusses the obtained results and Sec. 4.4 summarizes the conclusions extracted.

Anion chemical name	Abbreviation	Regime
tetrafluoroborate	EMI-BF_4	Ionic[68], Mixed[127]
bis-trifluoromethylsulfonyl-imide	EMI-Im	Ionic[58], Mixed[55]
dicyanamide	EMI-DCA	Mixed [128]
thiocyanate	EMI-SCN	Mixed*[134]
triflate	EMI-OTf	-
trifluoromethanesulfonate	EMI-TFA	-
ethylsulphate	EMI-$EtOSO_3$	-

* Only reported data of EMI-SCN regime, but with capillary emitter.

Table 4.1: Chemical name of ionic liquids tested and emission regime reported in the literature for externally wetted emitters. Common cation specie 1-ethyl-3-methylimidazolium (EMI^+) is omitted.

4.2 Experimental methods

4.2.1 Thruster description

The electrospray thrusters used in this study [72], [136] consist of an borosilicate-based extractor grid and an oxidized, silicon-based externally wetted emitter array, featuring 101 micro cones with nano-texturization to control the hydraulic resistance and a propellant reservoir for liquid storage. In addition, the emitter includes multiple feeding holes that allow the ionic liquid to flow passively from the reservoir positioned beneath the emitter to the emission sites. To ensure an uninterrupted liquid connection between the emitter and reservoir, a porous textile material is inserted. The reservoir itself is constructed using 3D printing technology, employing a porous aluminum piece. A schematic of a single micro-cone is shown in Fig. 4.1.

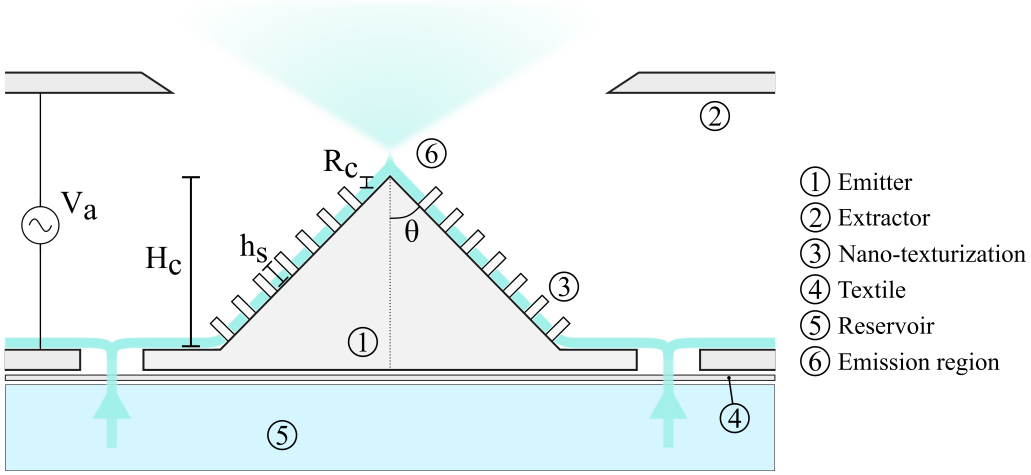

Figure 4.1: Schematic of externally wetted emitted with nano-texturization for impedance control (not to scale), featuring emitter, extractor grid and reservoir.

As mentioned, one of the challenges of externally wetted emitters is the flow rate control. It is passively controlled through the hydraulic resistance which depends on the viscosity of the liquid and geometric parameters of the emitter [26]. The hydraulic resistance of a conical externally wetted emitter is estimated as,

$$R_H = \frac{\mu}{2\pi K_{\text{ps}} h_s \sin\theta} \ln\left(\frac{H_c}{R_c}\right) \tag{4.1}$$

where θ is the cone semiangle, R_c is the base of emission region ($10^0 - 10^{-1}$ μm [102]), H_c the height of the emitter, h_s the height of the nano-structures composing the nano-texturization and, K_{ps} is the permeability of the surface layer, which is calculated according to the model of [137]. The geometric contribution to the hydraulic impedance for our emitters is, $R_H/\mu = 85 \cdot 10^{17}$ m^{-3}. From this equation, it is clear that for a fixed emitter geometry (K_{ps}, θ, R_c, and H_c, h_s), the flow rate is driven by the viscosity of the liquid. If the viscosity decreases, the hydraulic resistance decreases, hence increasing the flow rate.

For every propellant a different emitter was used to avoid cross-contamination. All the emitters used for this study were from the same silicon wafer to minimize possible differences between fabrication batches. Each emitter within the wafer was characterized using a scanning electron microscope to ensure that all the parameters of the emitter are similar. In addition, a different reservoir was used for every liquid to avoid contamination between cleaning procedures. All the reservoirs were filled with the same amount of propellant, 45 μL. The propellant handling and assembly process was carried using identical procedures to minimize any uncertainty that may arise from the thrusters operation.

4.2.2 Ionic liquid properties

The selected ILs all have the same cation (EMI^+), but a different anion, with a wide range of different properties to extract as many conclusions as possible from the performance of the liquids. According to studies [138], [139], generally a low molecular weight enhances the ion transport mechanism, which often results in ILs with higher conductivity. Propellants with lower molecular weight often exhibit lower densities. From an operational standpoint, higher density is typically desirable as it allows to store a larger amount of propellant within the given propellant tank volume, increasing the total impulse available. Tab. 4.2 shows the physical properties of the ILs studied along with the estimated hydraulic resistance for the given emitter and each IL, as calculated from Eq. 4.1. Since the thrusters have identical geometry, those liquids with highest viscosity will have the highest hydraulic resistance.

4.2.3 Vacuum facility and diagnostics

The vacuum facility used to conduct the experiments is similar to the one described in [72], a time-of-flight mass spectrometry (ToF) with the addition of a Faraday cup (FC) to

Ionic liquid	Anion [Da]	γ [mN/m]	K [S/m]	μ [mPa·s]	ρ [g/cm^3]	$R_H \cdot 10^{17}$ [Pa·s/m^3]
EMI-BF_4	87	52	1.4	44	1.29	3.74
EMI-Im	282	36	0.9	34	1.52	2.89
EMI-DCA	66	61	1.7	15	1.10	1.27
EMI-SCN	58	49	1.8	23	1.12	2.38
EMI-OTf	150	40	0.9	40	1.39	3.40
EMI-TFA	114	-	1.0	29	1.31	2.47
EMI-$EtOSO_3$	127	47	0.4	98	1.24	8.33

Table 4.2: Anion mass, surface tension (γ), conductivity (K), viscosity (μ), density (ρ) and estimated hydraulic impedance (R_H) for all the ionic liquids at room temperature (25 °C). Data has been obtained directly from the manufacturer of the ionic liquid. In the case that a parameter was not specified, literature references were used [140]–[145]. Molecular mass of cation (EMI^+) is 112 Da.

allow for angular divergence measurements. The thruster is mounted on a rotary stage, so that ToF and FC measurements can be taken uninterruptedly. Chamber pressure was maintained below 10^{-5} mbar during thruster operation.

4.2.4 Thruster operation

For each propellant the thruster was operated a different applied voltages, V_a, from 1000 V to 1600 V in 100 V intervals. ToF and FC measurements were taken at each voltage. The voltage waveform applied to the thruster is a trapezoid with amplitude V_a and an a period of approximately 1 s. A trapezoidal wave is preferred respect to a square one to avoid large dV/dt which create unwanted transients in the voltage signal. While the applied voltage is symmetric ($\pm V_a$) the resulting current is not. To avoid charging of the propellant the duration of the positive half cycle is fixed but the duration of the negative half cycle is varied in real time such that the total charge emitted in each half-cycle is equal (but opposite). The operating temperature was 25 °C during all the tests. As depicted in Fig. 4.3, samples extracted from the operation of both EMI-BF_4 and EMI-$EtOSO_3$ at the maximum voltage of 1600 V illustrate noteworthy distinctions. In particular, the positive current exhibited a higher magnitude, necessitating a longer duration of emission in the negative polarity to achieve the required balance.

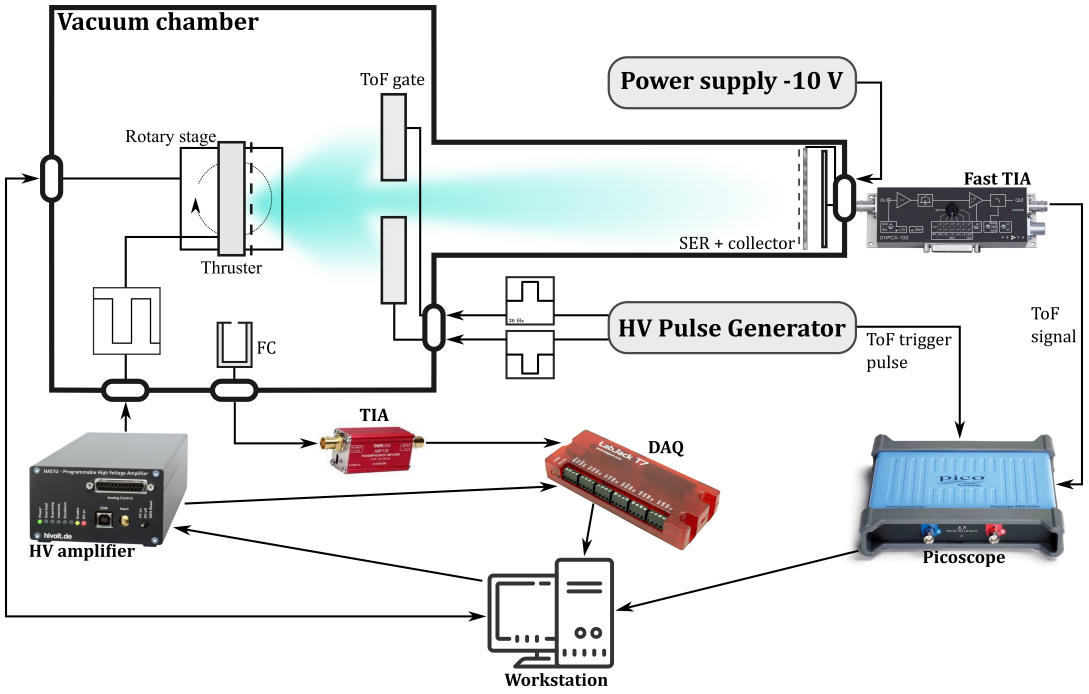

Figure 4.2: Experimental set-up including vacuum chamber, electrospray source, indirect diagnostics (time-of-flight and Faraday cup), and instruments. The thruster is mounted on the rotary stage controlled by the workstation. The time-of-flight comprises the electrostatic gate pulsed by the high-voltage pulse generator, the secondary electron repeller supplied with -10 V, and a collector connected to a fast transimpedance amplifier. Time-of-flight data is collected by a oscilloscope. The Faraday cup includes a trans-impedance amplifier and a data acquisition system. The thruster is operated using its own high-voltage amplifier.

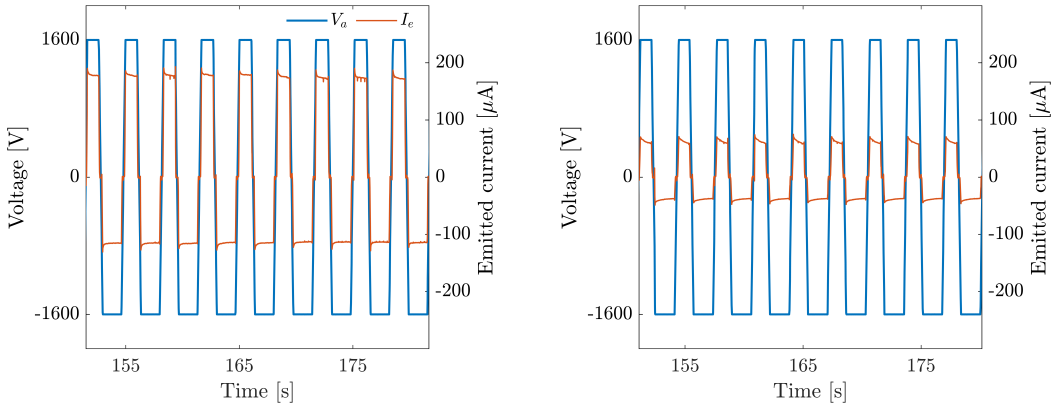

Figure 4.3: Sample of applied voltage (V_a) and emitted current (I_e) versus time for: EMI-BF_4 (a), and EMI-$EtOSO_3$ (b). The trapezoidal voltage waveform is observed. Additionally, the variations in the duration of positive and negative cycles are observed, attributed to the disparate magnitudes of the emitted current.

4.3 Results

4.3.1 Current-voltage characterization

Fig. 4.4 shows the mean emitted current, I_e, across the spectrum of ILs at varying applied voltages during their operation. The error bands correspond to the standard deviation of the mean emitted current during the thruster operational timespan at the specified voltage. From these results, EMI-SCN shows the highest emitted current with an average (between positive and negative emission) of 230 μA at 1600 V, followed by EMI-DCA and EMI-BF_4 with 184 and 146 μA respectively, while EMI-$EtOSO_3$ presents the lowest with a modest 50 μA. Moreover, the effect of surface tension on the thruster's startup voltage is discernible at the 1000 V operational threshold, where EMI-DCA (γ = 61 mN/m), and EMI-BF_4 (γ = 52 mN/m), both exhibit relatively low emitted currents at this specific voltage, measuring 6 μA and 17 μA, respectively, when compared to the other ILs, despite the fact that they emit more across the rest of applied voltages. In accordance with [146], which emphasize the correlation between surface tension and the initiation voltage for electrospraying from needles, it is evident that the elevated surface tension values of these ILs lead to an increase in the startup voltage. Consequently, this results in a diminished emission at the 1000 V benchmark, when contrasted with the remaining ILs with lower surface tension.

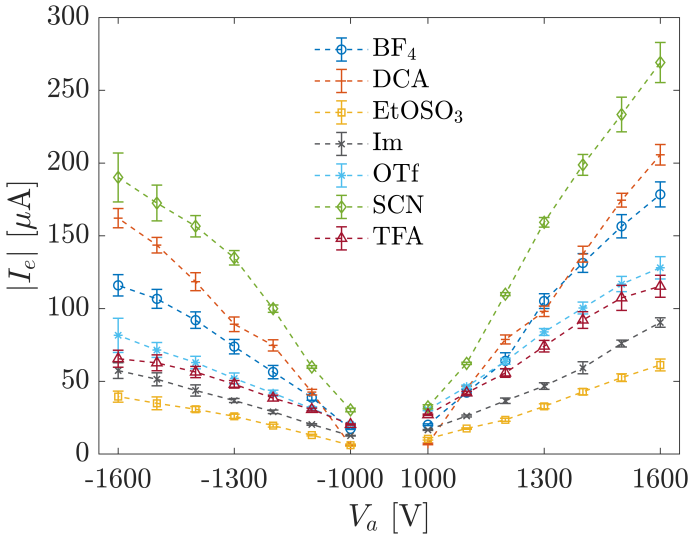

Figure 4.4: Emitted currents as a function of voltage for positive and negative polarities for all the ionic liquids tested

A quick glance at Tab. 4.2 and Fig. 4.4 shows that the liquids with the highest emission correspond to the higher conductivity ones. In order to verify this assumption, the emitted current is plotted against K for voltages above 1200V V in Fig. 4.5. Voltages below were not considered as the higher γ ILs are closer to the startup voltage. These values correspond to the initial exponential part of the I-V curve. A fitting curve is shown as a

black trace for each V_a. For the fitting, it was assumed that $I_e \propto K^m$. The results indicate that the emitted current exhibits a quadratic relationship with the electrical conductivity of the liquid. The same procedure was applied to the viscosity, but the data was more scattered, showing no clear relationship. These findings highlight that, based on experimental data, liquid conductivity appears to strongly correlate with the emitted current. However, it is important to note that correlation does not imply causation; the tested liquids possess various properties that could collectively influence the emission behavior.

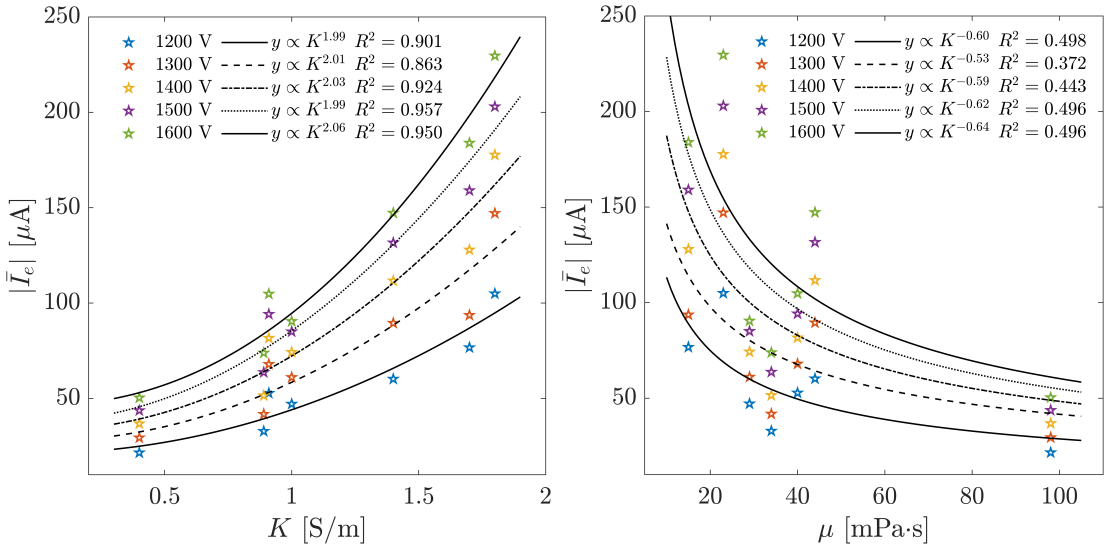

Figure 4.5: The mean emitted current (time-averaged between positive and negative cycles) is presented as a function of conductivity (left) and viscosity (right) at various applied voltages: V_a = 1200, 1300, 1400, 1500, and 1600 V. Black traces represent power fits for each applied voltage, emphasizing the dependence of emitted current on conductivity, along with the visual dispersion concerning viscosity.

4.3.2 Beam divergence

Assessing the beam divergence holds significance not only from a propulsion standpoint but also from an operational perspective, as accumulation of liquid on the extractor grid is one of the primary failure modes in electrospray systems is the accumulation of liquid on the extractor grid [147]. The main mechanism is direct overspray from the emission site, where the plume expansion hits the extractor. Other factors can be the radial expansion of the plume due to space charge repulsion and fragmentation of emitted charged species [78], [148]. In this regard, the difference in mass-to-charge, m/q, of the emitted particles results in the droplets barely moving while ions get repelled.

To evaluate the angular divergence of each ionic liquid, a FC scan was conducted over an angular range spanning from -90 to 90 ° relative to the central thruster axis, at the previously mentioned applied voltages. As illustrated in Fig. 4.6, the scan results depict the angular distribution of the seven liquids during positive emission at 1000, 1300, and 1600

V. To perform angular scans, the thruster was operated for several cycles at each angle position before moving to the next. The reported values represent the mean normalized collected current, and the associated error bands depict the standard deviation of these mean values. It is important to note that the error bands are selectively provided for a subset of values across the angular distribution to offer an estimation of their magnitude.

The findings of our study reveal a clear correlation between increased voltage and the widening of the beam. This effect is particularly pronounced for EMI-DCA and EMI-$EtOSO_3$, both of which exhibit the narrowest maximum opening angles at 1000 V, measuring -26°/38° and -40°/38°, respectively. In contrast, EMI-BF_4, EMI-SCN, and EMI-TFA maintain consistent maximum opening angles (angle at which no current is collected by the FC) of approximately 50° across all voltage levels, but the angular distribution becomes broader as the applied voltage increases. Conversely, EMI-Im and EMI-OTf display characteristic changes in their distribution patterns. For EMI-Im, at 1600 V, a distinctive shift of 5° to the right is observed in the central thrust angle, suggesting that individual beamlets from each emission site may be emitting off-axis. A similar trend is observed for EMI-OTf, where the distribution progressively widens, yielding maximum opening angles of -66°/64°. This effect becomes more pronounced with higher applied voltages.

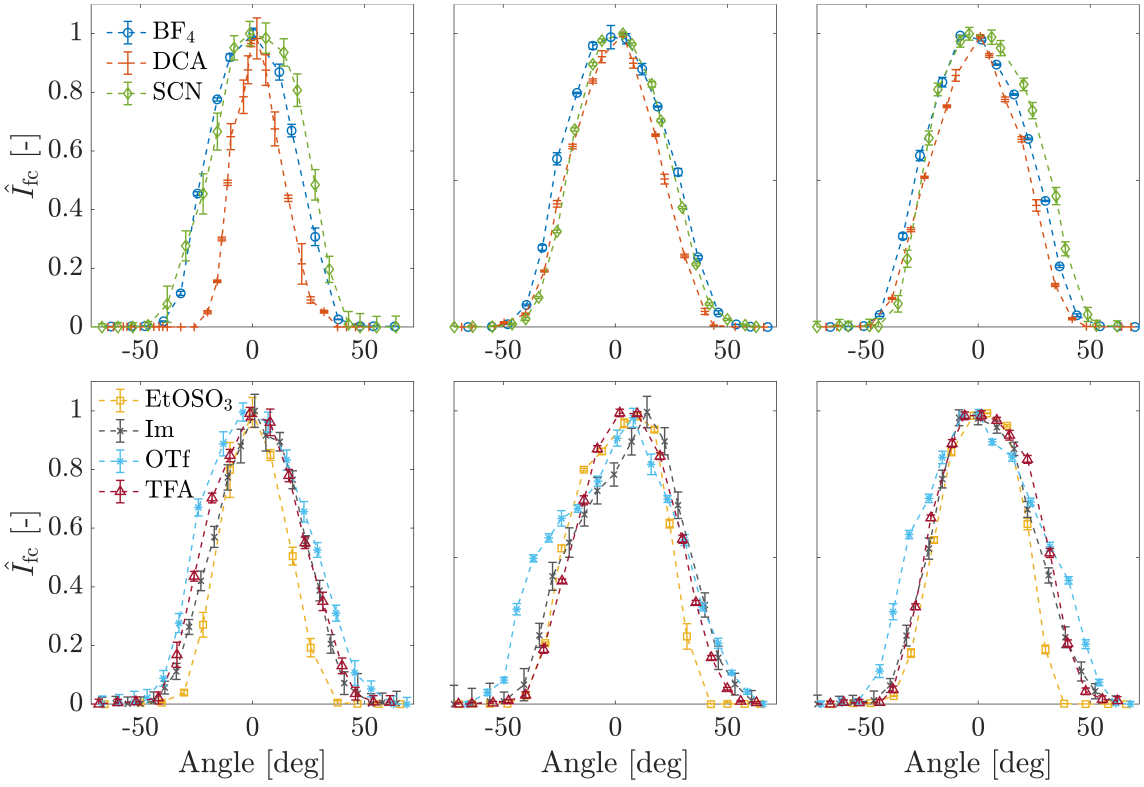

Figure 4.6: Angular current distribution in the positive polarity for EMI-BF_4, EMI-DCA, and EMI-SCN (top); and EMI-$EtOSO_3$, EMI-Im, EMI-OTf, and EMI-TFA (bottom) for 1000 V (left), 1300 V (middle), and 1600 V (right).

The associated angular efficiency for these profiles is determined using Eq. 4.2 [65],

where the plume is considered symmetric and half-averaged. This parameter is a charge weighted average of the cosine of the angle of the velocity vector, consequently contributing to the overall thrust generation.

$$\eta_\theta = \left(\frac{\int_0^{\frac{\pi}{2}} \hat{I}_{\mathrm{fc}}(\theta) \cos\theta \sin\theta d\theta}{\int_0^{\frac{\pi}{2}} \hat{I}_{\mathrm{fc}}(\theta) \sin\theta d\theta} \right)^2 \tag{4.2}$$

where θ is the angle respect to the central axis of the thruster and $\hat{I}_{\mathrm{fc}}$ the normalized angular distribution. Fig. 4.7 shows the angular efficiency for positive and negative emission respect to the emitted current. The emitted current, although being dependent on V_a, is used for better visualization of the plots The angular efficiency exhibits an interesting trend, with its highest values observed at lower emitted currents, and diminishing as the applied electric field intensifies. EMI-DCA, in particular, achieves the highest angular efficiency at ± 7 μA (1000 V), registering values of $\eta_\theta^+ = 0.939 \pm 0.006$ and $\eta_\theta^- = 0.958 \pm 0.007$. When increasing the applied voltages, these values are reduced, $\eta_\theta^+ = 0.849 \pm 0.010$ and $\eta_\theta^- = 0.857 \pm 0.009$ at 1600 V. This decrease is clearly evident when examining the angular distribution curves for EMI-DCA in Fig. 4.6, wherein both the full width at half maximum and the maximum opening angle increase with voltage. In contrast, EMI-SCN and EMI-TFA exhibit the lowest variation in angular efficiency with changing current, maintaining an average of $\langle \eta_\theta \rangle = 0.856 \pm 0.015$ and $\langle \eta_\theta \rangle = 0.836 \pm 0.012$, respectively, with only a 1% variation observed over the entire operational range. EMI-$EtOSO_3$, while covering a shorter range, demonstrates notably high angular efficiency compared to other heavier liquids. Conversely, EMI-OTf displays the poorest divergence efficiency, with $\eta_\theta^+ = 0.744 \pm 0.017$. This divergence can be attributed to off-axis emission and the asymmetric shape of its plume. Additionally, it is worth noting that the divergence stabilizes for EMI-DCA, EMI-TFA, EMI-BF_4, and EMI-SCN after reaching a certain emission current. On a broader note, it can be deduced that, across all liquids and operational points, negative emission consistently yields superior angular efficiency compared to positive emission. It is attributed to the generally lower current emission in the negative polarity, lowering the repulsion forces in the plume, hence yielding a higher η_θ. Recent studies by [136] demonstrate that the shape and geometry of the emitter play a critical role in determining the beam divergence profile. These findings suggest that minor imperfections in the emitter may have a more significant impact on beam divergence than variations in the applied voltage.

4.3.3 Time-of-flight spectra

To generate these ToF curves, the flight times recorded during the measurements are converted into ion masses, with the assumption that all particles possess a charge of e. Each curve displayed represents the average of 800 ToF measurements, a measure taken to minimize noise and uncertainty. A fitting approach, involving the superposition of lognormal distributions [72], [118], is shown as the red trace. This method is employed to mitigate

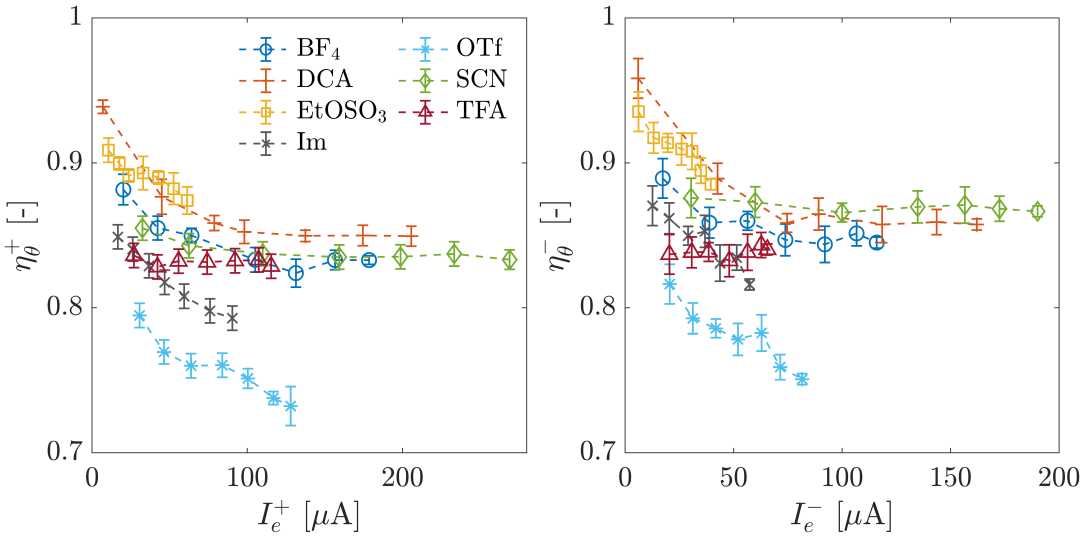

(a) Positive angular efficiency.

(b) Negative angular efficiency.

Figure 4.7: Positive (a) and negative (b) angular efficiency versus emitted current. It is plotted against the emitted current for a better visualization of the plot, where each point corresponds to the subsequent applied voltage.

the impact of noise in the recorded data, which can significantly affect the results, especially when the measured signal approaches zero, [39], [149]. In Fig. 4.9, ToF curves for the seven liquids are presented at both 1000 V and 1600 V. Each liquid's ToF data comprises four curves: the upper ones depict results during positive emission for both voltages, while the lower ones represent negative emission. Tab. 4.3 shows the current fraction of the different populations at the two shown voltages.

The selection of 1000 V and 1600 V as the two voltages for analysis was deliberate, aiming to visually discern differences in the operation regime. Higher voltages notably enhance ion evaporation, resulting in not only higher emitted currents but also a larger fraction of ions relative to droplets. Across all the liquids, it is apparent that the fraction of droplets is significantly reduced with increased voltage. At 1000 V, all the liquids operate in a mixed regime, with EMI-TFA displaying the highest droplet current fraction, measuring 13% and 26% for positive and negative emission, respectively. At 1600 V, EMI-BF_4, EMI-DCA, and EMI-SCN appear to operate in a pure ionic regime. Other liquids, such as EMI-$EtOSO_3$, EMI-Im, EMI-OTf, and EMI-TFA, still remain in the mixed regime at 1600 V, with the negative emission exhibiting a slightly higher droplet current fraction compared to the positive. In the case of EMI-BF_4, EMI-DCA, and EMI-SCN, increasing the voltage leads to an increase in the monomer current fraction while reducing dimers, trimers, and the droplet fraction. These three liquids hold an advantage in PIR, not only due to their high conductivity but also their higher surface tension, which favors this regime [104]. However, when comparing these liquids, it's crucial to consider the overall performance. At 1600 V, although EMI-SCN has below 1% of droplets in both polarities, they constitute 48% and 39% of the plume mass, as opposed to 18%-12%

Ionic liquid	V_a [V]	positive emission				negative emission			
		$n = 0$	$n = 1$	$n = 2$	n_{drop}	$n = 0$	$n = 1$	$n = 2$	n_{drop}
BF_4	1000	0.24	0.59	0.10	0.07	0.27	0.57	0.10	0.06
	1600	0.55	0.35	0.09	0.01	0.58	0.35	0.06	0.01
DCA	1000	0.41	0.49	0.02	0.08	0.60	0.34	0.03	0.03
	1600	0.71	0.25	0.03	0.01	0.85	0.12	0.03	<1%
$EtOSO_3$	1000	0.14	0.41	0.33	0.12	0.20	0.36	0.22	0.22
	1600	0.31	0.51	0.15	0.03	0.37	0.46	0.12	0.05
Im	1000	0.38	0.47	0.08	0.07	0.33	0.35	0.20	0.12
	1600	0.55	0.37	0.05	0.03	00.48	0.38	0.06	0.11
OTf	1000	0.24	0.56	0.14	0.06	0.13	0.35	00.48	0.10
	1600	0.34	0.49	0.13	0.04	0.26	0.41	0.27	0.06
SCN	1000	0.57	0.37	0.02	0.04	0.72	0.26	0.01	0.01
	1600	0.82	0.17	0.01	<1%	0.89	0.11	0.00	<1%
TFA	1000	0.18	0.58	0.11	0.13	0.04	0.26	0.44	0.26
	1600	0.40	0.48	0.09	0.03	0.19	0.48	0.25	0.08

Table 4.3: Current fraction of monomers (degree of solvation $n = 0$), dimers ($n = 1$), and trimers ($n = 2$), and droplet current fraction (n_{drop}) for positive and negative emission of the tested ionic liquids at two applied voltages: 1000 and 1600 V.

and 36%-18% for EMI-BF_4 and EMI-DCA, respectively. This is because the droplets in EMI-SCN, though fewer in number, are heavier and can potentially impact performance more than the other two liquids. Therefore, from this information, it can be inferred that EMI-BF_4 may exhibit the best performance among the three. It is worth noting that the higher viscosity of EMI-BF_4, compared to the other two ILs, contributes to the reduction in droplets as it restricts the flow rate, as indicated by Eq. 4.1. In contrast, EMI-$EtOSO_3$, EMI-Im, EMI-OTf, and EMI-TFA exhibit a higher proportion of droplets. In the negative polarity, these liquids display an increase in both the fraction of monomers and dimers, while the trimers and droplet fraction decrease. Due to their lower γ and K, these four liquids are anticipated to deliver comparatively inferior performance. Furthermore, their higher molecular mass results in a lower specific impulse. Among these four, EMI-$EtOSO_3$ distinguishes itself from the rest. Its elevated μ imposes sufficient restrictions on the flow to maintain a droplet mass fraction of just 35%-31%. This fraction is even lower than that of EMI-SCN, underscoring the critical importance of a high-impedance system for externally wetted emitters when aiming for an ionic regime.

a) EMI-BF_4 b) EMI-DCA

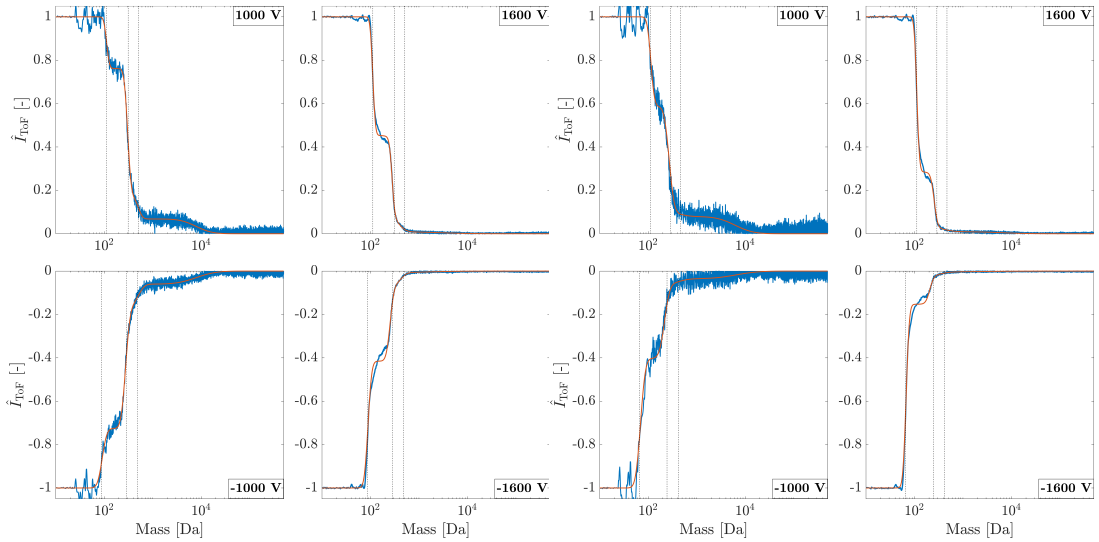

c) EMI-$EtOSO_3$ d) EMI-Im

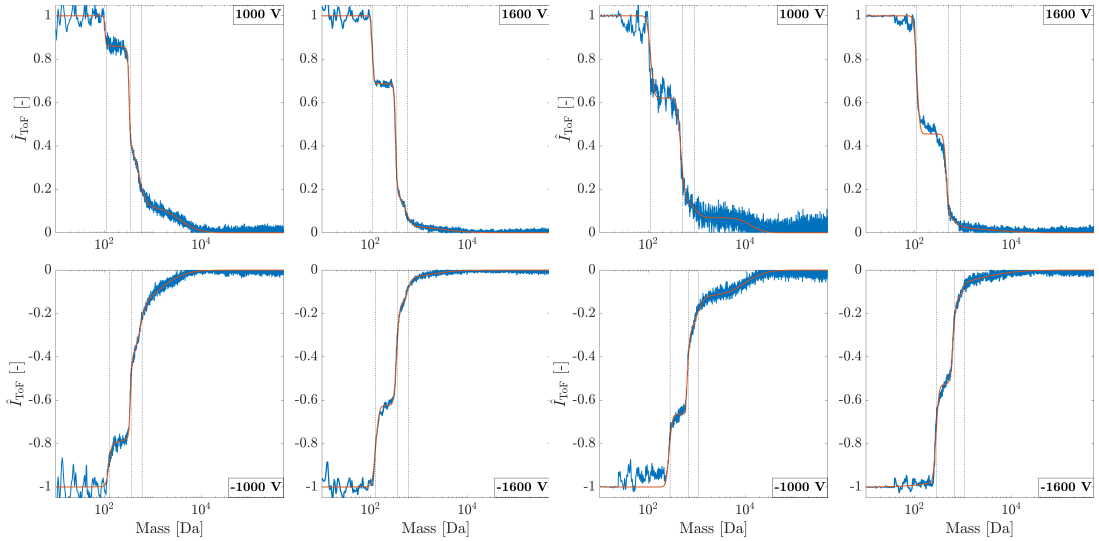

e) EMI-OTf f) EMI-SCN

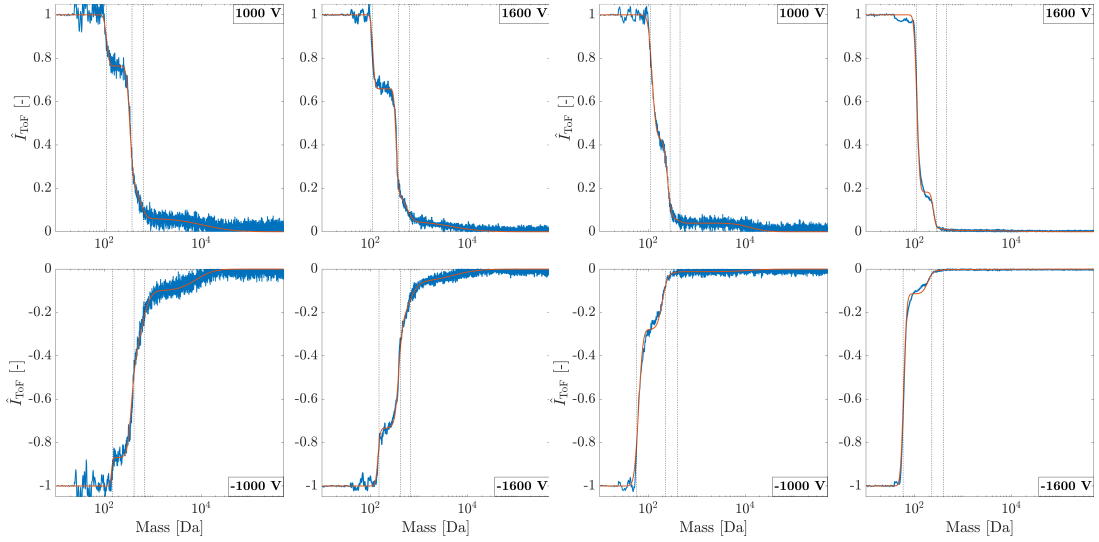

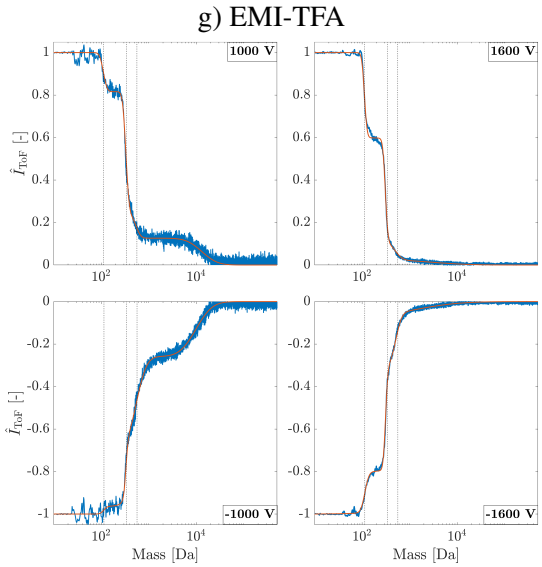

Figure 4.9: Experimental time of flight spectra for a) EMI-BF_4, b) EMI-DCA, c) EMI-$EtOSO_3$, d) EMI-Im, e) EMI-OTf, f) EMI-SCN, and g) EMI-TFA for positive and negative emission and two operating voltage 1000 and 1600 V. Dashed lines correspond to the theoretical mass of the oligomers with degree of solvation $n = 0$ for monomers, $n = 1$ for dimers, and $n = 2$ for trimers. Note that for some of them, trimers are not present at all. Raw data is presented in blue and a fit using log-normal distributions is plotted as the red trace.

4.3.4 Propulsive performance

The thruster performance can be estimated by integrating the ToF curves. Eq. 4.3 gives the thrust, F, and Eq. 4.4 the specific impulse [65],

$$F = \eta_x \eta_E \sqrt{\eta_\theta} F_{\mathrm{ToF}} = 2\eta_x \eta_E \sqrt{\eta_\theta} \frac{V_a I_e}{L_{\mathrm{ToF}}} \int_0^\infty \hat{I}_{\mathrm{ToF}}(t) dt \tag{4.3}$$

$$I_{\mathrm{sp}} = \frac{F}{g_0 \eta_E} \dot{m}_{\mathrm{ToF}}^{-1} = \frac{\eta_x \sqrt{\eta_\theta} L_{\mathrm{ToF}}}{2 g_0} \left[\int_0^\infty t \hat{I}_{\mathrm{ToF}}(t) dt \right]^{-1} \tag{4.4}$$

where $\hat{I}_{\mathrm{ToF}}$ is the normalized ToF curve and L_{ToF} the flight length. The energy efficiency, η_E, and the transmission efficiency. η_x, are also introduced. The energy efficiency is an measure of the acceleration of the particles respect to the applied potential and previous measurements have confirmed that regardless of propellant and voltage, η_E remains close to unity, approximately 0.97. The transmission efficiency accounts for the current that impacts the extractor and has been consistently measured as $\eta_x > 0.99$. The thrust efficiency, η_T, can be calculated using all the efficiencies,

$$\eta_T = \eta_\theta \eta_E \eta_p \eta_x^2 \tag{4.5}$$

where $\eta_p = F_{\mathrm{ToF}}^2 / (2\dot{m}_{\mathrm{ToF}} I_e V_a)$ and constitutes the polidispersive efficiency. This parameter quantifies the presence of different species in the plume and how they are non-uniformly

accelerated due to varying m/q ratios. Generally, it is the factor that most significantly impacts overall thrust efficiency. In a scenario with only one type of particle, η_p would equal 1. Fig. 4.10 shows the thrust versus the emitted current and Fig. 4.11 shows the specific impulse and polydispersive efficiency respect to the applied voltages for all the propellants. Mean values are calculated by time-averaging between positive and negative emissions for thrust and mass-averaging for specific impulse and polydispersive efficiency. Fig. 4.12 presents the propulsive performance map for all the liquids, including the thruster efficiency lines based on the thrust to power ratio (F/P) and I_{sp}, $\eta_T = (F/P)g_0 I_{sp}/2$ [127]. The performance plots incorporate error bands representing the potential deviation of the mean values resulting from propagating uncertainties estimated through the calculations of Eq. 4.3, 4.4, and 4.5. The primary source of uncertainty in these equations is associated with the emitted current as observed in the uncertainty in Fig. 4.4. Given that ToF data collection spans a few minutes to capture all samples, variations in current may occur during this timeframe, and these variations are duly considered in the error bands. Note that the uncertainty calculated in the beam divergence analysis is also incorporated into the performance uncertainty calculations through the angular efficiency.

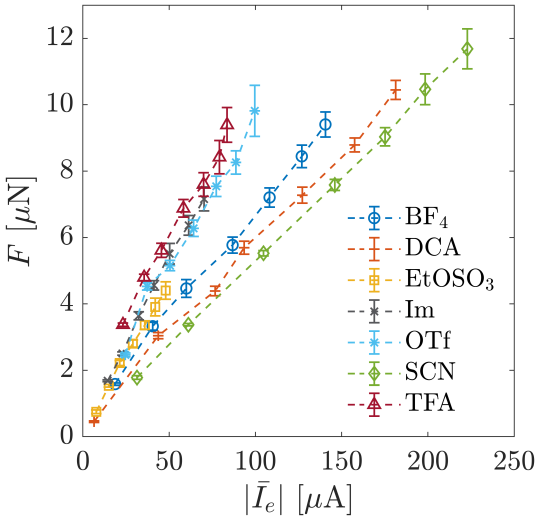

Figure 4.10: Mean thrust, F versus emitted current, I_e, for all the ionic liquids. Thrust is presented versus current to highlight the linear relationship between these two.

The thrust exhibits a linear increase with the current. Among the tested ionic liquids, EMI-SCN delivers the highest thrust at 11.7 ± 0.6 μN, while EMI-EtOSO$_3$ provides the lowest thrust at 4.4 ± 0.3 μN. This disparity can primarily be attributed to the fact that the emitted current for EMI-SCN surpasses that of the other liquids. However, when considering a fixed current, the highest thrust is achieved by EMI-TFA, followed by EMI-Im and EMI-OTf. These liquids, being heavier and featuring the presence of droplets in the plume, result in a higher mass-to charge, m/q, thus yielding greater thrust per μA of emission. For instance, at an emission of 70 μA, EMI-TFA delivers 8.6 μN, a considerable increase compared to EMI-BF$_4$ at 4.9 μN, EMI-DCA at 4.1 μN, and EMI-SCN at 3.8 μN (assuming the linearity of thrust with current).

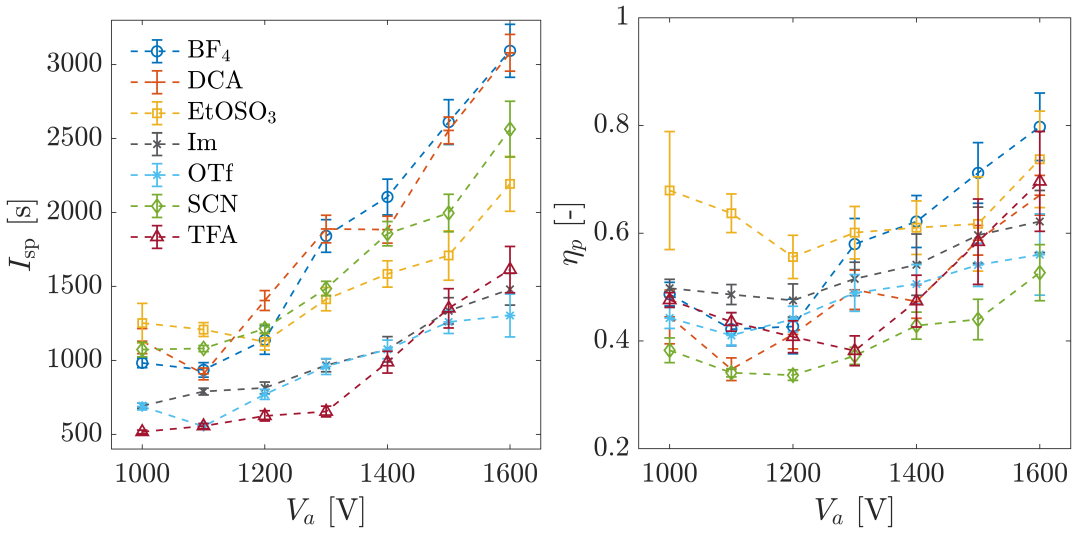

(a) Mean specific impulse

(b) Mean polydispersive efficiency

Figure 4.11: Mean specific impulse (a), I_{sp}, and mean polydispersive efficiency (b), η_p, versus applied voltage, V_a.

The specific impulse is predominantly influenced by the composition of the plume and the mass of droplets. Given the prevalence of droplets at lower voltages, the specific impulse tends to be lower and increases as voltage is raised, as also evidenced by the droplet percentage in the ToF curves. Among the tested liquids, EMI-BF_4 and EMI-DCA exhibit the highest I_{sp} values at 1600 V, measuring 3090 ± 200 s and 3080 ± 150 s, respectively. However, EMI-SCN yields a slightly lower I_{sp} value at 1600 V, standing at 2560 ± 190 s, attributed to the presence of a few droplets with high m/q. EMI-Im, EMI-TFA, and EMI-OTf produce the lowest I_{sp} values, falling within the range of 1200-1500 s at 1600 V. As expected from the ToF spectra, these liquids still feature droplets at higher voltages, significantly penalizing particle acceleration. A different scenario emerges with EMI-$EtOSO_3$, which exhibits a specific impulse of 2190 ± 185 s at 1600 V. Even though droplets are still present in the ToF curves at higher voltages, these droplets are lighter compared to those in the other liquids. Consequently, they achieve higher velocities, leading to an elevated specific impulse. This can be attributed to the increased hydraulic resistance due to the heightened viscosity of EMI-$EtOSO_3$.

The propulsive map in Fig. 4.12 provides a comprehensive overview of the performance of the various liquids. The performance summary of the ILs at the maximum emitter power is given in Tab. 4.4. On one hand, we have EMI-BF_4, EMI-DCA, and EMI-SCN, characterized by their lightweight molecules, resulting in high specific impulse values ranging from 2500 to 3000 s. However, they exhibit a lower thrust-to-power ratio, between 30-40 μN/W. The low viscosity of EMI-DCA and EMI-SCN is advantageous for achieving high emission rates, but it creates a low-impedance system. While their beam current may be nearly pure ionic, they tend to produce high-m/q droplets, which negatively affects polydispersive efficiency and consequently thrust efficiency. This is one of the reasons EMI-BF_4, with a viscosity of $\mu = 44$ mPa/s, achieves the highest

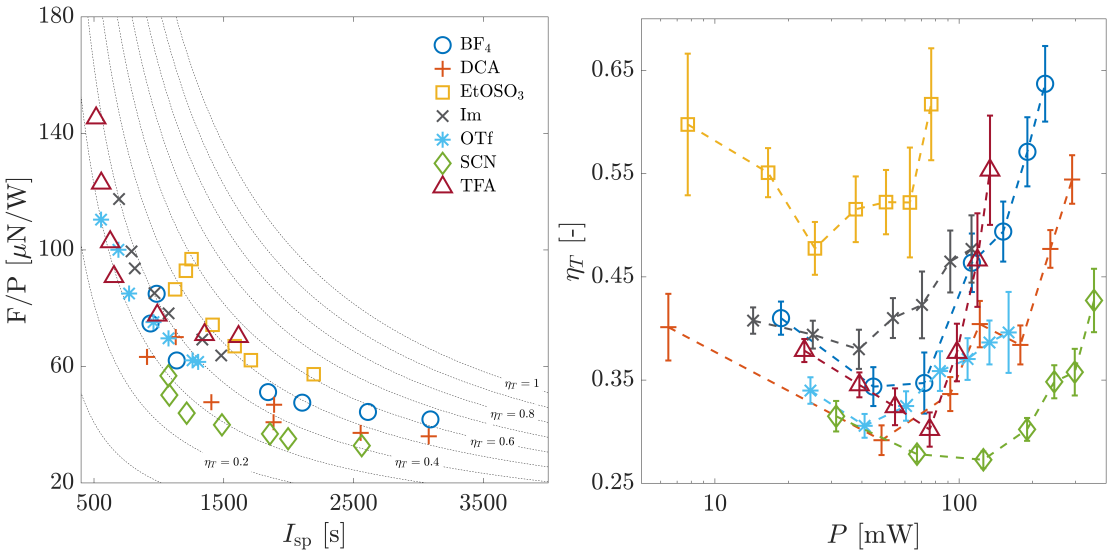

(a) Thrust efficiency map.

(b) Mean thrust efficiency vs mean power.

Figure 4.12: Performance map of the seven ionic liquids, featuring the thrust efficiency map (a) with specific impulse versus thrust-to-power for different thruster efficiency lines, η_T. Mean power, P, versus thruster efficiency (b) is plotted along side to complete the performance picture.

thrust efficiency at 64%. In another category, we find EMI-Im, EMI-OTf, and EMI-TFA, which have lower specific impulse values but exhibit higher thrust-to-power ratios in the range of 60-120 μN/W. However, this higher thrust-to-power ratio is typically observed at low power levels, resulting in lower thrust. EMI-OTf has the lowest thrust efficiency of these three at 40%, while EMI-TFA demonstrates the highest at 56%. Lastly, EMI-$EtOSO_3$ stands in a category of its own, delivering specific impulse values exceeding 1500 s while maintaining a thrust-to-power ratio of around 60 μN/W. Moreover, for a given power level, this ionic liquid presents the highest η_T, with the highest value just falling short of that of EMI-BF_4 at 62%. The properties of EMI-$EtOSO_3$, including high μ and γ, align well with the requirements of externally wetted emitters for reaching a pure ionic regime. However, the drawback of EMI-$EtOSO_3$ is its low emission, resulting in lower thrust.

4.4 Conclusions

This study involved the testing and characterization of seven ionic liquids to evaluate their impact on the propulsive performance of an externally wetted electrospray emitter. EMI-BF_4, EMI-DCA, and EMI-Im were included as benchmarks for comparison with other research and thrusters that have utilized these liquids. Notably, this work represents the first report on externally wetted emitters with EMI-OTf and EMI-SCN. Additionally, it characterizes EMI-$EtOSO_3$ and EMI-TFA for the first time in any emitter topology.

Ionic liquid	P [mW]	I_e [μA]	F/P [μN/W]	F [μN]	I_{sp} [s]	η_T
EMI-BF_4	225	141	41.8	9.4	3090	0.64
EMI-DCA	290	181	36.0	10.4	3080	0.54
EMI-$EtOSO_3$	77	48	57.3	4.4	2190	0.62
EMI-Im	112	70	63.8	7.2	1480	0.48
EMI-OTf	160	100	61.6	9.8	1300	0.40
EMI-SCN	357	223	32.8	11.7	2560	0.43
EMI-TFA	139	84	70.2	9.4	1610	0.56

Table 4.4: Summary of the performance of all tested liquids at an applied voltage of 1600 V, including power (P), emitted current (I_e), thrust-to-power (F/P), thrust (F), specific impulse (I_{sp}), and thrust efficiency (η_T).

The ionic liquids in this study exhibited varying levels of emitted current, with EMI-DCA and EMI-SCN, characterized by high conductivity and low viscosity, resulting the highest emitted currents. In contrast, EMI-$EtOSO_3$, with its higher viscosity, exhibited the lowest emitted current. These findings offer insights into the behavior of ionic liquids. It was observed that ionic liquids with lighter molecules, higher values of electrical conductivity, and surface tension tended to exhibit a greater amount of ion evaporation.

In terms of propulsive performance, EMI-SCN exhibited the highest thrust, generating 11.7 μN, while EMI-$EtOSO_3$ produced the lowest thrust, with 4.4 μN, due to its limited emitted current. It is worth noting that EMI-SCN, despite having lower mass-to-charge ratio, yielded the lowest thrust per μA of emitted current, with EMI-TFA achieving the highest thrust per emitted current in this regard. Moreover, ionic liquids operating in the pure ionic regime displayed the highest specific impulse, with EMI-BF_4 and EMI-DCA achieving values of nearly 3000 s. In contrast, liquids operating in the mixed regime recorded lower specific impulse, with EMI-Im, EMI-OTf, and EMI-TFA falling within the range of 1200-1500 s. EMI-$EtOSO_3$, operating in a mixed regime, exhibited a higher specific impulse, possibly due to its droplets having a lower mass-to-charge. This observation suggests a potential link to the higher viscosity of the liquid, which limits the flow rate in externally wetted configurations, favoring ion extraction. Regarding thrust efficiency, EMI-BF_4 demonstrated the highest efficiency at 1600 V, with a value of 64%, while EMI-SCN exhibited the lowest thrust efficiency at 0.4. Notably, despite the predominantly ionic composition of EMI-SCN plume, the presence of a few droplets with a relatively high mass-to-charge contributed to the reduced polidispersive efficiency.

Ionic liquids with higher conductivity and surface tension display an advantage when it comes to reaching the ionic regime at room temperature, as exemplified by EMI-BF_4, EMI-DCA, and EMI-SCN. However, in the case of EMI-DCA and EMI-SCN, their low viscosity in externally wetted emitters results in the production of few droplets with a sufficiently high mass-to-charge ratio, which in turn penalizes their efficiency. A notable exception is EMI-$EtOSO_3$, which, despite having low conductivity, benefits from its high

viscosity, achieving remarkable values for specific impulse and thrust efficiency with 2190 s and 62%, respectively. EMI-$EtOSO_3$ does have certain drawbacks, including its low emitted current and thrust, but these issues may be addressed by raising the operating temperature, as suggested in previous research [72]. Additionally, EMI-DCA and EMI-SCN are of particular interest due to their hypergolic properties, which opens up the possibility of employing them in a dual propulsion system that combines chemical and electrical propulsion.

* * *

Chapter 5

Computed tomography scanner

The content of the current chapter coincides with the following journal paper:

- **D. Villegas-Prados**, J. Kazadi, M. Wijnen, P. Fajardo, "Emission characterization of externally wetted electrospray thrusters using computed tomography", in Proceedings of 38th International Electric Propulsion Conference, Toulouse, France, June 2024. (**Paper IV**).

Paper content and author contribution

This chapter details the step-by-step development of the computed tomography experiment, fulfilling objective **O.1.4**. To enhance the reliability of the experiment, simulations were conducted to validate both the design and functionality of the diagnostic system. The findings provide a novel understanding of the emission characteristics of the electrospray thruster, offering insights into potential imperfections that could lead to emission instabilities, thereby addressing research gap **G.5**.

A specialized setup was designed, assembled, and tested under a controlled vacuum environment (**O.3**). Additionally, dedicated software was developed by the author to synchronize the thruster voltage with the current collected by the tomography system. A custom post-processing code was also developed to reconstruct the emission profile.

Preliminary results of this investigation were presented at the 2024 International Electric Propulsion Conference (**O.4**).

* * *

Abstract

This study uses computed tomography to map the current density of an electrospray thruster with an asymmetric emission distribution. The setup includes an angular stage to rotate the thruster and a linear stage to sweep a wire across its active area. Simulations showed that for sufficient resolution, the wire should be 1 mm from the extractor, with 50 angular steps and 300 linear or radial steps. CT scans at various voltages revealed that the northern region began emitting at lower voltages, with more regions emitting consistently as voltage increased from 700 V to 1300 V. However, emissions from nearby beamlets sometimes merged, complicating site extraction. Notably, the southwest region showed inconsistent emission. Scanning electron microscope analysis revealed these non-emitting cones had a damaged, volcano-like shape, likely due to handling errors or manufacturing defects.

Nomenclature

j	current density	z	wire-to-cone distance
W	wire width	r	radial position
L	wire length	θ	angular position
N_r	number of radial positions	I_w	wire collected current
N_θ	number of angular positions	I_e	emitted current
I	line integrated current	V_a	applied voltage

Acronyms/Abbreviations

IL	Ionic Liquid
CT	Computed Tomography
PCB	Printed Circuit Board
EMI-Im	1-Ethyl-3-methylimidazolium bis(trifluoromethylsulfonyl)imide
CAD	Computer Aided Design
HV	High Voltage
TIA	Transimpedance Amplifier
SEM	Scanning Electron Microscope

5.1 Introduction

Electrospray propulsion systems have gained significant attention in electric propulsion due to their compact size, high specific impulse, and low power consumption. These attributes render them well-suited for micro and nano satellites, offering enhanced efficiency in the low power range (< 100 W) compared to traditional ion or Hall thrusters [3], [95]. These systems operate by extracting and accelerating charged particles from a conductive liquid, known as Ionic Liquid (IL). Ionic liquids, with their remarkable stability and negligible vapor pressure at room temperature, are an ideal choice for space applications. The operational principle of electrospray involves an emitter in proximity to an extractor grid. By establishing an electric potential difference between the IL and the extractor grid, ions are extracted from the emitter's tip and accelerated to create a high-speed ion jet, generating thrust [96].

However, designing electrospray thrusters comes with many challenges. From an operational perspective, the longevity of electrosprays is a critical concern. The primary limiting factor is the overspray from the emitter to the extractor and the subsequent liquid accumulation on the extractor [150]. Overspray is a critical issue within electrospray systems, as the wide plume angles can result in propellant impinging on the extractor,

causing problems such as grid shorting, electrode aperture clogging, and propellant back spray [151]. These complications have the potential to ultimately lead to thruster failure.

Successfully addressing overspray as a failure mechanism necessitates a thorough comprehension of plume profiles and emission site characterization. Moreover, variations in flow resistance and tip geometry among emission sites, often arising from the design and manufacturing processes, can lead to non-uniform operational and emission characteristics. This variability may give rise to off-axis emission sites that are not aligned with the extractor grid holes, further intensifying the overspray issue.

Computed tomography (CT) scans serve as a valuable tool for characterizing emission sites and for detecting potential failure mechanisms [152]. CT tomography allows us to infer the emission site operation. This enables the analysis of the thruster's beam profile, identification of off-axis emission sites, inefficient current sharing, and non-uniform emission characteristics. These results can be traced back to the manufacturing processes, allowing us to gain insights into the presence of any defective regions within the emitter and to perform a comprehensive quality assessment of the emitters. Additionally, when CT is conducted over an extended period, it becomes possible to monitor changes in emission characteristics [152]. Such changes may be attributed to emitter degradation or clogging, providing valuable information for ongoing maintenance and performance monitoring.

This paper presents the design, implementation, and testing of a computed tomography scan diagnostic with an externally wetted electrospray thruster from IENAI SPACE. Section 5.2 provides background on computed tomography and the approach taken, Section 5.3 explains the experimental setup including the thruster employed, Section 5.4 shows the experimental results, and Section 5.5 concludes the study.

5.2 Methodology and Simulation results

Computed tomography in electrospray thrusters aims to extract the current density distribution, $j(x, y)$, within the thruster plume [153]. This process involves using a wire-probe of width W and length L which is swept radially across the thruster at various angles. If the emission were axisymmetric, sweeping the wire at a single angle would suffice to reconstruct the current density map. However, this ideal scenario is rare, necessitating measurements across a range of radial positions N_r and angular positions N_θ.

Each measurement at a specific radial position r and angle θ represents the line-integrated current density along the wire's length and width, denoted as $j(r, \theta)$. In practice, measurements are continuously obtained over time, resulting in the formation of a matrix $I(r, \theta)$ with discrete values corresponding to N_r and N_θ. The integral expression for the line-integrated current density is given by:

$$I(r,\theta) = \int_L j(x,y)W\,dl \tag{5.1}$$

The measured projections $I(r,\theta)$ form a sinogram, which is a key component in the process of reconstructing a 2D image. This reconstruction is achieved using the inverse Radon transform, as detailed by [154]. The inverse Radon transform allows for the reconstruction of an object from its projections. Despite the lack of a practical, exact implementation of the inverse Radon transform, several highly effective approximate algorithms have been developed to perform this reconstruction accurately.

The method commonly employed for reconstructing images is the Filtered Back Projection (FBP). This technique involves applying the Fourier transform to the projections, followed by interpolation in Fourier space to obtain the 2D Fourier transform of the image. This transformed image is then inverted to yield the reconstructed image. FBP is one of the fastest methods for performing the inverse Radon transform. The primary tunable parameter in FBP is the filter applied to the Fourier-transformed projections. In this study, a Shepp-Logan filter is used to suppress high-frequency noise in the reconstruction.

Implementing this algorithm is relatively straightforward in MATLAB, which provides a built-in function, *iradon*, for performing the inverse Radon transform. By inputting the sinogram and selecting the desired filter, *iradon* efficiently reconstructs the image using the FBP method.

5.2.1 Simulations

Several simulations were performed to understand the number of angular and linear data points needed, as well as the wire distance required to accurately identify the emission sites in the electrospray thruster. For this purpose, the thruster setup was constructed with each emission site assumed to emit with a Gaussian profile. The width of the profile was based on empirical data of the far plume current distribution. A random generator was implemented to ensure that not all cones emitted uniformly, introducing variations in the emitted current per cone.

Once the random emission profile was generated, the algorithm passed a wire at a specified distance z from the tip of the cone, at various positions (r,θ), to reconstruct the sinogram. The Radon transform was then applied to the sinogram to obtain the computed tomography scan.

Fig. 5.2 illustrates the reconstructed image for fixed values of $N_\theta = 50$ and $N_r = 300$, and for different wire distances $z = 0.5, 1, 1.5$ mm. Fig. 5.1 shows the reconstructed image for $z = 1$ mm and $N_r = 300$, with varying N_θ.

Ideally, the wire should be swept as close as possible to the extractor to identify each individual emission site. As the wire distance increases, the individual beamlets merge, making it difficult to differentiate between emission sites. Therefore, placing the wire as

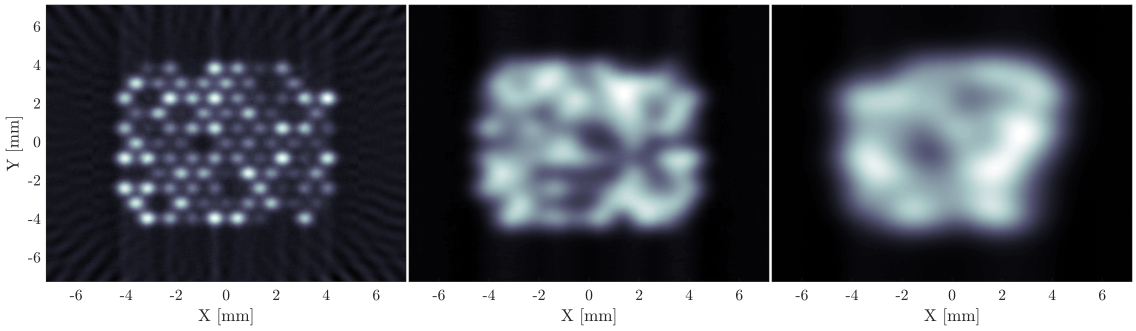

Figure 5.1: Simulated computed tomography for $N_\theta = 50$ and $N_r = 300$, and for different wire distances, $z = 0.5, 1, 1.5$ mm.

close as possible to the extractor is crucial.

Regarding the number of angular and linear steps, N_r is fixed by the amount of data points obtainable in a single sweep. On the other hand, different values of N_θ have been simulated for the case where $z = 1$ mm and $N_r = 300$. It was observed that with $N_\theta = 10$, the 2D map is quite noisy, and the quality improves as N_θ is increased. The drawback of increasing the number of angular steps is the increased time required to complete the entire test. However, this dataset represents a perfectly created emission scenario, whereas in reality, even with a high number of steps and close wire distance, emissions may still exhibit noise.

The parameters chosen for the test are $z = 1$ mm, $N_r = 300$, and $N_\theta = 50$.

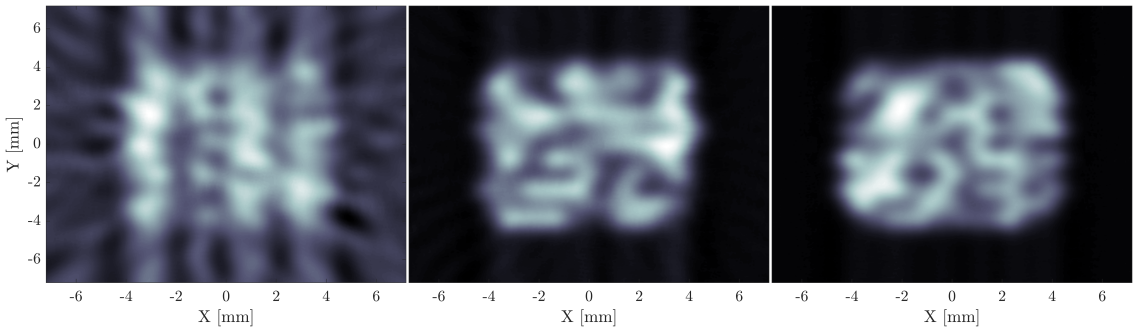

Figure 5.2: Simulated computed tomography for $z = 1$ mm and $N_r = 300$, and for different angular steps, $N_\theta = 10, 30, 50$

5.3 Experimental methods

5.3.1 Thruster description

The electrospray thrusters used in this study [72] consist of an borosilicate-based extractor grid and an oxidized, silicon-based externally wetted emitter array, featuring 101 micro cones with nano-texturization to control the hydraulic resistance and a propellant reservoir

for liquid storage. In addition, the emitter includes multiple feeding holes that allow the ionic liquid to flow passively from the reservoir positioned beneath the emitter to the emission sites. To ensure an uninterrupted liquid connection between the emitter and reservoir, a porous textile material is inserted. The reservoir itself is constructed using 3D printing technology, employing a porous aluminum piece. A schematic of a single micro-cone is shown in Fig. 5.3. The ionic liquid used in this work is 1-Ethyl-3-methyl-imidazolium bis-trifluoromethylsulfonyl-imide, also known as EMI-Im or EMI-NTf2 in the literature. Ionic liquids are room temperature molten salts composed of positively charged cations and negatively charged anions.

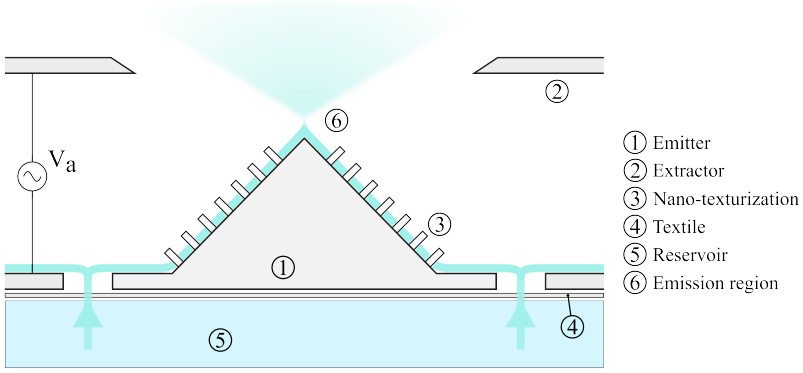

Figure 5.3: Schematic of externally wetted emitted with nano-texturization for impedance control (not to scale), featuring emitter, extractor grid and reservoir.

5.3.2 Computed tomography setup

To perform tomography measurements, we utilized linear and rotary stages, specifically the X-LSM50A-SV2 and X-RSW60A-SV2 models from Zaber, which are vacuum-rated. The linear stage is equipped with a manual vertical stage mounted atop its sliding platform. This vertical stage is used to place the wire at the desired distance from the extractor grid and it has mounted a custom "handsaw" metal piece that houses a printed circuit board (PCB) for establishing the electrical connection to the wire. At one extremity of the handsaw plate, a tensioning mechanism is incorporated to ensure the wire remains taut. The wire connects to the PCB via a screw, and SMA makes the connection with air-side. Movement of the linear stage facilitates the necessary linear measurements by displacing the wire accordingly.

Conversely, the rotary stage supports the thruster, with its electrical connections facilitated through a liquid connector housed within a borehole at the center of the rotary stage. This liquid connector is affixed to a PCB with a screw, enabling seamless electrical connectivity to the thruster. This configuration permits unobstructed rotation of the thruster without the risk of cable entanglement. Fig. 5.4 presents a CAD rendering of the computed tomography setup alongside an actual image of the thruster positioned within the setup.

Due to assembly constraints, the extractor grid is positioned 0.5 mm below the top part of the assembly holder. Adding this distance to the cone tip-to-extractor distance of 0.1 mm results in a minimum distance of 0.6 mm. To ensure a margin of 0.4 mm from the assembly and to avoid wire breakage, the wire distance was set to 1 mm. The wire, made of tungsten, has a diameter of 25 μm.

On the air-side, the wire current connection is linked to a transimpedance amplifier (TIA) with a 1 MΩ gain. The thruster is operated using a high-voltage (HV) amplifier. A dedicated software system ensures synchronization between the stage movements and thruster operation.

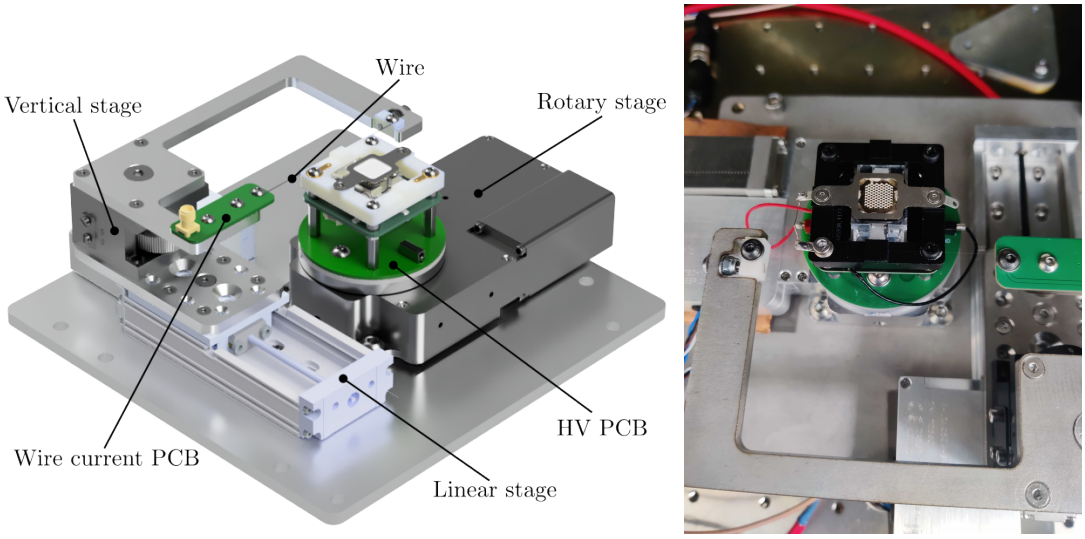

Figure 5.4: CAD of tomography assembly and actual image of the thruster mounted on top of the tomography setup.

5.3.3 Vacuum facilities

The tests were conducted at the IENAI SPACE facilities located in Leganés, Madrid, Spain. The vacuum facility features a cylindrical chamber with an 800 mm diameter and a length of 1000 mm, extended to a maximum length of 1200 mm due to its curved ends. This chamber includes a retractable plate with mounting holes for securing the experimental setup. The chamber pressure is maintained at 10^{-6} mbar throughout the tests by an Edwards 400 nEXT turbo-molecular pump. Fig. 5.5 depicts the chamber housing the computed tomography experiment and the thruster.

5.3.4 Operation procedure

To achieve high-resolution computed tomography, we have determined that numerous linear and angular steps are required. Ideally, a rapid snapshot of the current is desired;

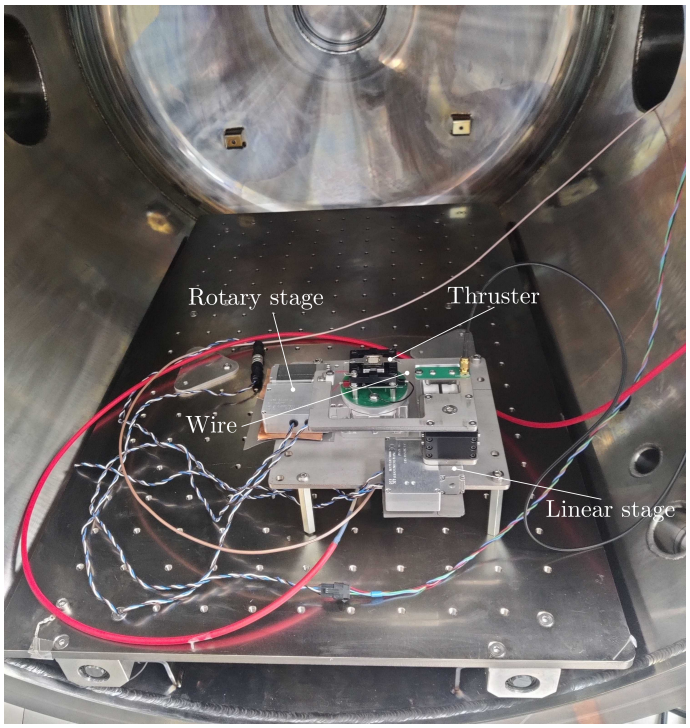

Figure 5.5: Vacuum chamber and computed tomography setup with electrospray thruster and connections before the start of the test.

however, in practice, the tomography process is time-consuming, and the thruster's dynamics may change over this period. To optimize time efficiency, the linear stage moves across the thruster during the high-voltage on-state at a sufficiently low speed to capture an adequate number of data points. This is synchronized such that the linear stage moves forward when the emission is negative and the thruster moves backward when the emission is positive. Upon completing a cycle, the voltage ramping time is utilized to adjust the angular stage to the next angle. This method ensures data collection at fixed angular steps, with the linear stage sweeping to obtain the wire current distribution $I_w(x)$ along the axial direction. This process is repeated for all angles.

This process is conducted at seven operational voltages ranging from 700 V to 1300 V, in increments of 100 V. The synchronization details are illustrated using the data for $V_a = 1100$ V, which includes the applied voltage, emitted current, wire current, and both angular and linear positions, as shown in Fig. 5.6. A close-up of one cycle is depicted in Fig. 5.7.

The high-voltage (HV) trapezoidal waveform features a 30-second HV period with 6-second ramps, resulting in a total duration of 1 minute and 24 seconds per angle. With $N_\theta = 50$, the overall test duration is 70 minutes. Ensuring the thruster's steady operation throughout this period is critical. The emitted current data, presented in the figure, confirms that the current remained constant throughout all the tests.

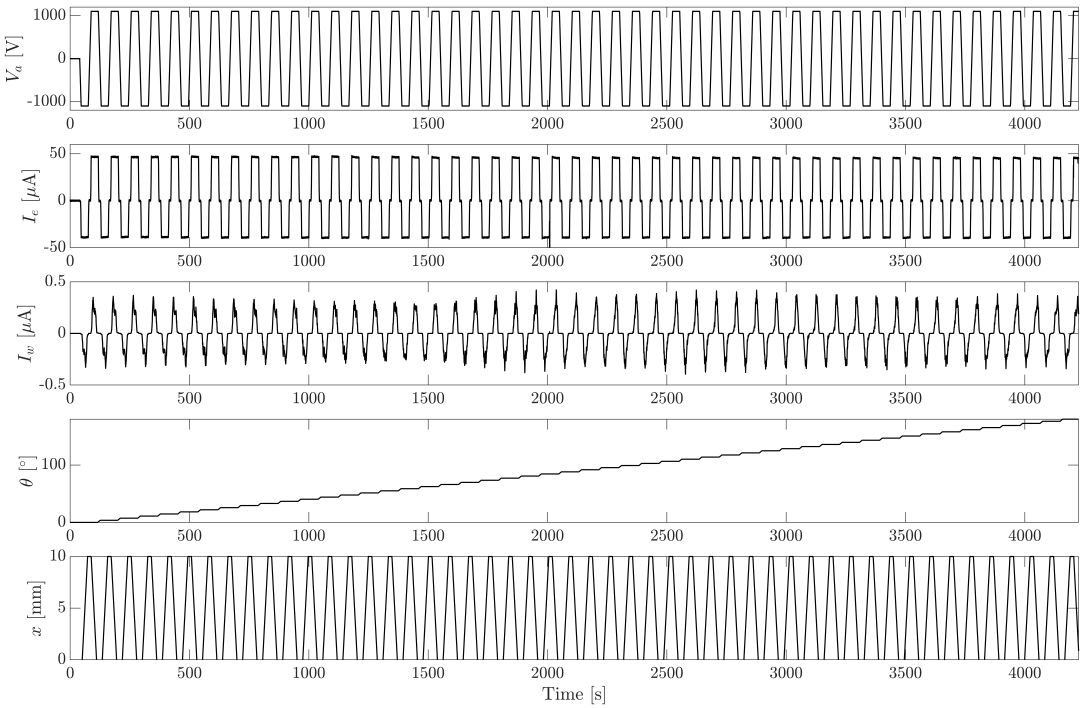

Figure 5.6: Applied voltage, emitted current, collected wire current, and angular and linear movement over time for a whole computed tomography scan at a given voltage.

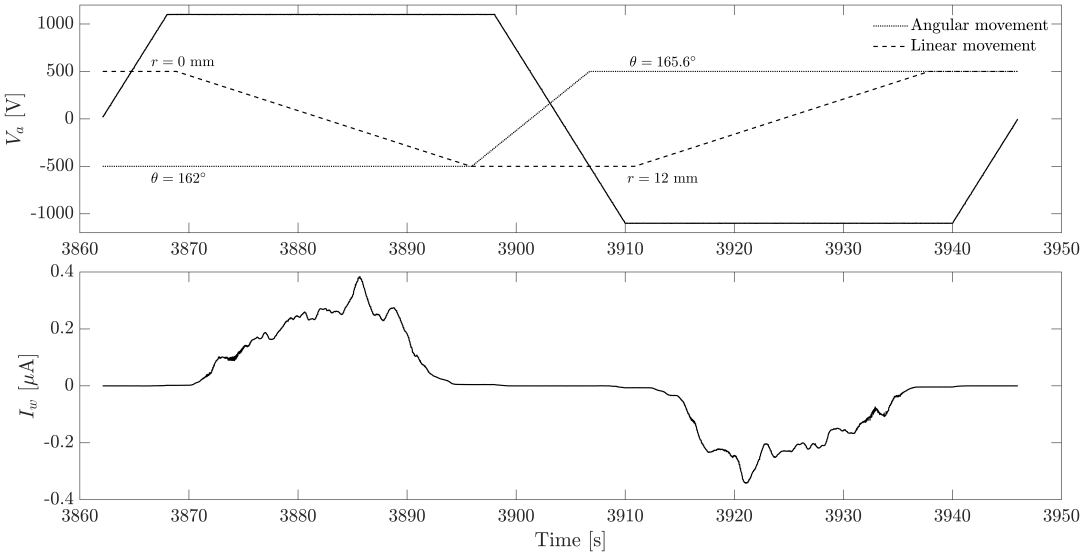

Figure 5.7: Snapshot of a single cycle showing how the angular and linear movement are synchronized with the applied voltage to obtain the wire current.

5.4 Experimental results

5.4.1 Thruster current-voltage characteristics

The emitted current for a single cycle at each tested voltage is illustrated in Fig. 5.8. Across all cases, the emitted current exhibits stability, albeit showing minor variations in

the negative polarity at higher voltages, typically within the range of 1-2 μA. Fig. 5.9 presents the mean emitted currents for all tested voltages, along with their respective standard deviations. Notably, at 1200 V, the maximum deviation is observed with emitted currents of 92 ± 1.6 μA and −79 ± 2.3 μA, respectively. The first test at 700 V was performed close to the onset of emission, currents were recorded as +1.5 ± 0.3 μA and −1.2 ± 0.3 μA, and this case will help highlighting the initial emission sites.

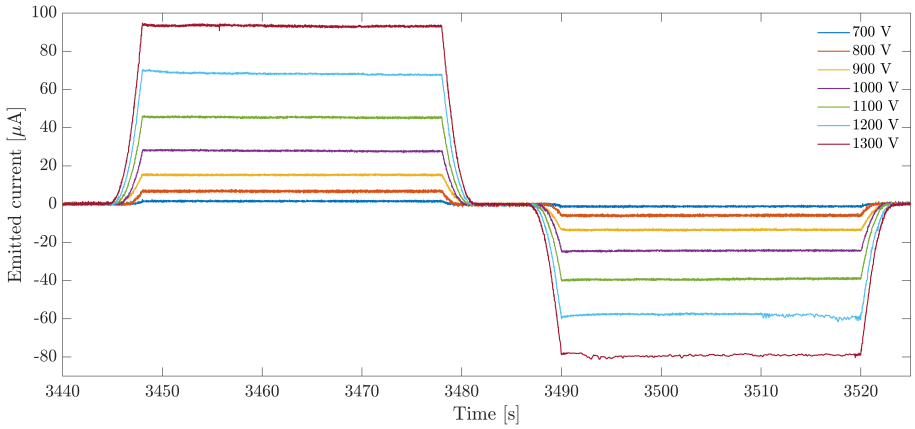

Figure 5.8: Snapshot of emitted current cycle for the different voltage cases tested.

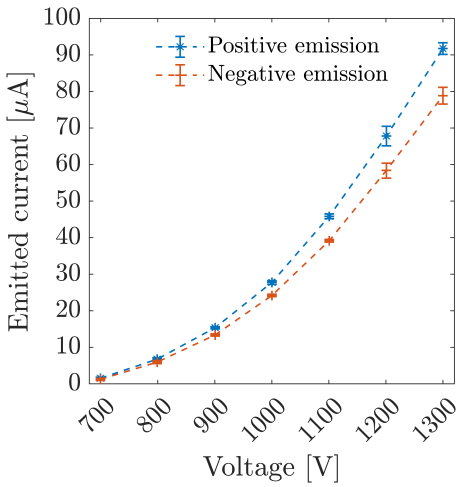

Figure 5.9: Current-voltage curve for positive and negative emission with standard deviation bars.

5.4.2 Computed tomography current maps

For all the reconstructed tomography maps, the cone-to-wire distance was set to 1 mm, the number of angular steps is $N_\theta = 50$, and the linear stage is swept at roughly 0.3 mm/s, corresponding to $N_r = 300$ in post-processing. Despite the stages having an extremely high step resolution of 20 μm, the primary limiting factor remains the data collection rate across all devices.

In Figure 10, the CT scan for positive emission is shown on the left and for negative emission on the right, with increasing applied voltage. The intensity in each image is normalized relative to its own maximum for optimal visualization. To provide clear orientation, the images use a north-south-east-west nomenclature to describe locations within them.

A notable observation is that the emission sites appear identical for both positive and negative polarity voltages across all tested conditions, indicating consistent emission from the same locations regardless of voltage polarity.

At 700 V, initial emission sites are concentrated in the northern part of the emitter, with minimal emission observed in the southern part. The data at this voltage exhibit higher noise levels, and emission sites appear larger compared to other voltage settings. Increasing the voltage to 800 V introduces additional emission sites, primarily located in the northern part of the emitter. By 900 V, emission sites begin to emerge in the southeast region of the emitter. As voltage further increases to 1000 V, the emission pattern becomes more uniform across the emitter, although the southwest region remains inactive with only a few low-intensity emission sites. Similar distributions are observed at 1100 V and 1200 V, with a noticeable absence of emission in a specific region. At 1300 V, sporadic emission is observed in the southwest region, but it remains significantly less pronounced compared to the rest of the emitter.

Additionally, it is noteworthy that the emitter lacks a central cone, which is why no emission is observed in the center of the images across all cases. Besides the non-emitting southwest region, it appears that specific cones do not emit consistently, indicated by regions with significantly reduced or absent intensity.

5.4.3 Scanning electron microscope images

Tomography serves as a crucial diagnostic tool, enabling the characterization of individual emission sites and providing insights into their emission behaviors. However, deriving meaningful conclusions regarding non-emitting regions necessitates aligning CT results with the emitter's fabrication details.

To discern differences among cones in various regions, the emitter was analyzed using a Scanning Electron Microscope (SEM). Imaging was conducted with a FEI Teneo at the Electron Microscopy Unit of Universidad Carlos III de Madrid. Figure 11 displays images from the top of the southwest and northeast quadrants, with Figure 12 providing close-up views of cones in each region.

The SEM images reveal that cones in the southwest region do not emit due to tip loss, resulting in a volcano-shaped structure. This observation correlates with the emission map from tomography, highlighting the compromised state of these cones. This particular emitter was exclusively used for testing purposes and has not been utilized subsequently, suggesting that the volcano-shaped cones may have resulted from mishandling

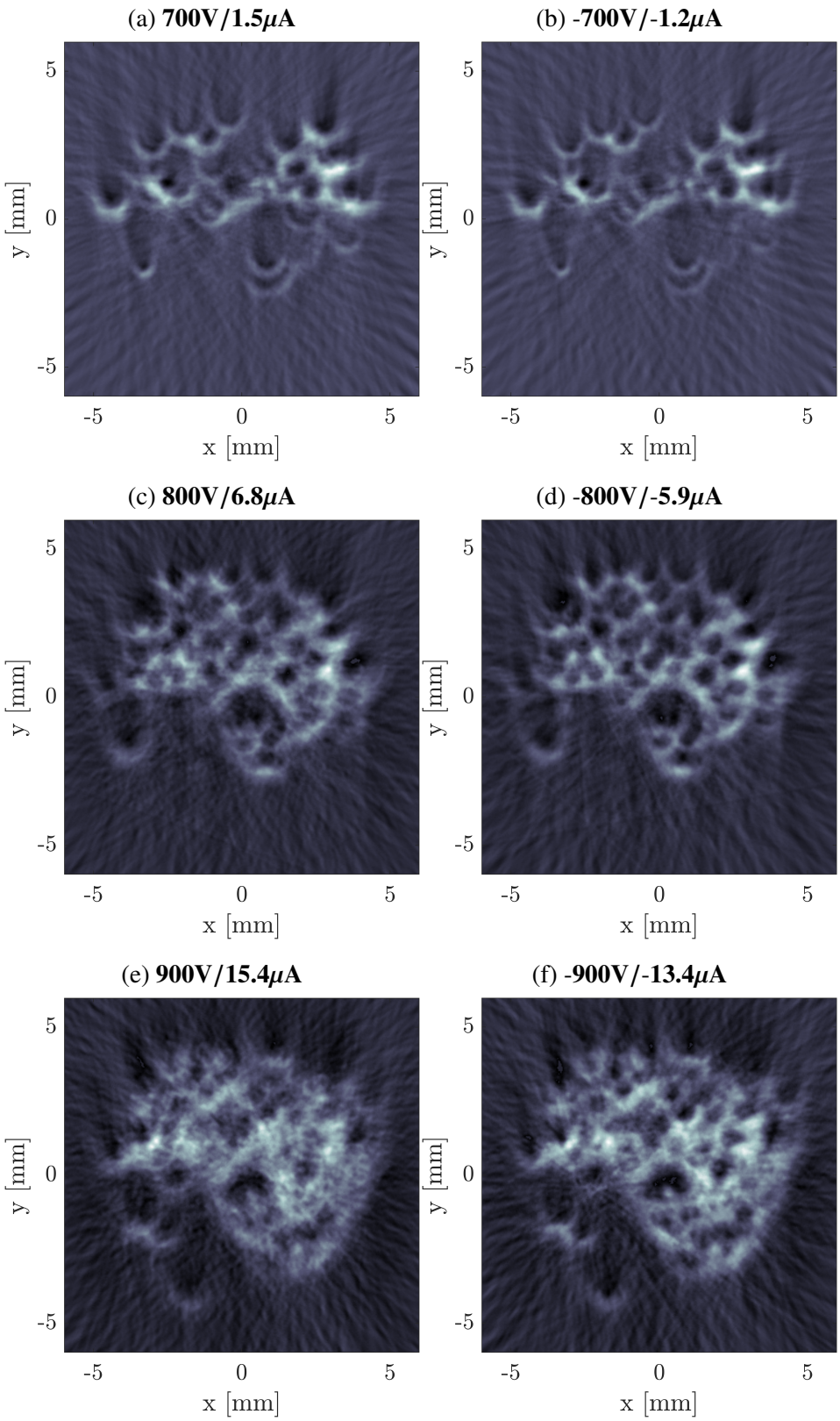

during manufacturing or corrosion caused by the ionic liquid. Among these possibilities, mishandling appears most plausible, though further investigation is required for definitive conclusions.

Nevertheless, the potential of tomography in diagnosing emitter issues has been un-

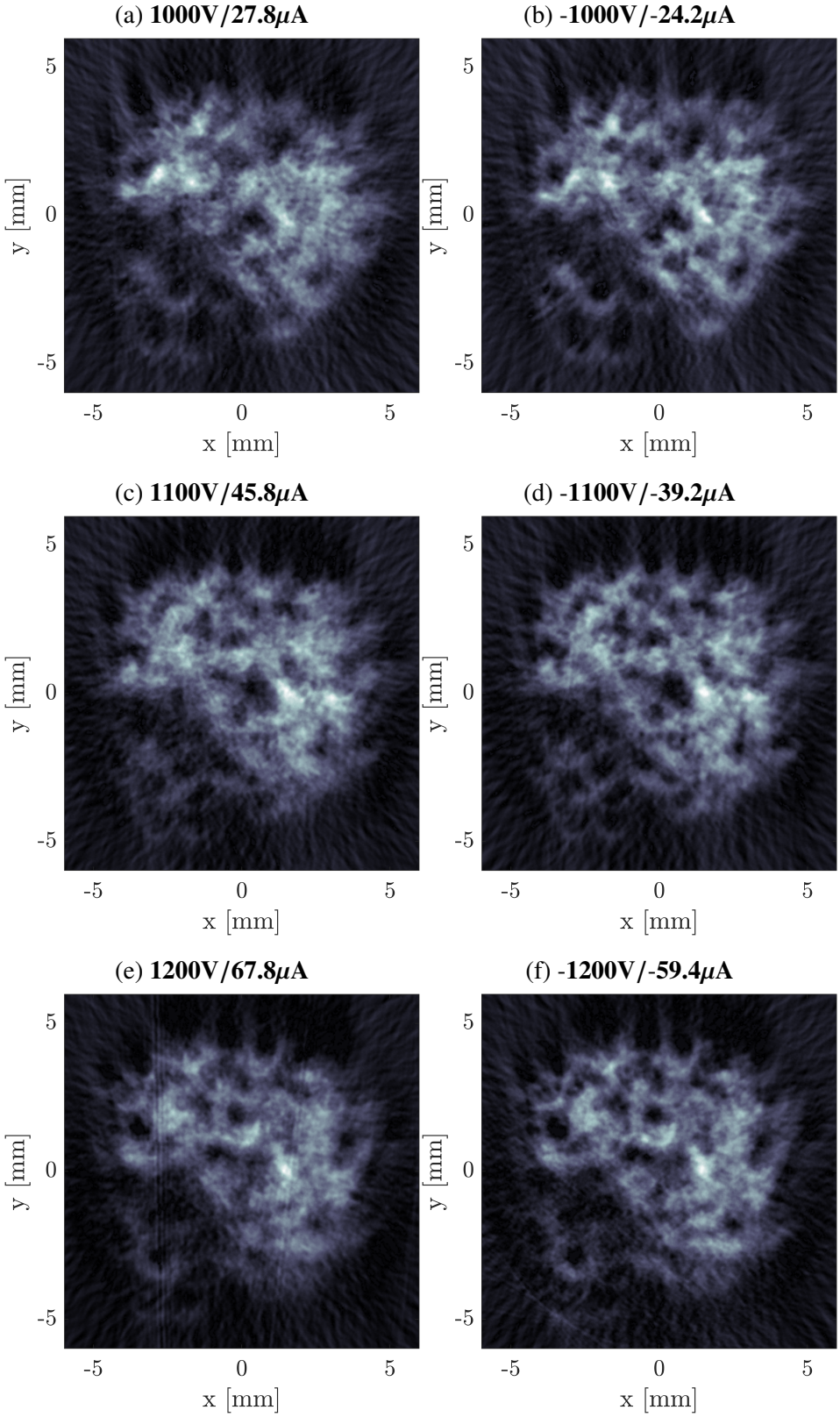

derscored, demonstrating its capability to detect and infer problems affecting emitter performance.

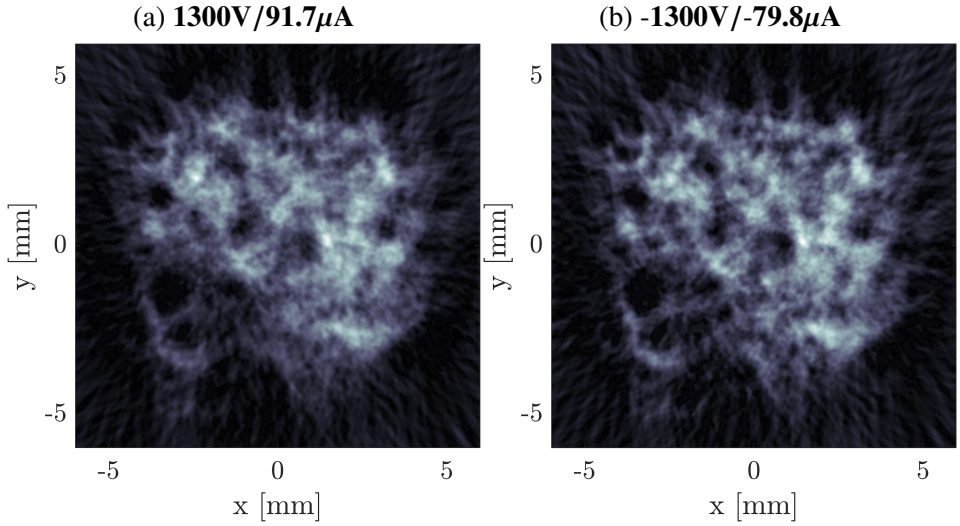

Figure 5.10: Computed tomography maps at different operating voltages for positive and negative polarity.

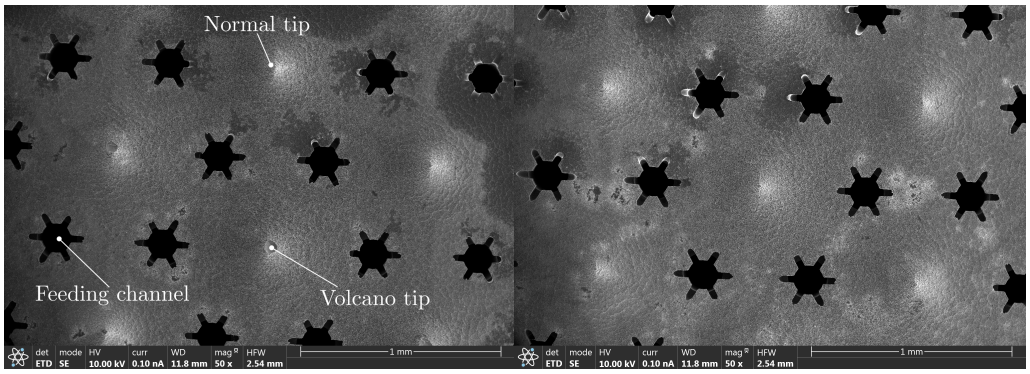

Figure 5.11: SEM images of southwest and northeast region.

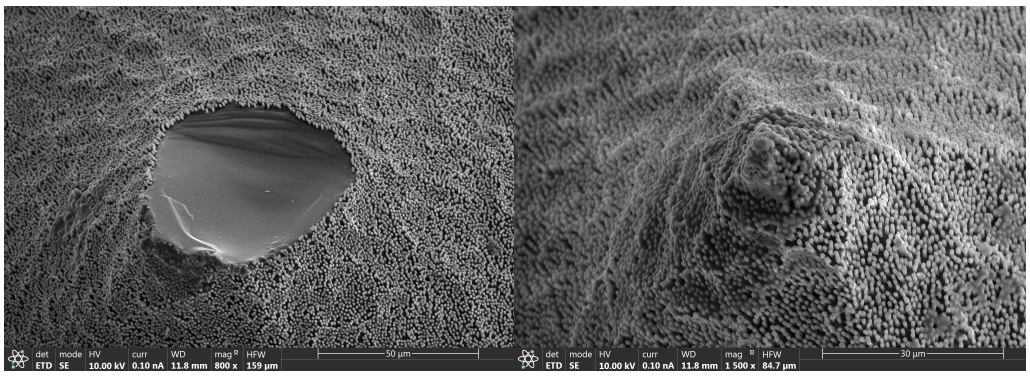

Figure 12: SEM close-up pictures of the cones with volcano shape and normal ones.

5.5 Conclusion

A computed tomography method has been developed to reconstruct the current density map of an electrospray thruster with an asymmetric distribution. The setup consists of an

angular stage that rotates the thruster and a linear stage that sweeps the wire across the thruster's active area. Simulations indicated that for a CT scan with sufficient resolution to distinguish emission regions, the wire must be positioned 1 mm from the extractor. Furthermore, a large number of angular and linear steps are required for the reconstruction, with $N_\theta = 50$ and $N_r = 300$ in our case. This is primarily due to the compact design of the thrusters at IENAI SPACE, where the distance between cones is 0.8 mm.

A key aspect of computed tomography is ensuring that the thruster operates steadily throughout the test duration. This was confirmed with tests lasting approximately 70 minutes, during which a steady emission was maintained for all tested voltages. Significant effort was also invested in developing synchronization software to enable continuous sweep measurements of positive and negative emissions at different angles.

The computed tomography scans at different voltages show an increase in emission with voltage. The northern region of the emitter starts emitting at lower voltages, and as the voltage increases from 700 V to 1300 V, more regions begin emitting consistently. Emission sites can be extracted from the maps, but this is challenging as emissions from nearby beamlets sometimes merge. A wire probe positioned closer to the exit plane could improve the reconstruction, but improvements in the assembly are needed to allow the wire to be positioned closer to the extractor.

The most notable observation from the maps is the southwest region, which did not show consistent emission despite increasing the voltage, with only a few spots emitting slightly. To verify and understand the reason behind this anomaly, the emitter was examined using a scanning electron microscope. It was found that the non-emitting cones were "eaten away" and had a volcano shape, in contrast to the other cones that maintained their cone-like shape. Several theories can be proposed about the state of these cones, but most converge on the fact that the emitters are extremely fragile, and any error during handling can damage them, as observed in the images.

These measurements constitute the first data we have obtained from computed tomography. Future efforts will focus on improving the setup to achieve closer maps where individual cones can be differentiated. Additionally, it will be interesting to conduct long-term firings where computed tomography is periodically performed to observe how the emission sites change over time. Furthermore, a Faraday probe could be positioned in future experiments to obtain the far plume angular distribution and correlate it with the tomography results.

* * *

Chapter 6

Conclusions and Future work

This final chapter highlights the key findings of the research conducted throughout this dissertation and presents the derived conclusions, emphasizing the main takeaways and contributions. Additionally, it proposes directions for future research.

6.1 Conclusion

This dissertation presents experimental performance data of an externally wetted electrospray thruster that is being developed by IENAI SPACE, focusing on the development of diagnostic tools and on the characterization of this thruster under different conditions, from voltage and temperature dependence to the use of different propellants.

Each published work delves into the identified research gaps fulfilling the objectives set for the thesis. Below there is a summary of the conclusion of each article organized by chapter

- *Chapter 2 - Development of diagnostics tools*: introduced a novel bipolar high-voltage pulse generator designed specifically for time-of-flight mass spectrometry in electrospray thrusters. The generator, based on a Forward-Flyback with Cockcroft-Walton voltage multiplier, operates efficiently from a 5V DC supply, producing rapid bipolar kilovolt pulses with minimal voltage drop. Experimental validation confirms the generator's ability to provide configurable pulse amplitudes and achieve fast rise and fall times, which are essential for accurately analyzing the plume composition of electrospray sources. This innovation proves particularly effective in driving electrostatic shutter gates and characterizing particle emissions, enhancing the understanding of plume dynamics in electrospray systems.

- *Chapter 3 - Thruster characterization on different operating points*: expands on this by studying the impact of voltage and propellant temperature on plume composition and thruster performance. The research uniquely characterizes the emission regime of an externally wetted electrospray thruster across different temperatures and volt-

ages, revealing the effects on thrust, specific impulse, and efficiency. Findings show that both increased voltage and temperature negatively affect angular efficiency and shift the emission regime from a pure ionic state to a mixed state, particularly at higher temperatures. This shift is attributed to the temperature-induced changes in ionic liquid properties such as viscosity, which affect the flow rate, altering the emission characteristics.

- *Chapter 4 - Testing of new ionic liquids*: explores the propulsive performance of various ionic liquids in externally wetted electrospray emitters, offering the first characterization of several new ionic liquids in this application, such as EMI-Otf and EMI-$EtOSO_3$. The study reveals significant differences in emitted current, thrust, specific impulse, and efficiency among the tested liquids, driven by variations in conductivity, viscosity, and surface tension. Ionic liquids like EMI-DCA and EMI-SCN, despite high conductivity, show lower thrust efficiency due to the formation of droplets with high mass-to-charge ratios. The findings suggest that selecting ionic liquids with suitable properties, such as high viscosity and appropriate conductivity, can optimize performance for externally wetted electrospray, as they allow to reduce the flow rate and achieve a regime close to pure ionic regime. EMI-BF_4 remains the best ionic liquid in terms of performance. Moreover, the study highlights the potential of certain ionic liquids for dual propulsion systems, combining chemical and electrical propulsion, such as EMI-SCN or EMI-DCA.

- *Chapter 5 - Computed tomography scan*: presents a computed tomography method to reconstruct current density maps of electrospray thrusters with asymmetric distributions. The method involves rotating the thruster and sweeping a wire probe across its active area, providing detailed insights into emission characteristics and identifying non-emitting regions. Experimental results demonstrate that emission sites and their characteristics vary with applied voltage, with some regions failing to emit due to damage or degradation. This chapter also discusses the fragility of emitters and suggests improvements in assembly and handling.

6.2 Future work

The development of the suite of diagnostics facilitate future characterization of the thruster. However, there are quite a few things that could be improved. First, the development of a synchronization algorithm could enabled the alignment of the HVPG pulse with the desired point of the up-voltage of the thruster's square wave, facilitating the resolution of particles present in the plume during different phases of a single cycle. Additionally, a lifetime test based on periodic time-of-flight analysis can been implemented to study the evolution of plume composition over time. This method could help identify potential issues such as degradation, or clogging, which may affect thruster performance.

Another potential improvement is the combined development of an RPA and TOF techniques. By incorporating an RPA, TOF measurements can be taken as a function of stopping voltage, enabling a more precise analysis of species composition and distinguishing between particles generated in the acceleration region or the field-free region. This approach contributes to a more accurate efficiency analysis by facilitating independent evaluation of different particles [71], [77].

Studies on capillary emitters suggest that localized heating of the emission region increases the range of ion emission stability, leading to a more ionic regime [155]. Our research focuses on heating the entire propellant buffer, a strategy more aligned with practical engineering solutions. Nonetheless, it would be insightful to conduct similar experiments as those performed with capillary emitters, but by externally heating only the tip of the cone. While this approach would offer a direct comparison to capillary-based studies, its implementation poses challenges due to the emitter's geometric constraints.

Furthermore, an interesting avenue for future work involves comparing the results obtained through indirect diagnostic methods with direct measurements from a thrust balance. Preliminary results suggest comparable thrust values between the two methods, though mass flow measurements diverge. Additional investigation is required to understand the mechanisms underlying this disparity. Recent studies [156] indicate that neutral evaporation from the electrospray emitter may be a contributing factor. While TOF experiments cannot detect these neutral particles, thrust balances can [157]. Understanding the role of neutral evaporation will be critical to fully characterizing thruster performance.

In terms of performance characterization, several additional experiments could provide valuable insights. For instance, combining TOF mass spectrometry with the rotation stage could offer performance data at different angles. Theoretically, heavier particles should be ejected more centrally, while lighter molecules are repelled outward by Coulomb forces, resulting in an ion-dominated plume at higher angles and droplet concentration near the center. Performing similar experiments with the RPA would allow for energy distribution measurements at varying angles.

Significant gaps remain in the study of ionic liquids, particularly regarding their application in electric propulsion. The rapid development of ILs for both propulsion and electrochemical purposes opens the possibility of synthesizing ILs specifically tailored for electrospray thrusters. Expanding the database of ILs by testing their properties—especially conductivity, surface tension, and viscosity—will provide critical insights into their emission characteristics and performance.

The ionic liquid EMI-EtOSO_3 will undergo further characterization at different operating temperatures. This liquid shows promise, as increasing its temperature may enhance emission currents and thrust while maintaining high viscosity, which is desirable for a higher hydraulic impedance. This balance would allow operation within a pure ionic regime, maximizing specific impulse and polydispersive efficiency.

Another promising area of exploration involves high-temperature ionic liquids (HTILs),

which are solid at room temperature but melt at higher temperatures (above 60°C). These propellants share similar properties with room-temperature ionic liquids and could be used in comparable applications. Despite the higher power requirements due to elevated operating temperatures, HTILs offer simplified storage solutions and could be integrated into smaller platforms such as picosatellites. Electrospray applications for HTILs remain unexplored, representing a key focus for future research.

Finally, the full potential of the computed tomography scanner has yet to be realized, as the system was recently completed. By bringing the wire closer to the structure, spatial resolution can be significantly enhanced. When correlated with simulations, this technique could resolve individual cones within the emitter array. Additionally, performing tests with a single emitter may reveal off-axis emissions [158]. The primary goal of tomography in this context is to correlate emission profiles with manufacturing imperfections and quantify their impact on thruster performance. Computed tomography can also be applied over time to capture dynamic changes in emission behavior, enabling traceability of each part of the emitter array rather than relying on the overall current measurements from the entire thruster.

Bibliography

[1] nanosats.eu, *Total nanosatellites and cubesats launched*, Accessed: 2024-07-30, 2024. [Online]. Available: https://www.nanosats.eu.

[2] D. Krejci and P. Lozano, "Space propulsion technology for small spacecraft," *Proceedings of the IEEE*, vol. 106, no. 3, pp. 362–378, 2018.

[3] K. Lemmer, "Propulsion for cubesats," *Acta Astronautica*, vol. 134, pp. 231–243, 2017. DOI: 10.1016/j.actaastro.2017.01.048.

[4] E. Stuhlinger, *Ion propulsion for space flight*. McGraw-Hill New York, 1964, vol. 62333.

[5] I. Levchenko, D. M. Goebel, and K. Bazaka, "Electric propulsion of spacecraft," *Physics Today*, vol. 75, no. 9, pp. 38–44, 2022. DOI: 10.1063/PT.3.5081.

[6] O. O. Baranov *et al.*, "Miniaturized plasma sources: Can technological solutions help electric micropropulsion?" *IEEE Transactions on Plasma Science*, vol. 46, no. 2, pp. 230–238, 2017. DOI: 10.1109/TPS.2017.2773073.

[7] V. Khayms, "Advanced propulsion for microsatellites," Ph.D. dissertation, Massachusetts Institute of Technology, 2000.

[8] Á. Somogyi, "Mass spectrometry instrumentation and techniques," in *Medical applications of mass spectrometry*, Elsevier, 2008, pp. 93–140. DOI: 10.1016/B978-044451980-1.50008-2.

[9] J. Zeleny, "The electrical discharge from liquid points, and a hydrostatic method of measuring the electric intensity at their surfaces," *Physical Review*, vol. 3, no. 2, p. 69, 1914. DOI: 10.1103/PhysRev.3.69.

[10] J. Zeleny, "Instability of electrified liquid surfaces," *Physical review*, vol. 10, no. 1, p. 1, 1917. DOI: 10.1103/PhysRev.10.1.

[11] G. I. Taylor, "Disintegration of water drops in an electric field," *Proceedings of the Royal Society of London. Series A. Mathematical and Physical Sciences*, vol. 280, no. 1382, pp. 383–397, 1964. DOI: 10.1098/rspa.1964.0151.

[12] M. Dole, L. L. Mack, R. L. Hines, R. C. Mobley, L. D. Ferguson, and M. B. Alice, "Molecular beams of macroions," *The Journal of chemical physics*, vol. 49, no. 5, pp. 2240–2249, 1968. DOI: 10.1063/1.1670391.

[13] V. E. Krohn Jr *et al.*, "Liquid metal droplets for heavy particle propulsion," in *Electrostatic propulsion*, Elsevier, 1961, pp. 73–80. DOI: 10.2514/5.9781600864797.0073.0080.

[14] V. E. Krohn Jr, "Glycerol droplets for electrostatic propulsion," *Progress in Astronautics and Aeronautics*, vol. 9, 1963. DOI: 0.2514/5.9781600864865.0435.0440.

[15] T. BATES, J. Mahoney, R. MOORE, J. PEREL, and A. YAHIKU, "Research on a charged particle bipolar thrustor," in *6th Electric Propulsion and Plasmadynamics Conference*, 1967, p. 728. DOI: 10.2514/6.1967-728.

[16] S. Rocca, C. Menon, and D. Nicolini, "Feep micro-thrust balance characterization and testing," *Measurement Science and Technology*, vol. 17, no. 4, p. 711, 2006. DOI: 0.1088/0957-0233/17/4/016.

[17] M. Gamero-Castano, I. Aguirre-de-Carcer, L. De Juan, and J. Fernández de la Mora, "On the current emitted by taylor cone-jets of electrolytes in vacuo: Implications for liquid metal ion sources," *Journal of applied physics*, vol. 83, no. 5, pp. 2428–2434, 1998. DOI: 10.1063/1.367002.

[18] E. Cohen and D. GORDON, "A 100-kv, 10-w heavy-particle thrustor," in *2nd Annual Meeting*, 1965, p. 377. DOI: 10.2514/6.1965-377.

[19] P. Kidd and H. Shelton, "Life test/4350 hours/of an advanced colloid thruster module," in *10th Electric Propulsion Conference*, 1973, p. 1078. DOI: 10.2514/6.1973-1078.

[20] A. Shtyrlin, "State of the art and future prospects of colloidal electric thrusters," in *24th International Electric Propulsion Conference, Moscow, Russia*, 1995.

[21] D. Selva and D. Krejci, "A survey and assessment of the capabilities of cubesats for earth observation," *Acta Astronautica*, vol. 74, pp. 50–68, 2012. DOI: 10.1016/j.actaastro.2011.12.014.

[22] M. Paine and S. Gabriel, "A micro-fabricated colloidal thruster array," in *37th Joint Propulsion Conference and Exhibit*, 2001, p. 3329. DOI: 10.2514/6.2001-3329.

[23] E. Cardiff, A. Chepko, P. Norgaard, and B. Jamieson, "The nasa gsfc mems colloidal thruster," in *40th AIAA/ASME/SAE/ASEE Joint Propulsion Conference and Exhibit*, 2004, p. 3592. DOI: 10.2514/6.2004-3592.

[24] J. Xiong, Z. Zhou, D. Sun, and X. Ye, "Development of a mems based colloid thruster with sandwich structure," *Sensors and Actuators A: Physical*, vol. 117, no. 1, pp. 168–172, 2005. DOI: 10.1016/j.sna.2004.05.029.

[25] L. F. Velásquez-García, A. I. Akinwande, and M. Martinez-Sanchez, "A planar array of micro-fabricated electrospray emitters for thruster applications," *Journal of Microelectromechanical Systems*, vol. 15, no. 5, pp. 1272–1280, 2006. DOI: 10.1109/JMEMS.2006.879710.

[26] B. Gassend, L. F. Velasquez-garcía, A. I. Akinwande, and M. Martínez-Sánchez, "A microfabricated planar electrospray array ionic liquid ion source with integrated extractor," *Journal of Microelectromechanical Systems*, vol. 18, no. 3, pp. 679–694, 2009. DOI: 10.1109/JMEMS.2009.2015475.

[27] E. Grustan-Gutierrez and M. Gamero-Castaño, "Microfabricated electrospray thruster array with high hydraulic resistance channels," *Journal of Propulsion and Power*, vol. 33, no. 4, pp. 984–991, 2017. DOI: 10.2514/1.B36268.

[28] L. F. Velásquez-García, "Sla 3-d printed arrays of miniaturized, internally fed, polymer electrospray emitters," *Journal of Microelectromechanical Systems*, vol. 24, no. 6, pp. 2117–2127, 2015. DOI: 10.1109/JMEMS.2015.2475696.

[29] H. Kim and L. F. Velásquez-García, "3d-printed, internally fed, mems electrospray thrusters," in *2022 21st International Conference on Micro and Nanotechnology for Power Generation and Energy Conversion Applications (PowerMEMS)*, IEEE, 2022, pp. 46–49. DOI: 10.1109/PowerMEMS56853.2022.10007598.

[30] F. L. Kunze, T. Henning, and P. J. Klar, "3d micro printed capillary electrospray thruster with a fully modular integrated extraction electrode," *Journal of Electric Propulsion*, vol. 3, no. 1, p. 3, 2024. DOI: 10.1007/s44205-023-00066-7.

[31] C. Ma and C. N. Ryan, "Characterization of a micro-electrospray thruster with a porous glass emitter array," in *Proc. Sp. Propuls. Conf*, 2018, pp. 1–12.

[32] M. R. Natisin and H. L. Zamora, "Performance of a fully conventionally machined liquid-ion electrospray thruster operated in pir," in *Proceedings of the 36th International Electric Propulsion Conference, Vienna, Austria*, 2019, pp. 9–12.

[33] M. Martinez-Sanchez, "Electrospray propulsion: A review," in *APS Division of Plasma Physics Meeting Abstracts*, vol. 46, 2004, NM2A–00.

[34] Y.-h. Chiu and R. A. Dressler, "Ionic liquids for space propulsion," in ACS Publications, 2007. DOI: 10.1021/bk-2007-0975.ch010.

[35] S. Jeong, V.-C. Ho, O. Kwon, Y. Park, and J. Mun, "High-stability room temperature ionic liquids: Enabling efficient charge transfer in solid-state batteries by minimizing interfacial resistance," *Energy Materials*, 2023. DOI: 10.20517/energymater.2023.47.

[36] S. Aldrich, *Ionic liquids: Electrochemical apps*, https://www.sigmaaldrich.com/ES/es/technical-documents/technical-article/materials-science-and-engineering/batteries-supercapacitors-and-fuel-cells/ionic-liquids-electrochemical, [Accessed 09-08-2024].

[37] M. Hayyan, F. S. Mjalli, M. A. Hashim, I. M. AlNashef, and T. X. Mei, "Investigating the electrochemical windows of ionic liquids," *Journal of Industrial and Engineering Chemistry*, vol. 19, no. 1, pp. 106–112, 2013. DOI: 10.1016/j.jiec.2012.07.011.

[38] C. Xu and Z. Cheng, "Thermal stability of ionic liquids: Current status and prospects for future development," *Processes*, vol. 9, no. 2, p. 337, 2021. DOI: doi.org/10.3390/pr9020337.

[39] D. Krejci, F. Mier-Hicks, R. Thomas, T. Haag, and P. Lozano, "Emission characteristics of passively fed electrospray microthrusters with propellant reservoirs," *Journal of Spacecraft and Rockets*, vol. 54, no. 2, pp. 447–458, 2017. DOI: 10.2514/1.A33531.

[40] D. G. Courtney, H. Shea, K. Dannenmayer, and A. Bulit, "Charge neutralization and direct thrust measurements from bipolar pairs of ionic electrospray thrusters," *Journal of Spacecraft and Rockets*, vol. 55, no. 1, pp. 54–65, 2018. DOI: 10.2514/1.A33863.

[41] M. Freemantle, *An introduction to ionic liquids*. Royal Society of chemistry, 2010.

[42] Z. Lei, B. Chen, Y.-M. Koo, and D. R. MacFarlane, *Introduction: Ionic liquids*, 2017. DOI: 10.1021/acs.chemrev.7b00246.

[43] A. G. Bailey, J. E. Bracher, and H. Von Rohden, "A capillary-fed annular colloid thruster," *Journal of spacecraft and Rockets*, vol. 9, no. 7, pp. 518–521, 1972. DOI: 10.2514/3.61733.

[44] M. S. Alexander, K. L. Smith, M. D. Paine, and J. P. Stark, "Voltage-modulated flow rate for precise thrust control in colloid electrospray propulsion," *Journal of Propulsion and Power*, vol. 23, no. 5, pp. 1042–1048, 2007. DOI: 10.2514/1.25309.

[45] K. Kinefuchi, S. Cho, and R. Tsukizaki, "Characterization of a capillary flow controller for electric propulsion," *Journal of Propulsion and Power*, vol. 36, no. 4, pp. 586–592, 2020. DOI: 10.2514/1.B37726.

[46] M. Cloupeau and B. Prunet-Foch, "Electrohydrodynamic spraying functioning modes: A critical review," *Journal of Aerosol Science*, vol. 25, no. 6, pp. 1021–1036, 1994. DOI: 10.1016/0021-8502(94)90199-6.

[47] J. Fernández de La Mora, "The fluid dynamics of taylor cones," *Annu. Rev. Fluid Mech.*, vol. 39, no. 1, pp. 217–243, 2007. DOI: 10.1146/annurev.fluid.39.050905.110159.

[48] M. Gamero-Castaño and J. Fernández de la Mora, "Direct measurement of ion evaporation kinetics from electrified liquid surfaces," *The Journal of Chemical Physics*, vol. 113, no. 2, pp. 815–832, 2000. DOI: 10.1063/1.481857.

[49] W. M. Folkner *et al.*, "Disturbance reduction system: Testing technology for precision formation control," in *High-Contrast Imaging for Exo-Planet Detection*, SPIE, vol. 4860, 2003, pp. 221–228. DOI: 10.1117/12.457878.

[50] J. Ziemer *et al.*, "Colloid microthruster flight performance results from space technology 7 disturbance reduction system," in *International Electric Propulsion Conference (IEPC)*, 2017.

[51] R. S. Legge Jr and P. C. Lozano, "Electrospray propulsion based on emitters microfabricated in porous metals," *Journal of Propulsion and Power*, vol. 27, no. 2, pp. 485–495, 2011. DOI: 10.2514/1.50037.

[52] C. Huang, J. Li, M. Li, T. Si, C. Xiong, and W. Fan, "Experimental investigation on current modes of ionic liquid electrospray from a coned porous emitter," *Acta Astronautica*, vol. 183, pp. 286–299, 2021. DOI: 10.1016/j.actaastro.2021.03.014.

[53] C. Ma, T. G. Bull, and C. Ryan, "Time-of-flight characterization of electrospray thrusters using porous emitters with high emission currents," *Journal of Propulsion and Power*, 2021.

[54] P. Wright and R. E. Wirz, "Transient flow in porous electrospray emitters," in *Aiaa propulsion and energy 2021 forum*, 2021, p. 3437. DOI: 10.2514/6.2021-3437.

[55] Y.-H. Chiu, G. Gaeta, T. Heine, R. Dressler, and D. Levandier, "Analysis of the electrospray plume from the emi-im propellant externally wetted on a tungsten needle," in *42nd AIAA/ASME/SAE/ASEE Joint Propulsion Conference & Exhibit*, 2006, p. 5010. DOI: 10.2514/6.2006-5010.

[56] B. Gassend, L. F. Velásquez-García, A. Akinwande, and M. Martínez-Sánchez, "A fully integrated microfabricated externally wetted electrospray thruster," in *43rd AIAA/ASME/SAE/ASEE Joint Propulsion Conf.*, 2007. DOI: 10.2514/6.2007-5182.

[57] B. Ticknor, S. Miller, and Y.-H. Chiu, "Mass spectrometric analysis of the electrospray plume from an externally wetted tungsten ribbon emitter," in *45th AIAA/ASME/SAE/ASEE Joint Propulsion Conference & Exhibit*, 2009, p. 5088. DOI: 10.2514/6.2009-5088.

[58] P. Lozano and M. Martínez-Sánchez, "Ionic liquid ion sources: Characterization of externally wetted emitters," *Journal of colloid and interface science*, vol. 282, no. 2, pp. 415–421, 2005. DOI: 10.1016/j.jcis.2004.08.132.

[59] D. G. Courtney, N. Alvarez, and N. R. Demmons, "Electrospray thrusters for small spacecraft control: Pulsed and steady state operation," in *2018 Joint Propulsion Conference*, 2018, p. 4654. DOI: 10.2514/6.2018-4654.

[60] C. Ryan *et al.*, "The microthrust mems electrospray thruster: Results and conclusions," in *Space propulsion conference*, 2014.

[61] D. G. Courtney, "Ionic liquid ion source emitter arrays fabricated on bulk porous substrates for spacecraft propulsion," Ph.D. dissertation, Massachusetts Institute of Technology, 2011.

[62] F. A. Hill, E. V. Heubel, P. P. de Leon, and L. F. Velásquez-García, "High-throughput ionic liquid ion sources using arrays of microfabricated electrospray emitters with integrated extractor grid and carbon nanotube flow control structures," *Journal of Microelectromechanical Systems*, vol. 23, no. 5, pp. 1237–1248, 2014. DOI: 10.1109/JMEMS.2014.2320509.

[63] J. Bester, B. Groenewald, and R. Wilkinson, "Electrical power system for a 3u cubesat nanosatellite incorporating peak power tracking with dual redundant control," *Przegląd Elektrotechniczny. Selected full texts*, vol. 88, pp. 300–304, 2012.

[64] P. Lozano and M. Martinez-Sanchez, "Efficiency estimation of emi-bf4 ionic liquid electrospray thrusters," in *41st AIAA/ASME/SAE/ASEE Joint Propulsion Conference & Exhibit*, 2005, p. 4388. DOI: 10.2514/6.2005-4388.

[65] E. Petro, A. Bruno, P. Lozano, L. E. Perna, and D. Freeman, "Characterization of the tile electrospray emitters," in *Aiaa propulsion and energy 2020 forum*, 2020, p. 3612. DOI: 10.2514/6.2020-3612.

[66] S. Xue, L. Duan, and Q. Kang, "Study on the electrowetting and beam current characteristics of externally wetted ionic liquid electrospray thruster," *AIP Advances*, vol. 11, no. 12, 2021. DOI: 10.1063/5.0069731.

[67] Y. Fujiwara, "Temperature effects on electrospray current from an externally wetted emi-im ionic liquid ion source," *Journal of Vacuum Science & Technology B*, vol. 41, no. 6, 2023. DOI: 10.1116/6.0003088.

[68] P. Lozano and M. Martínez-Sánchez, "Ionic liquid ion sources: Characterization of externally wetted emitters," *Journal of colloid and interface science*, vol. 282, no. 2, pp. 415–421, 2005. DOI: 10.1016/j.jcis.2004.08.132.

[69] J. Fernández de la Mora and I. G. Loscertales, "The current emitted by highly conducting taylor cones," *Journal of Fluid Mechanics*, vol. 260, pp. 155–184, 1994. DOI: 10.1017/S0022112094003472.

[70] P. Lozano, "Energy properties of an emi-im ionic liquid ion source," *Journal of Physics D: Applied Physics*, vol. 39, no. 1, p. 126, 2005. DOI: 10.1088/0022-3727/39/1/020.

[71] M. Gamero-Castaño and A. Cisquella-Serra, "Electrosprays of highly conducting liquids: A study of droplet and ion emission based on retarding potential and time-of-flight spectrometry," *Physical Review Fluids*, vol. 6, no. 1, p. 013 701, 2021. DOI: 10.1103/PhysRevFluids.6.013701.

[72] D. Villegas-Prados, J. Cruz, M. Wijnen, S. Correyero, P. Fajardo, and J. Navarro-Cavallé, "Impact of propellant temperature on the emission regime of an externally wetted electrospray system using time-of-flight mass spectrometry," *Acta Astronautica*, 2023. DOI: 10.1016/j.actaastro.2023.08.045.

[73] K. W. Jung, S. S. Choi, and K.-H. Jung, "An electron-impact ionization time-of-flight mass spectrometer using a simple high-voltage square pulse generator," *Review of scientific instruments*, vol. 62, no. 9, pp. 2125–2130, 1991. DOI: 10.1063/1.1142378.

[74] P. Marmillod, S. Antonioni, and U. J. Lorenz, "A radio frequency/high voltage pulse generator for the operation of a planar multipole ion trap/time-of-flight mass spectrometer," *Review of Scientific Instruments*, vol. 84, no. 4, 2013. DOI: 10.1063/1.4802630.

[75] J. Kim, "Construction and test of an ion-gate with high-voltage switch system for single-reflection time of flight measurement," *AIP Advances*, vol. 10, no. 2, 2020. DOI: 10.1063/1.5133813.

[76] O. K. Yoon, I. A. Zuleta, M. D. Robbins, G. K. Barbula, and R. N. Zare, "Simple template-based method to produce bradbury-nielsen gates," *Journal of the American Society for Mass Spectrometry*, vol. 18, pp. 1901–1908, 2007. DOI: 10.1016/j.jasms.2007.07.030.

[77] L. J. Pérez-Lorenzo and J. Fernández de la Mora, "Probing electrically driven nanojets by energy and mass analysis in vacuo," *Journal of Fluid Mechanics*, vol. 931, 2022. DOI: 10.1017/jfm.2021.771.

[78] C. E. Miller, "Characterization of ion cluster fragmentation in ionic liquid ion sources," Ph.D. dissertation, Massachusetts Institute of Technology, 2019.

[79] P. Lozano, "Studies on the ion-droplet mixed regime in colloid thrusters," Ph.D. dissertation, Massachusetts Institute of Technology, 2003.

[80] A. Elserougi, A. M. Massoud, A. Ibrahim, and S. Ahmed, "A high voltage pulse-generator based on dc-to-dc converters and capacitor-diode voltage multipliers for water treatment applications," *IEEE Transactions on Dielectrics and Electrical Insulation*, vol. 22, no. 6, pp. 3290–3298, 2015. DOI: 10.1109/TDEI.2015.005376.

[81] J. Mankowski and M. Kristiansen, "A review of short pulse generator technology," *IEEE Transactions on Plasma Science*, vol. 28, no. 1, pp. 102–108, 2000. DOI: 10.1109/27.842875.

[82] M. R. Q. R. Abadi, M. H. Marzebali, V. Abolghasemi, and M. H. Anisi, "High-voltage pulse generators for electroporation applications: A systematic review," *IEEE Access*, vol. 10, pp. 64 933–64 951, 2022. DOI: 10.1109/ACCESS.2022.3184015.

[83] M. A. Elgenedy, "High-voltage pulse generators incorporating modular multilevel converter sub-modules," Ph.D. dissertation, University of Strathclyde, 2018. DOI: 10.48730/ds93-qb07.

[84] F. Blazquez-Plaza, A. Barrado, and M. Wijnen, "Power converter with high gain, high performance for space thrusters based on electrospray technology," in *Aerospace Europe Conference EUCASS-CEAS*, 2023. DOI: 10.13009/EUCASS2023-986.

[85] J. A. Serrano, P. Alou, and J. A. Oliver, "Dcm forward-flyback converter with cockcroft-walton voltage multiplier: Steady-state analysis considering the influence of the parasitic capacitances at very low power and very high voltage gain," in *2019 IEEE Energy Conversion Congress and Exposition (ECCE)*, IEEE, 2019, pp. 6841–6847. DOI: 10.1109/ECCE.2019.8911903.

[86] P. Horowitz and W. Hill, *The art of electronics*. Cambridge university press Cambridge, 1978.

[87] M. J. Breddan and R. E. Wirz, "Electrospray plume divergence: Background pressure influence," *Journal of Aerosol Science*, p. 106 417, 2024. DOI: 10.1016/j.jaerosci.2024.106417.

[88] M. Gamero-Castaño and M. Galobardes-Esteban, "Electrospray propulsion: Modeling of the beams of droplets and ions of highly conducting propellants," *Journal of Applied Physics*, vol. 131, no. 1, 2022. DOI: 10.1063/5.0073380.

[89] G. Yuntao *et al.*, "Direct thrust test and asymmetric performance of porous ionic liquid electrospray thruster," *Chinese Journal of Aeronautics*, vol. 36, no. 4, pp. 120–133, 2023. DOI: 10.1016/j.cja.2022.09.007.

[90] D. Villegas-Prados, J. Cruz, M. Wijnen, P. Fajardo, and J. Navarro-Cavallé, "Emission and performance characterization of ionic liquids for an externally wetted electrospray thruster," *Acta Astronautica*, vol. 219, pp. 97–107, 2024. DOI: 10.1016/j.actaastro.2024.03.013.

[91] I. Romero-Sanz, R. Bocanegra, J. Fernandez De La Mora, and M. Gamero-Castaño, "Source of heavy molecular ions based on taylor cones of ionic liquids operating in the pure ion evaporation regime," *Journal of Applied Physics*, vol. 94, no. 5, pp. 3599–3605, 2003. DOI: 10.1063/1.1598281.

[92] S. Mazouffre, "Electric propulsion for satellites and spacecraft: Established technologies and novel approaches," *Plasma Sources Science and Technology*, vol. 25, no. 3, p. 033 002, 2016. DOI: 10.1088/0963-0252/25/3/033002.

[93] M. A. Silva, D. C. Guerrieri, A. Cervone, and E. Gill, "A review of mems micropropulsion technologies for cubesats and pocketqubes," *Acta Astronautica*, vol. 143, pp. 234–243, 2018. DOI: 10.1016/j.actaastro.2017.11.049.

[94] A. R. Tummala and A. Dutta, "An overview of cube-satellite propulsion technologies and trends," *Aerospace*, vol. 4, no. 4, p. 58, 2017. DOI: 10.3390/aerospace4040058.

[95] D. Krejci, M. G. Jenkins, and P. Lozano, "Staging of electric propulsion systems: Enabling an interplanetary cubesat," *Acta Astronautica*, vol. 160, pp. 175–182, 2019. DOI: 10.1016/j.actaastro.2019.04.031.

[96] J. Fernández de la Mora, G. J. Van Berkel, C. G. Enke, R. B. Cole, M. Martínez-Sánchez, and J. B. Fenn, "Electrochemical processes in electrospray ionization mass spectrometry," *Journal of Mass Spectrometry*, vol. 35, no. 8, pp. 939–952, 2000. DOI: 10.1002/1096-9888(200008)35:8<939::AID-JMS36>3.0.CO;2-V.

[97] A. Cisquella-Serra, M. Galobardes-Esteban, and M. Gamero-Castaño, "Scalable microfabrication of multi-emitter arrays in silicon for a compact microfluidic electrospray propulsion system," *ACS Applied Materials and Interfaces*, vol. 14, no. 38, pp. 43 527–43 537, 2022. DOI: 10.1021/acsami.2c12716.

[98] M. Cloupeau and B. Prunet-Foch, "Electrostatic spraying of liquids in cone-jet mode," *Journal of electrostatics*, vol. 22, no. 2, pp. 135–159, 1989. DOI: 10.1016/0304-3886(89)90081-8.

[99] A. M. Gañán-Calvo and J. M. Montanero, "Revision of capillary cone-jet physics: Electrospray and flow focusing," *Physical review E*, vol. 79, no. 6, p. 066 305, 2009. DOI: 10.1103/PhysRevE.79.066305.

[100] J. Iribarne and B. Thomson, "On the evaporation of small ions from charged droplets," *The Journal of chemical physics*, vol. 64, no. 6, pp. 2287–2294, 1976. DOI: 10.1063/1.432536.

[101] B. D. Prince *et al.*, "A combined experimental and theoretical treatment of ionic liquid thermal dissociation," in *53rd AIAA/SAE/ASEE Joint Propulsion Conference*, 2017, p. 4970. DOI: 10.2514/6.2017-4970.

[102] C. Coffman, M. Martínez-Sánchez, F. Higuera, and P. Lozano, "Structure of the menisci of leaky dielectric liquids during electrically-assisted evaporation of ions," *Applied Physics Letters*, vol. 109, no. 23, p. 231 602, 2016. DOI: 10.1063/1.4971778.

[103] C. Larriba *et al.*, "Taylor cones of ionic liquids as ion sources: The role of electrical conductivity and surface tension," *ChemInform*, vol. 39, no. 42, no–no, 2008. DOI: 10.1021/bk-2007-0975.ch021.

[104] D. Garoz *et al.*, "Taylor cones of ionic liquids from capillary tubes as sources of pure ions: The role of surface tension and electrical conductivity," *Journal of Applied Physics*, vol. 102, no. 6, p. 064 913, 2007. DOI: 10.1063/1.2783769.

[105] S. Castro *et al.*, "Effect of liquid properties on electrosprays from externally wetted ionic liquid ion sources," *Journal of Applied Physics*, vol. 102, no. 9, p. 094 310, 2007. DOI: 10.1063/1.2802547.

[106] A. M. Gañán-Calvo, N. Rebollo-Muñoz, and J. Montanero, "The minimum or natural rate of flow and droplet size ejected by taylor cone–jets: Physical symmetries and scaling laws," *New Journal of Physics*, vol. 15, no. 3, p. 033 035, 2013. DOI: 10.1088/1367-2630/15/3/033035.

[107] M. Gamero-Castaño, "Characterization of the electrosprays of 1-ethyl-3-methylimidazolium bis (trifluoromethylsulfonyl) imide in vacuum," *Physics of Fluids*, vol. 20, no. 3, p. 032 103, 2008. DOI: 10.1063/1.2899658.

[108] S. Castro and J. Fernández De La Mora, "Effect of tip curvature on ionic emissions from taylor cones of ionic liquids from externally wetted tungsten tips," *Journal of Applied Physics*, vol. 105, no. 3, 2009. DOI: 10.1063/1.3073873.

[109] G. L. Mair, "The effects of flow impedance on the current-voltage characteristics of liquid-metal ion sources," *Journal of Physics D: Applied Physics*, vol. 30, no. 13, p. 1945, 1997. DOI: 10.1088/0022-3727/30/13/017.

[110] V. L. Pisacane, *Fundamentals of space systems*. Johns Hopkins University/Appli, 2005.

[111] N. A. Kreitinger, *Temperature effects on electrospray performance*, 2011.

[112] R. S. Legge Jr, "Fabrication and characterization of porous metal emitters for electrospray applications," Ph.D. dissertation, Massachusetts Institute of Technology, 2008.

[113] D. Conroy and J. Ziemer, "Water contaminant mitigation in ionic liquid propellant," in *International Electric Propulsion Conference (IEPC)*, 2009.

[114] A. P. Froba, H. Kremer, and A. Leipertz, "Density, refractive index, interfacial tension, and viscosity of ionic liquids [emim][etso4],[emim][ntf2],[emim][n (cn) 2], and [oma][ntf2] in dependence on temperature at atmospheric pressure," *The Journal of Physical Chemistry B*, vol. 112, no. 39, pp. 12 420–12 430, 2008. DOI: 10.1021/jp804319a.

[115] T. Makino, M. Kanakubo, Y. Masuda, T. Umecky, and A. Suzuki, "Co2 absorption properties, densities, viscosities, and electrical conductivities of ethylimidazolium and 1-ethyl-3-methylimidazolium ionic liquids," *Fluid Phase Equilibria*, vol. 362, pp. 300–306, 2014. DOI: 10.1016/j.fluid.2013.10.031.

[116] R. Khalil, N. Chaabene, M. Azar, I. B. Malham, and M. Turmine, "Effect of the chain lengthening on transport properties of imidazolium-based ionic liquids," *Fluid Phase Equilibria*, vol. 503, p. 112 316, 2020. DOI: 10.1016/j.fluid.2019.112316.

[117] P. Lozano and M. Martínez-Sánchez, "Ionic liquid ion sources: Suppression of electrochemical reactions using voltage alternation," *Journal of colloid and interface science*, vol. 280, no. 1, pp. 149–154, 2004. DOI: 10.1016/j.jcis.2004.07.037.

[118] E. Grustan-Gutierrez, S. Jhuree, and J. P. Stark, "Modelling of colloid thrusters for mission analysis," 2017.

[119] K. N. Marsh, J. A. Boxall, and R. Lichtenthaler, "Room temperature ionic liquids and their mixtures—a review," *Fluid phase equilibria*, vol. 219, no. 1, pp. 93–98, 2004. DOI: 10.1016/j.fluid.2004.02.003.

[120] P. Walden, "Molecular weights and electrical conductivity of several fused salts," *Bull. Acad. Imper. Sci.(St. Petersburg)*, vol. 1800, 1914. DOI: 10.3389/fchem.2020.627213.

[121] M. Gamero-Castano and V. Hruby, "Electrospray as a source of nanoparticles for efficient colloid thrusters," *Journal of Propulsion and Power*, vol. 17, no. 5, pp. 977–987, 2001. DOI: 10.2514/2.5858.

[122] B. D. Prince, B. A. Fritz, and Y.-H. Chiu, "Ionic liquids in electrospray propulsion systems," in *Ionic Liquids: Science and Applications*, ACS Publications, 2012, pp. 27–49. DOI: 10.1021/bk-2012-1117.ch002.

[123] X. Gallud and P. C. Lozano, *The limited effect of electric conductivity on the ion current evaporated from electrospray sources*, 2023. DOI: 10.48550/arXiv.2305.14714. arXiv: 2305.14714.

[124] C. Schreiner, S. Zugmann, R. Hartl, and H. J. Gores, "Fractional walden rule for ionic liquids: Examples from recent measurements and a critique of the so-called ideal kcl line for the walden plot," *Journal of Chemical & Engineering Data*, vol. 55, no. 5, pp. 1784–1788, 2010. DOI: 10.1021/je900878j.

[125] R. Krpoun, K. L. Smith, J. P. Stark, and H. R. Shea, "Tailoring the hydraulic impedance of out-of-plane micromachined electrospray sources with integrated electrodes," *Applied Physics Letters*, vol. 94, no. 16, 2009. DOI: 10.1063/1.3117191.

[126] X. Gallud and P. C. Lozano, "The emission properties, structure and stability of ionic liquid menisci undergoing electrically assisted ion evaporation," *Journal of Fluid Mechanics*, vol. 933, 2021. DOI: 10.48550/arXiv.2109.12274.

[127] C. HUANG, L. Jianling, and L. Mu, "Performance measurement and evaluation of an ionic liquid electrospray thruster," *Chinese Journal of Aeronautics*, 2021. DOI: 10.1016/j.cja.2021.10.030.

[128] C. Huang, J. Li, and M. Li, "Experimental characterization of the electrospray propulsive performance for ionic liquid propellants [emim][dca] and [bmim][dca]," *Fuel*, vol. 336, p. 126 822, 2023. DOI: 10.1016/j.fuel.2022.126822.

[129] S. P. Berg, "Development of ionic liquid multi-mode spacecraft micropropulsion systems," 2015.

[130] S. Stovbun, A. Shchegolikhin, S. Usachev, S. Khomik, and S. Medvedev, "Synthesis and testing of hypergolic ionic liquids for chemical propulsion," *Acta Astronautica*, vol. 135, pp. 110–113, 2017. DOI: 10.1016/j.actaastro.2016.11.047.

[131] J. L. Rovey *et al.*, "Review of multimode space propulsion," *Progress in Aerospace Sciences*, vol. 118, p. 100 627, 2020. DOI: 10.1016/j.paerosci.2020.100627.

[132] Z. Li *et al.*, "Hypergolic coordination compounds as modifiers for ionic liquid propulsion," *Chemical Engineering Journal*, vol. 423, p. 130 187, 2021. DOI: 10.1016/j.cej.2021.130187.

[133] Y. Jin *et al.*, "Recent advances in hypergolic ionic liquids with broad potential for propellant applications," *FirePhysChem*, vol. 2, no. 3, pp. 236–252, 2022. DOI: 10.1016/j.fpc.2022.04.001.

[134] C. Ryan *et al.*, "Experimental progress towards the microthrust mems electrospray electric propulsion system," in *33rd International Electric Propulstion Conference*, 2013.

[135] N. Timilsina, *Electrospray Thrusters for Attitude Control of a 1-U CubeSat*. University of California, Irvine, 2014.

[136] R. Ramos-Tomás, D. Villegas-Prados, B. de Saavedra, J. Cruz, and B. Sepúlveda, "Impact of tip angle on the divergence and efficiency of electrospray thrusters," *ACS Applied Electronic Materials*, vol. 6, no. 10, pp. 7319–7328, 2024. DOI: 10.1021/acsaelm.4c01224.

[137] A. Tamayol and M. Bahrami, "Transverse permeability of fibrous porous media," *Physical review E*, vol. 83, no. 4, p. 046 314, 2011. DOI: 10.1103/PhysRevE.83.046314.

[138] V. Ruiz, T. Huynh, S. R. Sivakkumar, and A. Pandolfo, "Ionic liquid–solvent mixtures as supercapacitor electrolytes for extreme temperature operation," *RSC advances*, vol. 2, no. 13, pp. 5591–5598, 2012. DOI: 10.1039/C2RA20177A.

[139] F. Fan *et al.*, "Effect of molecular weight on the ion transport mechanism in polymerized ionic liquids," *Macromolecules*, vol. 49, no. 12, pp. 4557–4570, 2016. DOI: 10.1021/acs.macromol.6b00714.

[140] S. Zhang, X. Lu, Q. Zhou, X. Li, X. Zhang, and S. Li, *Ionic liquids: physicochemical properties*. Elsevier, 2009. DOI: 10.1016/j.fluid.2019.112304.

[141] W. Martino, J. F. De La Mora, Y. Yoshida, G. Saito, and J. Wilkes, "Surface tension measurements of highly conducting ionic liquids," *Green Chemistry*, vol. 8, no. 4, pp. 390–397, 2006. DOI: 10.1039/B515404A.

[142] Y.-H. Yu, A. N. Soriano, and M.-H. Li, "Heat capacities and electrical conductivities of 1-ethyl-3-methylimidazolium-based ionic liquids," *The Journal of Chemical Thermodynamics*, vol. 41, no. 1, pp. 103–108, 2009. DOI: 10.1016/j.jct.2008.07.013.

[143] J. S. Torrecilla, T. Rafione, J. García, and F. Rodríguez, "Effect of relative humidity of air on density, apparent molar volume, viscosity, surface tension, and water content of 1-ethyl-3-methylimidazolium ethylsulfate ionic liquid," *Journal of Chemical & Engineering Data*, vol. 53, no. 4, pp. 923–928, 2008. DOI: 10.1021/je700523b.

[144] O. Nordness, L. D. Simoni, M. A. Stadtherr, and J. F. Brennecke, "Characterization of aqueous 1-ethyl-3-methylimidazolium ionic liquids for calculation of ion dissociation," *The Journal of Physical Chemistry B*, vol. 123, no. 6, pp. 1348–1358, 2019. DOI: 10.1021/acs.jpcb.8b11892.

[145] H. Rodriguez and J. F. Brennecke, "Temperature and composition dependence of the density and viscosity of binary mixtures of water+ ionic liquid," *Journal of Chemical & Engineering Data*, vol. 51, no. 6, pp. 2145–2155, 2006. DOI: 10.1021/je0602824.

[146] P. D. Prewett and G. L. R. Mair, "Focused ion beams from liquid metal ion sources," *Vacuum*, vol. 43, p. 272, 1992. DOI: 10.1016/0042-207X(92)90309-K.

[147] A. Thuppul, P. L. Wright, A. L. Collins, J. K. Ziemer, and R. E. Wirz, "Lifetime considerations for electrospray thrusters," *Aerospace*, vol. 7, no. 8, p. 108, 2020. DOI: 10.2514/6.2018-4652.

[148] C. Barrios-Collado, G. Vidal-de-Miguel, and P. M.-L. Sinues, "Numerical modeling and experimental validation of a universal secondary electrospray ionization source for mass spectrometric gas analysis in real-time," *Sensors and Actuators B: Chemical*, vol. 223, pp. 217–225, 2016. DOI: 10.1016/j.snb.2015.09.073.

[149] R. Alonso-Matilla, J. Fernández-García, H. Congdon, and J. Fernández de la Mora, "Search for liquids electrospraying the smallest possible nanodrops in vacuo," *Journal of Applied Physics*, vol. 116, no. 22, 2014. DOI: 10.1063/1.4901635.

[150] N. M. Uchizono *et al.*, "Emission modes in electrospray thrusters operating with high conductivity ionic liquids," *Aerospace*, vol. 7, no. 10, p. 141, 2020. DOI: 10.3390/aerospace7100141.

[151] A. Thuppul, A. Collins, P. Wright, N. Uchizono, and R. Wirz, "Mass flux and current density distributions of electrospray plumes," *Journal of Applied Physics*, vol. 130, no. 10, 2021. DOI: 10.1063/5.0056761.

[152] D. G. Courtney, Z. Wood, and T. Fedkiw, "Reconstructing electrospray plume current spatial distributions using computed tomography," in *36th International Electric Propulsion Conference, University of Vienna, Austria*, 2019, pp. 15–20.

[153] T. Fedkiw, Z. D. Wood, and N. R. Demmons, "Improved computed tomography current mapping of electrospray thrusters," in *AIAA Propulsion and Energy 2021 Forum*, 2021, p. 3389. DOI: 10.2514/6.2021-3389.

[154] A. C. Kak and M. Slaney, *Principles of computerized tomographic imaging*. SIAM, 2001.

[155] M. Magnani and M. Gamero-Castaño, "Modelling and scaling laws of the ion emission regime in taylor cones," *Journal of Fluid Mechanics*, vol. 972, A34, 2023. DOI: 10.1017/jfm.2023.717.

[156] M. Caballero-Pérez and M. Gamero, "Increasing specific impulse in electrospray devices through emitter design," in *38th International Electric Propulsion Conference, Toulouse, France*, 2024.

[157] B. De Saavedra, D. Villegas-Prados, M. Wijnen, and P. Fajardo, "Comparison of direct and indirect performance measurements of an externally wetted, passively fed electrospray thruster," in *38th International Electric Propulsion Conference, Toulouse, France*, 2024.

[158] M. J. Breddan and R. E. Wirz, "Electrospray plume evolution: Influence of drag," *Journal of Aerosol Science*, vol. 167, p. 106 079, 2023. DOI: 10.1016/j.jaerosci.2022.106079.